UNIVERSIDADE DE SÃO PAULO
ESCOLA DE ENGENHARIA DE LORENA

ISNALDI RODRIGUES DE SOUZA FILHO

Phase transformations in a high-Mn steel: strain hardening mechanisms, austenite reversion, and athermal martensitic transformation

Transformações de fase em um aço de alto Mn: mecanismos de encruamento, reversão da austenita e transformação martensítica atérmica

Lorena
2019

ISNALDI RODRIGUES DE SOUZA FILHO

Phase transformations in a high-Mn steel: strain hardening mechanisms, austenite reversion, and athermal martensitic transformation

Thesis presented at Escola de Engenharia de Lorena of Universidade de São Paulo to obtain the degree of Doctoral of Science issued by the Programa de Pós-Graduação em Engenharia de Materiais in the field of Conventional and Advanced Materials.

Advisor: Dr. Maria José Ramos Sandim

Original Version

Lorena

2019

Ficha catalográfica elaborada pelo Sistema Automatizado
da Escola de Engenharia de Lorena,
com os dados fornecidos pelo(a) autor(a)

Souza Filho, Isnaldi Rodrigues de
Phase transformations in a high-Mn steel: strain hardening mechanisms, austenite reversion, and athermal martensitic transformation / Isnaldi Rodrigues de Souza Filho; orientadora Maria José Ramos Sandim - Versão Original. - Lorena, 2019.
152 p.

Tese (Doutorado em Ciências - Programa de Pós Graduação em Engenharia de Materiais na Área de Materiais Convencionais e Avançados) - Escola de Engenharia de Lorena da Universidade de São Paulo. 2019

1. High-mn steel. 2. Strain-hardening mechanisms. 3. Austenite reversion. 4. Athermal martensitic transformation. 5. Magnetic properties. I. Título. II. Sandim, Maria José Ramos, orient.

ISNALDI RODRIGUES DE SOUZA FILHO

Transformações de fase em um aço de alto Mn: mecanismos de encruamento, reversão da austenita e transformação martensítica atérmica

Tese apresentada à Escola de Engenharia de Lorena da Universidade de São Paulo para obtenção do título de Doutor em Ciências do Programa de Pós-Graduação em Engenharia de Materiais na área de Materiais Convencionais e Avançados.

Orientadora: Profa. Dra. Maria José Ramos Sandim

Versão Original

Lorena

2019

Ficha catalográfica elaborada pelo Sistema Automatizado
da Escola de Engenharia de Lorena,
com os dados fornecidos pelo(a) autor(a)

Souza Filho, Isnaldi Rodrigues de
Transformações de fase em um aço de alto Mn: mecanismos de encruamento, reversão da austenita e transformação martensítica atérmica / Isnaldi Rodrigues de Souza Filho; orientadora Maria José Ramos Sandim - Versão Original. - Lorena, 2019.
152 p.

Tese (Doutorado em Ciências - Programa de Pós Graduação em Engenharia de Materiais na Área de Materiais Convencionais e Avançados) - Escola de Engenharia de Lorena da Universidade de São Paulo. 2019

1. Aços de alto mn. 2. Mecanismos de encruamento. 3. Reversão da austenita. 4. Transformação martensítica atérmica. 5. Propriedades magnéticas. I. Título. II. Sandim, Maria José Ramos, orient.

To Isnaldi and Denise,

my beloved parents and true examples of strength.

ACKNOWLEDGMENTS

To Prof. Dr. Dagoberto Brandão Santos (UFMG) for kindly supplying the steel investigated in this work;

To FAPESP for the Doctoral grants 2015/26409-8 and 2017/17170-7 (BEPE);

To Dr. Maria José R. Sandim for the guidance throughout these years;

To Prof. Dr.-Ing. habil. Dierk Raabe (MPIE – Düsseldorf) for the supervision during the internship in Germany;

To Prof. Dr. Hugo R. Z. Sandim (DEMAR – EEL – USP) and to Dr. Dirk Ponge and Dr. Baptiste Gault (MPIE) for the collaboration and enlightening discussions;

To Dr. Luiz C. C. M. Nagamine, Sérgio Romero and Renato Cohen (Instituto de Física – USP) for the collaboration with the magnetic measurements;

To Katja Angenendt and Monika Nellessen (MPIE) for the training in high-resolution microscopy;

To Benjamin Breitbach (MPIE) for the high-resolution XRD measurements;

To Dr. Wenjun Lu (MPIE) for the TEM measurements;

To the colleagues Alisson K. da Silva and Cauê C. Silva for the valuable collaboration during this work;

To PPGEM (Programa de Pós-Graduação em Engenharia de Materiais) and to EEL – USP (Escola de Engenharia de Lorena) for the technical support;

To my parents Isnaldi and Denise and brother Irving for all unconditional support;

To Lorena Bonno Bissoli for joining me throughout this journey.

“The two most important days in your life are the day you are born and the day you find out why”

Mark Twain

ABSTRACT

SOUZA FILHO, I. R. **Phase transformations in a high-Mn steel: strain hardening mechanisms, austenite reversion, and athermal martensitic transformation**. 2019. 152p. Thesis (Doctoral of Science) – Escola de Engenharia de Lorena, Universidade de São Paulo, Lorena, 2019.

In this work, phase transformations in a high-Mn steel containing 17.6 wt.% of Mn and belonging to the Fe-Mn-Al-Si-C-Ni system were investigated for a variety of states, including cold rolled and annealed ones. The strain hardening mechanisms of austenite, ε-, and α'-martensite were tracked during cold rolling. The complex superposition of several displacive reactions were revealed for each phase with the aid of the combinatorial use of XRD measurements (coupled with the software MAUD), ECCI-SEM, and EBSD. Dilatometry measurements revealed that the austenite reversion splits into two stages during continuous annealing. Such phenomenon is due to strong elemental partitioning between the growing austenite and the α'-matrix, as simulated using the software DICTRA and confirmed via near-atomic resolution APT. Results provided new insights that the successful austenite nucleation is preceded by long-range elemental partitioning. Besides, the growth of austenite is also given by strong elemental partitioning and solute redistribution within both austenite and α'-martensite. Magnetic properties were also investigated for several microstructures of the present steel, modified by means of straining and/or annealing. The formation of nano reversed γ-grains in the early stages of the austenite reversion is sufficient to induce strong magnetic shape anisotropy. Using *in-situ* magnetic measurements and thermodynamic modelling, the Curie temperature of the steel was evaluated, as well as the stability of austenite during controlled conditions of cooling. The influence of local changes in chemical composition on the magnetic properties was deeply investigated by means of magnetic measurements, thermodynamic simulations (Thermo-Calc), high-resolution microscopy, including STEM, and APT. The findings revealed that short- and long-range chemical fluctuations strongly affect the saturation magnetization of the steel and brought new insights on the use of magnetic probing as tool for quantification of phases in Mn-based steels.

Keywords: High-Mn steel. Strain-hardening mechanisms. Austenite reversion. Athermal martensitic transformation. Magnetic properties.

RESUMO

SOUZA FILHO, I. R. **Transformações de fase em um aço de alto Mn: mecanismos de encruamento, reversão da austenita e transformação martensítica atérmica**. 2019. 152p. Tese (Doutorado em Ciências) – Escola de Engenharia de Lorena, Universidade de São Paulo, Lorena, 2019.

Neste trabalho, transformações de fases foram estudadas em um aço contento 17,6 % em massa de Mn e pertencente ao sistema Fe-Mn-Al-Si-C-Ni. Os mecanismos de encruamento na austenita, martensitas ε e α' foram monitorados durante a laminação a frio. A complexa superposição de várias transformações adifusionais foram reveladas para cada fase com auxílio de medidas de difração de raios X (acopladas ao uso do *software* MAUD), ECCI e EBSD. Medidas de dilatometria revelaram que a reversão da austenita ocorre em dois estágios durante recozimentos contínuos. Esse fenômeno é devido à pronunciada partição de elementos entre a austenita revertida e a matriz martensítica, como mostrado por meio de simulações utilizando-se o *software* DICTRA e confirmado via APT. Os resultados obtidos evidenciaram que a nucleação bem-sucedida da austenita é precedida da partição de longo alcance de elementos químicos. Além disso, o crescimento da austenita revertida também é acompanhado de partição de longo alcance e redistribuição de solutos entre as fases γ e α'. As propriedades magnéticas do presente aço também foram investigadas para uma ampla variedade de microestruturas, modificadas por deformação e/ou recozimento. Foi observado que a formação de grãos austeníticos de ordem nanométrica no início da reversão é suficiente para induzir pronunciada anisotropia magnética de forma. Por meio de medidas de magnetização *in-situ* e modelamento termodinâmico, a temperatura de Curie foi avaliada como também a estabilidade da austenita frente ao resfriamento controlado. A influência de mudanças composicionais sobre as propriedades magnéticas foi detalhadamente investigada com auxílio de medidas magnéticas, simulações termodinâmicas (Thermo-Calc), microscopia de alta resolução, incluindo microscopia eletrônica de transmissão (MET), e APT. Os resultados mostraram que flutuações químicas de curto e longo alcance afetam fortemente a magnetização de saturação do material. Além disso, este trabalho trouxe novos *insights* acerca do uso de medidas de magnetização como uma ferramenta para quantificação de fases em aços a base de Mn.

Palavras-chave: Aços de alto Mn. Mecanismos de encruamento. Reversão da austenita. Transformação martensítica atérmica. Propriedades magnéticas.

LIST OF FIGURES

Figure 7.16 - **(a)** Schematic representation of the starting disordered bcc phase (steel deformed to 80%) with random distribution of atoms within the coherent domain sizes (crystallites). The straight dot lines represent the atomic planes. **(b)** Schematic representation of the same specimen after 30 min of annealing at 350°C. The formation of ordered crystallites fragments the initial coherent domain sizes……131

LIST OF TABLES

TABLE OF CONTENTS

Chapter 1

Introduction

In the last decades, the rising interest in Mn-based steels for automotive industry applications is due to their outstanding mechanical properties (FROMMEYER; BRÜX, 2006; DE COOMAN; CHIN; KIM, 2011; KIM; SUH; KIM, 2013; RAABE et al., 2014; ZHANG; RAABE; TASAN, 2017). These materials are known as advanced high strength steels (AHSS) and combine high strength with ductility without sacrificing the crashworthy properties. Depending on several metallurgical aspects, especially the chemical composition in terms of Mn, metastable austenite (γ) in these steels may accommodate deformation by means of different and complex strain hardening mechanisms. Among them, one can cite the transformation-induced plasticity (TRIP effect) where fcc-γ transforms into bcc α'-martensite with or without the intermediate presence of the hcp ε-phase (REMY; PINEAU, 1977; LEE; CHOI, 2000; ALLAIN et al., 2004; BRACKE; KESTENS; PENNING, 2007; SAEED-AKBARI et al., 2009; DING et al., 2011; STEINMETZ et al., 2013; PIERCE et al., 2014; WONG et al., 2016). Another important mechanism for strain accommodation is the twinning-induced plasticity (TWIP effect), where the profuse formation of nano-twins subdivides the original γ-grains into smaller units and consequently diminishes the mean free path for dislocation motion (GRÄSSEL et al., 2000; DE COOMAN; CHIN; KIM, 2011). In terms of Mn, the TRIP effect is generally observed for steels with Mn content lower than 15 wt.%. For Mn compositions higher than 25 wt.%, the TWIP effect is predominant. Finally, for Mn contents ranging between 15 and 25 wt.%, both TRIP and TWIP mechanisms may take place simultaneously (GAZDER et al., 2015).

Recently, Mn-based steels have been designed by means of precipitation reactions, segregation engineering (RAABE et al., 2013), and grain refinement (ZHANG; RAABE; TASAN, 2017). Reduction of anisotropy in mechanical properties is one of the most important advantages of strengthening by means of grain refinement (ESCOBAR; DAFÉ; SANTOS, 2015). This can be achieved by the transformation of α'-martensite back into austenite using the so-called austenite reversion treatments (α' → γ) (DASTUR et al., 2017). In this context, the elemental redistribution (especially Mn) between parent α' and growing γ plays a key role on the final microstructure and mechanical properties of the steel. In fact, Mn possesses very low diffusivity in austenite. Contrastingly, its high diffusivity in α'-martensite promotes Mn fluxes towards the growing austenite, leading to strong partitioning

and segregation at α'/γ interfaces and grain boundaries (DMITRIEVA et al., 2011). In this scenario, the segregation tendency is also observed to be enhanced by high Mn contents.

In light of the above observations, the high-quality performance of Mn-based steels lies on the complexity of their microstructural aspects. In this Doctorate work phase transformations driven either by diffusionless or diffusion mechanisms were carefully investigated for a high-Mn steel belonging to the Fe-Mn-Al-Si-C-Ni system and containing 17.6 wt.% of Mn. The present steel possesses a stacking fault energy (SFE) of ~ 8.1 mJ/m^2 and therefore the formation of α'-martensite is preceded by the intermediate formation of the ε-phase (SOUZA FILHO et al., 2019a). The complex superposition of several displacive (diffusionless) and incommensurate transformation reactions occurring concomitantly in γ, ε - and α'-martensite were revealed for a broad range of strain imposed by rolling (SOUZA FILHO et al., 2019b). With regard to the diffusion reactions, austenite reversion was tracked for continuous and isothermal conditions of annealing. Relevant and new results regarding austenite nucleation and growth, as well as the corresponding elemental redistribution during the occurrence of the α' → γ reaction threw lights on the thermo-kinetics of the austenite reversion in Mn-based steels (SOUZA FILHO et al., 2019c). Starting with fully austenitic microstructures at high temperatures (viz. 800°C), the stability of austenite faced to the athermal martensitic transformation was also investigated by means of *in-situ* magnetic measurements for controlled conditions of cooling and thermodynamic modelling (SOUZA FILHO et al., 2019a). Last but not least, the changes in magnetic properties (especially regarding the coercive field and saturation magnetization) were evaluated for a variety of microstructures modified by straining and/or annealing. In this work, the strong influence of chemical composition fluctuations on the magnetization was clearly revealed for the Mn-based steels variants containing the ferromagnetic α'-martensite. The systematic investigation conducted in this work brings new insights about the use of the magnetization saturation as a probe for quantifying ferromagnetic phases in steels.

This thesis is organized in seven chapters as follows:

Chapter 1: Introduction

Chapter 2: Experimental

Chapter 3 Thermodynamic assessment

Chapter 4: Strain hardening mechanisms during cold rolling: interplay between submicron defects and microtexture

This Chapter is a modified version of the present author's publication: **I.R. Souza Filho**, M.J.R. Sandim, D. Ponge, H.R.Z. Sandim, D. Raabe. Strain hardening mechanisms during cold rolling of a high-Mn steel: Interplay between submicron defects and microtexture. Materials Science & Engineering A, v.754, p.636-649, 2019.

Chapter 5: Martensite to austenite reversion: partitioning-dependent two-stage kinetics revealed by atom probe tomography, in-situ magnetic measurements and simulation

This Chapter is a modified version of the present author's publication: **I.R. Souza Filho,** A. Kwiatkowski da Silva, M.J.R. Sandim, D. Ponge, B. Gault, H.R.Z. Sandim, D. Raabe. Martensite to austenite reversion in a high-Mn steel: Partitioning dependent two-stage kinetics revealed by atom probe tomography, in-situ magnetic measurements and simulation. Acta Materialia, v.166, p.178-191, 2019.

Chapter 6: Magnetic properties: study of strain-induced martensite formation, austenite reversion, and athermal α'-formation

This Chapter is a modified version of the present author's publication: **I.R. Souza Filho**, M.J.R. Sandim, R. Cohen, L.C.C.M. Nagamine, H.R.Z. Sandim, D. Raabe. Magnetic properties of a 17.6 Mn-TRIP steel: Study of strain-induced martensite formation, austenite reversion, and athermal α′-formation. Journal of Magnetism and Magnetic Materials, v.473, p.109-118, 2019.

Chapter 7: Revealing the anomalous increase in magnetization of α'-martensite at low temperatures

Chapter 2

Experimental

2.1 Material

The steel investigated in this study is a high-Mn steel (Fe-Mn-Al-Si-Ni-C) which chemical composition is displayed in Table 2.1. This material was produced according to the procedure reported in Ref. (ZORZI, 2014) and kindly supplied by Prof. Brandão (UFMG) in the form of a 45%-cold-rolled plate with 7 mm of thickness.

Table 2.1 - Chemical composition of the high-Mn steel studied in this work, given in both wt.% and at.%.

%	Mn	Al	Si	C	N	P	S	Fe
wt.%	17.6	1.71	3.22	0.042	0.014	0.020	0.0068	Bal.
at.%	16.9	3.36	6.07	0.019	0.053	0.034	0.012	Bal.

Source: elaborated by the author.

2.1.2 Microstructural homogenization

Given the deformed state of the 7-mm-thick plate, it was annealed at 800°C for 15 min in a conventional tubular furnace (LindBerg Blue) in order to obtain fully recrystallized microstructure. After annealing, the plate was cooled down to room temperature under the furnace inertia and it will be referred to as "as-received" from now on. To evaluate possible effects of elemental macro segregation, energy dispersive spectroscopy (EDS) measurements were carried out using a Zeiss scanning electron microscope (SEM), installed at the *Max-Planck-Institut für Eisenforschung* (MPIE, Düsseldorf).

2.2 Cold rolling

After homogenization annealing (Section 2.1.2), the as-received plate was cold-rolled to equivalent logarithmic strains (ε) of 0.11 (corresponding to 10% of thickness reduction), 0.22 (20%), 0.51 (40%), 0.92 (60%), 1.20 (70%), and 1.56 (80%) in multiple passes, using a two-high/four-high 4-105 model Fenn rolling mill. Each rolling pass was set to produce approximately 10% of thickness reduction.

2.3 Characterization techniques

2.3.1 X-ray diffraction analysis

X-ray diffraction (XRD) was carried out on samples deformed to all levels of true (logarithmic) strain (ε = 0, 0.11, 0.22, 0.51, 0.92, 1.20, and 1.56). Specimens with

dimensions of approximately 20 x 20 mm^2 were cut, ground up to half-thickness, and further polished with colloidal silica suspension. XRD measurements were conducted using a Seifert Type ID3003 diffractometer with Co-$K\alpha$ radiation operated at 40 kV and 30 mA (installed at the MPIE, Düsseldorf). To minimize texture effects, all samples were measured under rotation around their normal direction (ND) with an angular speed of $\pi\ s^{-1}$. The diffracted data were recorded in the range for 2θ from 30 to 120° with steps of 0.03° and a dwell time of 10 s at each angle. From the diffracted data, the volume fractions of austenite, ε- and α'-martensite were determined using the direct comparison method, as performed in preceding studies (SOUZA FILHO et al., 2017; SOUZA FILHO et al., 2019a; SOUZA FILHO et al., 2019b).

The acquired data were further analyzed by means of Rietveld-based refinement using software MAUD (*Materials Analysis Using Diffraction*) (LUTTEROTTI; SCARDI; MAITRELLI; 1990; LUTTEROTTI, 2006). The reliability of each refinement was established by means of the goodness of fit (GoF) parameter, which must converge to 1 (PRINCE, 1993; SAHU; DE; KAJIWARA, 2002). The effective crystallite size (D_{eff}) and accumulated microstrain $<\varepsilon^2_{hh}>^{1/2}$ for all phases were evaluated according to the Popa model (*size-strain* analysis) implemented in MAUD (POPA, 1998). The planar fault parameters of austenite and ε-martensite, which include stacking faults (α) and twinning (β), were estimated in terms of their probabilities (viz. P_α and P_β) according to Warren's approach (*fault* analysis) (WARREN, 1969).

2.3.1.1 Direct comparison method

Phase quantification using XRD data can be conducted by means of the direct comparison method, where the integrated intensity of the peaks belonging to certain phase is assumed to be proportional to its volume fraction (DE et al., 2004). Considering the reflections of austenite, ε- and α'-martensite in the present steel, the γ-volume fraction, for example, is determined as follows:

$$V\gamma = \frac{\frac{1}{n}\sum_{j=1}^{n}\frac{I_\gamma^j}{R_\gamma^j}}{\frac{1}{n}\sum_{j=1}^{n}\frac{I_\gamma^j}{R_\gamma^j} + \frac{1}{n}\sum_{j=1}^{n}\frac{I_\varepsilon^j}{R_\varepsilon^j} + \frac{1}{n}\sum_{j=1}^{n}\frac{I_{\alpha'}^j}{R_{\alpha'}^j}} \qquad (2.1)$$

where, n is the number of peaks for a certain phase (in this case austenite); I is the integrated intensity of the {hkl} peaks, obtained from the diffractogram and R is the scattering factor of the material (CULLITY, 1978). For a given (hkl) peak, R is defined as:

$$R_{hkl} = \left(\frac{1}{v^2}\right)\left[|F|^2 p\left(\frac{1+\cos^2 2\theta}{\sin^2\theta\cos\theta}\right)\right](e^{-2M}) \quad (2.2)$$

where, ν is the volume of the unit cell; F, p, and e^{-2M} are respectively the structure, multiplicity, and temperature-dependent factors for a reflecting (hkl) peak. θ is the corresponding diffraction angle of the peaks. In this work, the scattering factor R was calculated using the parameters available in the software PowderCell. The integrated intensities of the peaks were obtained by means of a fitting profile analysis conducted with the aid of the software High-Score Plus®.

2.3.1.2 Popa Model (1998)

The Gaussian (G_H) and Lorentzian (L_H) components of a diffracted profiles mirror, respectively, the effects of strain and crystallite size (POPA, 1998; KEIJSER, MITTEMEIJER, ROZENDAAL, 1983). These two components can be expressed in terms of their corresponding integral breaths β_{GH} and β_{LH} as follows:

$$G_H(z) = \frac{1}{\beta_{GH}} \cdot e^{\left(-\frac{\pi z^2}{\beta_{GH}^2}\right)} \quad (2.3)$$

$$G_L(z) = \frac{1}{\beta_{LH}} \cdot \left(1 + \frac{\pi^2 \cdot z^2}{\beta_{LH}^2}\right)^{-1} \quad (2.4)$$

For a conventional diffraction experiment, where the used wavelength (λ) is constant, z = 2θ and β_{GH} e β_{LH} are given by:

$$\beta_{GH} = 2\tan\theta\,(2\pi < \varepsilon_{hh}^2 >)^{1/2} \quad (2.5)$$

$$\beta_{LH} = 2\lambda/\left(3 < D_{eff} > \cos\theta\right) \quad (2.6)$$

where $< \varepsilon_{hh}^2 >$ and D_{eff} are the accumulative microstrain and crystallite size, respectively. The Popa model stablishes mathematical solutions compatible with the Rietveld refinement

so that the values of both $< \varepsilon_{hh}^2 >$ and D_{eff} are obtained by means of iterative refinement of the diffracted data.

2.3.1.3 Warren Model (1969)

The Warren model for planar defects in closed-packed structures (1969) considers that the formation of stacking faults is mirrored on both peak shifting and symmetrical broadening. Stacking faults shift different planes to higher or smaller angles depending on their corresponding {hkl} indexes. For a fcc crystal as an example, the measured peak displacement caused by faulting can be expressed as follows:

$$\Delta(2\theta) = \frac{90\sqrt{3}(P_\alpha)tan\theta}{\pi^2(u+b)h_0^2}\sum_b(\pm)L_0 \qquad (2.7)$$

where, $\Delta(2\theta)$ is the peak shift in degrees; $h_0 = (h^2 + k^2 + l^2)^{1/2}$, $L_0 = h + k + l$; "*b*" and "*u*" are, respectively, the number of peaks broadened and unbroadened by faults. The values of $\sum_b(\pm)L_0\,/(u+b)h_0^2$ are constant for different planes of a fcc crystal and can be found in ref. (WARREN, 1969). P_α is the stacking fault probability, an adjustable parameter in MAUD.

Stacking faults also contribute to peak broadening since they can fragment the original coherent domains into smaller units. Therefore, the D_{eff} parameter obtained via the Popa model can be associated to the probabilities of stacking faults and twinning according to the following equation:

$$\frac{1}{D_{eff}} = \frac{1}{D} + \frac{(1.5P_\alpha + P_\beta)}{(u+b)ah_0^2}\sum_b|L_0| \qquad (2.8)$$

where D is the coherent domain of the reflecting {hkl} planes; $\sum_b|L_0|\,/a(u+b)h_0^2$ is constant for each reflecting plane of a fcc crystal and can be found in ref. (WARREN, 1969); P_β is the probability of twinning, also a refinable parameter in MAUD. Mechanical twinning is also responsible for asymmetrical broadening of peak profiles. Hence, one can also determine P_β by means of peak asymmetry analyzes as reported in ref. (WARREN, 1969).

2.3.1.4 Dislocation density and character

The average dislocation density (ρ_{av}) for austenite, ε- and α'-martensite was estimated according to the statements of Williamson and Smallman (1956), i.e.

$$\rho_{av} = \left(\frac{3 \cdot K \cdot < \varepsilon_{hh}^2 >}{D_{eff}^2 \cdot b^2}\right)^{1/2} \qquad (2.9)$$

where K = 16.6 for austenite (fcc) and 14.4 for α'-martensite (bcc) (FUSTER et al., 2015). For ε-martensite (hcp), K is assumed as being in the order of 18 (GUPTA; ANANTHARAMAN, 1971) b is the magnitude of the Burgers vector, which is equivalent to $a/\sqrt{2}$ in the <110> directions of the fcc structure (where "a" is the lattice parameter). For bcc, b = $a\sqrt{3}/2$ along the <111> directions. In this work, b = $a/3$ is considered along the <11$\bar{2}$0> directions of the hcp cell.

The dislocation character (q) in γ and α'-martensite was evaluated by using the modified Williamson-Hall method (ÚNGAR, 1999), according to the following equation:

$$\Delta K \cong \frac{1}{D} + \varepsilon_{lattice} \cdot [K^2 \cdot \bar{C}_{h00} \cdot (1 - qH^2)] \qquad (2.10)$$

where, ΔK = 2cosθ(FWHM)/λ and K = 2sinθ/λ. FWHM is the full width at half maximum of a diffracted peak and λ is the wavelength of the used radiation; D is the crystallite size and $\varepsilon_{\text{lattice}}$ can be assumed as a lattice-strain dependent parameter; $\bar{C}_{h00}$ is a constant adopted as being 0.332 and 0.285 for γ and α'-martensite, respectively (ÚNGAR, 1999). H^2 is defined as $(h^2k^2 + h^2l^2 + k^2l^2)/(h + k + l)^2$ (ÚNGAR, 1999). The values of q (dislocation character) were determined as those which promoted the best linear fit between the terms ΔK and $K^2 \cdot \bar{C}_{h00} \cdot (1 - qH^2)$ (ÚNGAR, 1999).

2.3.1.5 Instrumental contribution

For the above mentioned XRD analysis, one must bear in mind the additional contribution for peak broadening arising from the geometry of the diffractometer. Before conducting any XRD analysis it is imperative to determine the instrumental broadening and separate it from the diffracted data. For this purpose, one standard material with large coherent domains sizes and nearly absent of crystallographic defects is submitted to XRD

Figure 2.1 - Peak width of a standard-Si used for evaluating the instrumental contribution. The width of each peak is represented by the full width at half maximum (FWHM) and integral breath (β), both plotted as a function of the diffracted angle (2θ).

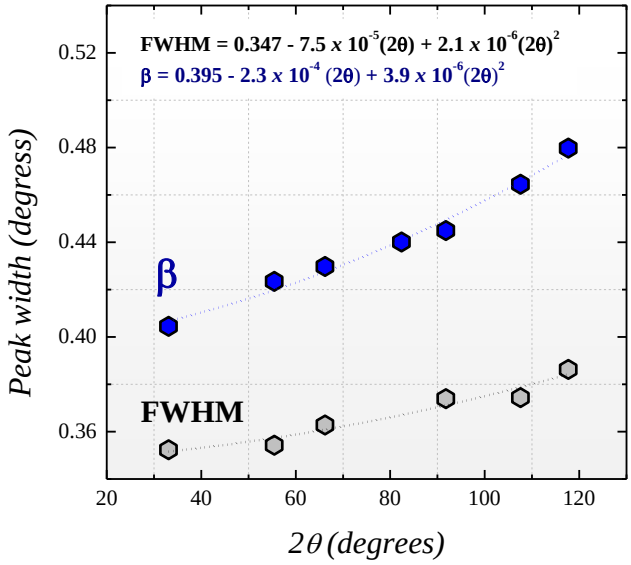

Source: elaborated by the author.

Measurements in the same 2θ range used for the investigated samples. After obtaining a diffractogram for the standard, the values of FWHM (or integral breath, β) of each peak are measured and plotted as a function of 2θ. The experimental points are thus fitted by a parabolic function, as shown in Fig. 2.1 for the standard-Si used in this work. In this figure, the width of the peaks was evaluated in terms of both FWHM and β. In this work, the instrumental contribution was evaluated using the behavior of FWHM.

Assuming that the peak broadening arising from lattice distortion is described by a Gaussian function (Section 2.4.1.1), the instrumental contribution can be subtracted from the diffracted data as follows:

$$FWHM_{real} = \sqrt{FWHM^2_{experimental} - FWHM^2_{standard}} \qquad (2.11)$$

where $FWHM_{experimental}$ is the FWHM obtained from the investigated sample and $FWHM_{standard}$ is the FWHM described by the function displayed in Fig. 2.1.

2.3.2 Microstructural characterization

Microstructural characterization was performed by means of electron backscatter diffraction (EBSD) using a JEOL-6500F field-emission scanning electron microscope (SEM), installed at the MPIE (Düsseldorf). High resolution EBSD maps were acquired with

a step size of 50 nm at a working distance of 18 mm. Confidence index (CI) standardization was adopted as a cleanup procedure. All data with CI below 0.1 were removed from the maps. Crystallographic aspects were also assessed from the EBSD maps. Local misorientation gradients were evaluated by means of the kernel average misorientation (KAM) parameter, constructed using the third neighbors (WRIGHT; NOWELL; FIELD, 2011). Submicron structural defects at representative strain levels were evaluated with the aid of electron channeling contrast image (ECCI) technique using a Zeiss Merlin SEM, installed at the MPIE (Düsseldorf). Scanning transmission electron microscopy (STEM) were carried out using an aberration-corrected FEI Titan Themis 60-300 microscope, operated at 300 kV. Vickers microhardness testing was carried out on the longitudinal section of the samples using a load of 200 g for 30 s.

2.3.3 Magnetic measurements

For magnetic measurements, samples were cut from the plates of the high-Mn steel using a low-speed diamond wheel saw with dimensions of approximately 5 x 1 x 1 mm^3. The largest dimension (5 mm) was obtained parallel to the rolling direction of the sheet (// RD). Different sets of experiments were conducted as follows:

I) Hysteresis loops at room temperature were obtained for the ε = 0, 0.22, 0.51, 0.92, 1.20, and 1.56 deformed samples (or equivalent thickness reductions of 0, 20, 40, 60, 70, and 80%). These measurements were performed using a vibrating sample magnetometer (VSM) from EG&G Princeton Applied Research, installed at the Institute of Physics (IF-USP). In all cases, the field was applied parallel to the RD.

II) *In-situ* magnetic measurements were obtained during continuous annealing. For these measurements, one sample from the 80% cold-rolled material was annealed from room temperature to 800°C with a heating rate of 3°C/min. The heating process was performed in the presence of a fixed external field of ~ 90 Oe, which promotes a magnetization (M) of ~ 10% of M_s at room temperature. Such experiment was performed under high-purity argon (99.999%) flow using a VSM Lake Shore model 7404, also installed at IF-USP.

III) 80% cold-rolled samples were isothermally annealed in the temperature range of 400-800°C during several time intervals (5-120 min) followed by air-cooling. After cooling, hysteresis loops were obtained at room temperature, as described

in (I). In this work, the temperatures used for isothermal annealing will be identified as "$T_{isothermal}$".

IV) 80% cold-rolled samples were isothermally annealed at 800°C during several time intervals (5-120 min) in a VSM Lake Shore model 7404. After annealing, an external fixed field was applied, as described under item II. The magnetic response of each sample was tracked during cooling down to room temperature using a rate of -3°C/min. In this case, the cooling temperature was defined in the text as "$T_{cooling}$".

From all hysteresis loops the corresponding coercive field (H_c) and saturation magnetization (M_s) were taken with an accuracy of ± 5 Oe and 2%, respectively.

2.3.4 Dilatometry experiments

For dilatometry, samples were cut from the 80% cold-rolled steel with dimensions of 10 x 1.56 x 5 mm^3, with the largest dimension (L_o = 10 mm) taken parallel to the rolling direction (RD). The relative changes in length of the material $\left(\frac{\Delta L}{L_0}\right)$ were tracked using a Linseis L75 Platinum dilatometer. Annealing was conducted from room temperature up to temperatures of 505, 660, and 800°C. In all treatments, heating and cooling rates were 0.05°C/s and -0.05°C/s, respectively. All experiments were performed under argon atmosphere.

2.3.5 Thermodynamic and thermo-kinetic simulations

Based on the chemical composition of the steel (Table 2.1), stability of the phases in thermodynamic equilibrium was calculated using Thermo-Calc in conjunction with the database TCFE9 (HUANG, 1989; DJUROVIC et al., 2010; DJUROVIC et al., 2011). Additionally, the diffusion-controlled phase transformation was simulated using DICTRA in conjunction with the mobility database MOBFE4 (INDEN; NEUMANN, 1996; BORGENSTAM et al., 2000; SCHNEIDER; INDEN, 2005).

2.3.6 Atom Probe Tomography (APT)

APT measurements were performed for the sample subjected to dilatometry interrupted at 505°C and for the sample isothermally annealed at 600°C for 5 min. Needle-shape specimens were prepared for APT using a FEI Helios 600i dual-beam FIB/SEM, installed at the MPIE (Düsseldorf). For extraction of the specimens, a FIB lift-out method

was adopted as reported in ref. (THOMPSON et al., 2007). All specimens were mounted on Si micro-tips and sharpened by annular ion milling. APT was performed on a LEAP 5000 XS straight flight path instrument (MPIE, Düsseldorf) for highest reconstruction accuracy at 60 K in laser-pulse mode operated at 40 pJ pulse energy. The wavelength, pulse and detection rates of the laser were 355 nm, 500 kHz and 1.5 ions detected on average per 100 pulses, respectively. For data reconstruction and evaluation, the Cameca IVAS® analysis software was used following the protocol reported by Geiser and co-authors (GEISER et al., 2009).

Chapter 3

Thermodynamic assessment

3.1 Thermodynamic modelling for Staking Fault Energy (SFE) calculation

Adopting the chemical composition displayed in Table 2.1, the stacking fault energy (SFE) of the present steel were estimated using the regular solid solution model reported in Refs. (SAEED-AKBARI et al., 2009, ALLAIN et al., 2004). The SFE can be assumed as the free energy required for creating one ε-martensite plate composed of two atomic layers (ALLAIN et al., 2004). As proposed by Olson and Cohen (1976), the SFE can be evaluated by means of the following expression:

$$SFE = 2\,\rho\,\Delta G^{\gamma\rightarrow\varepsilon} + 2\,\sigma^{\gamma/\varepsilon} \qquad (3.1)$$

where ρ the molar surface density along the {111} planes and can be determined as being $\rho = \frac{4}{\sqrt{3}} \cdot \frac{1}{a^2 N}$. In this context, "a" is the austenite lattice parameter and *N* the Avogadro constant; $\Delta G^{\gamma\rightarrow\varepsilon}$ is the free energy associated to the reaction $\gamma \rightarrow \varepsilon$; and $\sigma^{\gamma/\varepsilon}$ is the interfacial energy between austenite and ε-martensite (γ/ε), varying between 5 e 10 mJ/m^2 (YANG; WAN, 1990; LEE; CHOI, 2000; LEE, 2002).

For the Fe-Mn-Al-Si-C system, $\Delta G^{\gamma\rightarrow\varepsilon}$ can be calculated by means of the regular solid solution model expressed by the following formalism (SAEED-AKBARI et al., 2009; ALLAIN et al., 2004):

$$\begin{aligned}\Delta G^{\gamma\rightarrow\varepsilon} = {} & X_{Fe}\Delta G_{Fe}^{\gamma\rightarrow\varepsilon} + X_{Mn}\Delta G_{Mn}^{\gamma\rightarrow\varepsilon} + X_{Al}\Delta G_{Al}^{\gamma\rightarrow\varepsilon} + X_{Si}\Delta G_{Si}^{\gamma\rightarrow\varepsilon} + X_{C}\Delta G_{C}^{\gamma\rightarrow\varepsilon} \\ & + X_{Fe}X_{Mn}\Delta\Omega_{FeMn}^{\gamma\rightarrow\varepsilon} + X_{Fe}X_{Al}\Delta\Omega_{FeAl}^{\gamma\rightarrow\varepsilon} + X_{Fe}X_{Si}\Delta\Omega_{FeSi}^{\gamma\rightarrow\varepsilon} + X_{Fe}X_{C}\Delta\Omega_{FeC}^{\gamma\rightarrow\varepsilon} \\ & + X_{Mn}X_{C}\Delta\Omega_{MnC}^{\gamma\rightarrow\varepsilon} + \Delta G_{mag}^{\gamma\rightarrow\varepsilon} \qquad (3.2)\end{aligned}$$

where X_i and $\Delta G_i^{\gamma\rightarrow\varepsilon}$ correspond to the molar fraction of the element "*i*" and to the energy associated to the transformation $\gamma\rightarrow\varepsilon$ in pure metals, respectively; $\Delta\Omega_{ij}^{\gamma\rightarrow\varepsilon}$ is the interaction energy between the elements "*i*" e "*j*". $\Delta G_{mag}^{\gamma\rightarrow\varepsilon}$ is the energy associated to the magnetic transition between the paramagnetic state of austenite and the anti-ferromagnetic state of the ε-martensite. All energies from Eq. (3.2) are given in J/mol.

As suggested by Saeed-Akbari and co-authors (2009), C is treated as a substitutional element in the formalism of Eq. (3.2), although it is an interstitial element in both bcc and fcc-Fe. Besides, the interaction Mn-Al and Al-C are negligible in Fe-containing alloys as in the present case. Later, it will be demonstrated that Ni plays a minor effect on austenite reversion and therefore, for the sake of simplicity, here Ni was also neglected in Eq. (3.2).

The parameters $\Delta G_i^{\gamma\to\varepsilon}$ and $\Delta\Omega_{ij}^{\gamma\to\varepsilon}$ can be found in Refs. (DINSDALE, 1991; LEE; CHOI, 2000; PIERCE et al., 2014; YANG; WAN, 1990; HUANG, 1989; HAMADA, 2007; ADLER; OLSON; COHEN, 1986) and are summarized in Table 3.1.

Table 3.1 - Representation of the parameters $\Delta G_i^{\gamma\to\varepsilon}$ and $\Delta\Omega_{ij}^{\gamma\to\varepsilon}$ adopted to calculate the free energy associated to the transformation $\gamma \to \varepsilon$ ($\Delta G^{\gamma\to\varepsilon}$). T is the temperature given in Kelvin.

Thermodynamic parameters and corresponding functions	Reference
$\Delta G_{Fe}^{\gamma\to\varepsilon} = -2243.38 + 4.309 \cdot T$	(DINSDALE, 1991)
$\Delta G_{Mn}^{\gamma\to\varepsilon} = -1000 + 1{,}123 \cdot T$	(DINSDALE, 1991)
$\Delta G_{Al}^{\gamma\to\varepsilon} = 2800 + 5 \cdot T$	(LEE; CHOI, 2000)
$\Delta G_{Si}^{\gamma\to\varepsilon} = -560 - 8 \cdot T$	(PIERCE et al., 2014)
$\Delta G_{C}^{\gamma\to\varepsilon} = -22166$	(YANG; WAN, 1990)
$\Delta\Omega_{FeMn}^{\gamma\to\varepsilon} = 2180 + 532 \cdot (X_{Fe} - X_{Mn})$	(HUANG, 1989)
$\Delta\Omega_{FeAl}^{\gamma\to\varepsilon} = 3323$	(HAMADA, 2007)
$\Delta\Omega_{FeSi}^{\gamma\to\varepsilon} = -106149 + (41.116 \cdot T) - [191658 \cdot (X_{Fe} - X_{Si})] + [123574 \cdot (X_{Fe} - X_{Si})^2] - \{-125248 + (41.116 \cdot T) - [142708 \cdot (X_{Fe} - X_{Si})] + [89907 \cdot (X_{Fe} - X_{Si})^2]\}$	(PIERCE et al., 2014)
$\Delta\Omega_{FeC}^{\gamma\to\varepsilon} = 42500$	(ADLER; OLSON; COHEN, 1986)
$\Delta\Omega_{MnC}^{\gamma\to\varepsilon} = 26910$	(YANG; WAN, 1990)

Source: elaborated by the author.

Back to Eq. (3.2), the magnetic transition parameter $\Delta G_{mag}^{\gamma\to\varepsilon}$ is represented by the following expression:

$$\Delta G_{mag}^{\gamma\to\varepsilon} = G_{mag}^{\varepsilon} - G_{mag}^{\gamma} = RT\left[ln\left(1 + \frac{\beta^{\varepsilon}}{\mu B}\right) f\left(\frac{T}{T_N^{\varepsilon}}\right) - ln\left(1 + \frac{\beta^{\gamma}}{\mu B}\right) f\left(\frac{T}{T_N^{\gamma}}\right)\right] \quad (3.3)$$

In this case, β , μB, and T_N correspond respectively to the magnetic moment, Bohr magneton, and Néel temperature (Kelvin) for both γ e ε phases (ALLAIN et al., 2004). These parameters can be obtained by means of the following expressions (SAEED-AKBARI et al., 2009):

$$\frac{\beta^{\varepsilon}}{\mu B} = 0.62 \cdot X_{Mn} - 4X_C \quad (3.4)$$

$$\frac{\beta^{\gamma}}{\mu B} = 0.7X_{Mn} + 0.62X_{Mn} - 0.64 \cdot X_{Fe}X_{Mn} - 4X_C \quad (3.5)$$

$$T_N^{\gamma} = 669.271 \cdot [1 - \exp(-5.46X_{Mn})] - 0.241X_C(1 - X_{Mn} - X_C) - 109 \quad (3.6)$$

$$T_N^{\varepsilon} = 580X_{Mn} \quad (3.7)$$

For the present case and considering the room temperature (298 K), it will be demonstrated in Table 3 that both ratios $\frac{T}{T_N^{\varepsilon}}$ e $\frac{T}{T_N^{\gamma}}$ are higher than the unity. Therefore, the function $f\left(\frac{T}{T_N^{\varphi}}\right)$ in Eq. (3.3) is given by (SAEED-AKBARI et al., 2009):

$$f = -\frac{\left[\frac{1}{10}\cdot\left(\frac{T}{T_N^{\varphi}}\right)^{-5} + \frac{1}{315}\cdot\left(\frac{T}{T_N^{\varphi}}\right)^{-15} + \frac{1}{1500}\cdot\left(\frac{T}{T_N^{\varphi}}\right)^{-25}\right]}{2{,}342456517} \quad (3.8)$$

where φ represents the γ e ε phases.

The first column of Table 3.2 shows the molar fraction (X_i) of the chemical elements of the studied steel (previously shown in Table 2.1 in the form of weight and atomic percentage). By using the values of X_i, the functions displayed in Table 3.1, and also the Equations (3.3-3.8), the values of $\Delta G_i^{\gamma\to\varepsilon}$, $\Delta\Omega_{ij}^{\gamma\to\varepsilon}$, $\frac{\beta^{\varphi}}{\mu B}$, $\frac{T}{T_N^{\varphi}}$ e f^{φ} were obtained as displayed in Table 3.2.

Table 3.2 - Respective values of $\Delta G_i^{\gamma\to\varepsilon}$, $\Delta\Omega_{ij}^{\gamma\to\varepsilon}$, $\frac{\beta^{\varphi}}{\mu B}$, $\frac{T}{T_N^{\varphi}}$ e f^{φ} for the studied high-Mn steel.

X_i	$\Delta G_i^{\gamma\to\varepsilon}$(J/mol)	$\Delta\Omega_{ij}^{\gamma\to\varepsilon}$ (J/mol)	$\frac{\beta^{\varphi}}{\mu B}$	$\frac{T}{T_N^{\varphi}}$	$f^{\varphi}(10^{-3})$
X_{Fe} = 0.7342	$\Delta G_{Fe}^{\gamma\to\varepsilon}$= -959.3	$\Delta\Omega_{FeMn}^{\gamma\to\varepsilon}$= 2480,4	$\frac{\beta^{\varepsilon}}{\mu B}$ = 0.105	$\frac{T}{T_N^{\varepsilon}}$ = 1.55	f^{ε} = -0.17
X_{Mn} = 0.1697	$\Delta G_{Mn}^{\gamma\to\varepsilon}$= -665.4	$\Delta\Omega_{FeAl}^{\gamma\to\varepsilon}$ = 3323	$\frac{\beta^{\gamma}}{\mu B}$ = 0.557	$\frac{T}{T_N^{\gamma}}$ = 3.03	f^{γ} = -4.70
X_{Al} = 0.0336	$\Delta G_{Al}^{\gamma\to\varepsilon}$= -4290	$\Delta\Omega_{FeSi}^{\gamma\to\varepsilon}$ =1402,6			
X_{Si} = 0.0607	$\Delta G_{Si}^{\gamma\to\varepsilon}$= 2944	$\Delta\Omega_{FeC}^{\gamma\to\varepsilon}$ = 42500			
X_C = 0.0019	$\Delta G_C^{\gamma\to\varepsilon}$= -22166	$\Delta\Omega_{MnC}^{\gamma\to\varepsilon}$ = 26910			

Source: elaborated by the author.

Based on the values displayed in Table 3.2 and on the Equations (3.2) and (3.3), the parameters $\Delta G_{mag}^{\gamma\to\varepsilon}$ e $\Delta G^{\gamma\to\varepsilon}$ for the present steel were obtained as being 5.13 J/mol and -373.41 J/mol, respectively. Using Eq. (3.1) and assuming ρ = 2,98 x 10^{-5} mol/m^2 (SOUZA

FILHO et al., 2019a) and $\sigma^{\gamma/\varepsilon}$ = 15 mJ/m^2 as suggested in the literature (SAEED-AKBARI et al., 2009), a SFE of ~ 8.1 mJ/m^2 was obtained. Therefore, the steel investigated in this work belongs to the low-SFE series of high-Mn steels and both TRIP and TWIP effects can be expected to operate simultaneously upon deformation.

3.2 Phase stability (equilibrium conditions)

Figure 3.1 shows the diagram of phase equilibrium for the high-Mn steel studied in this work. Based on the chemical composition displayed in Table 2.1 (Section 2.1), this diagram was calculated with the aid of the software Thermo-Calc coupled with the database TCFE-9. From this figure, the melting point is observed to be ~ 1370°C and the solidification mechanism is ferritic (viz., Liquid → Liquid + δ → Liquid + δ + γ → δ + γ). Fig. 3.1 also evidences the precipitation of AlN and MnS directly from the liquid at ~ 1600 and ~ 1300°C, respectively. Besides, once formed both phases are pinned as residual phases in the final solidified microstructure. The austenite (γ)-single phase field is found between ~ 1294 and 585°C. For temperatures lower than 655°C, γ can undergo a slightly decomposition into Fe_3P. The intercritical field (α + γ), in turn, ranges between ~ 585 and ~ 400°C and coexists

Figure 3.1 - Phase stability of the high-Mn steel studied in this work, calculated with the aid of the software Thermo-Calc (database TCFE-9).

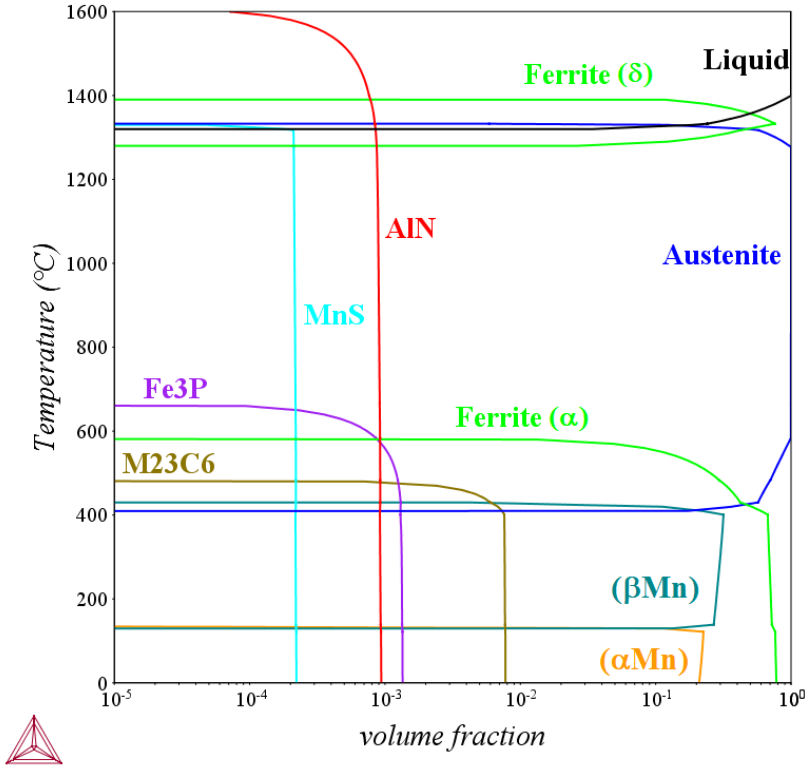

Source: elaborated by the author.

with the precipitation of $M_{23}C_6$ for temperatures lower than 473°C. The intercritical field of this steel will better evaluated in Chapter 5. Finally, the decomposition of the bcc-ferrite into the Mn-solid solutions, namely (βMn) and (αMn), is expected to take place bellow 426°C.

3.3 Austenite stability

The diagram depicted in Fig. 3.1 was calculated for long-term conditions of the equilibrium. However, the stability of austenite in high-Mn steels is also strongly dependent on its SFE. For high-Mn steel belonging to the Fe-Mn-Al-Si-C system, it has been demonstrated that SFEs lower than 20 mJ/m^2 favor the γ → ε transformation during cooling (SAHU et al., 2007). In the Section 3.1, it was determined that the SFE for the present steel is ~ 8.1 mJ/m^2. Thus, the γ → ε and ε → α' reactions are expected to occur upon cooling of austenite (e.g. from 800°C to room temperature). Such reactions are also influenced by the primary austenite grain size and cooling rate (DAFÉ et al., 2013). Under fast cooling rates (quenching), the formation of martensite can be ruled either by an athermal process or induced by thermal stresses (PISARIK, VAN AKEN, 2014). Contrastingly, slow cooling rates can partially suppress the martensitic transformation induced by cooling.

Based on the above statement and in order to obtain a microstructure mainly composed of austenite, the plate of the high-Mn steel was annealed at 800°C for 15 min and cooled under the furnace inertia. This temperature is found in the γ-single phase field and above the stability of the Fe_3P intermetallic (Fig. 3.1). The relative short annealing time was also chosen to avoid grain growth. Fig. 3.2 shows the microstructure of the steel represented

Figure 3.2 - Microstructure of the high-Mn steel annealed at 800°C for 15 min and cooled under the furnace inertia. Austenite, ε- and α'-martensite are represented in green, yellow and red, respectively.

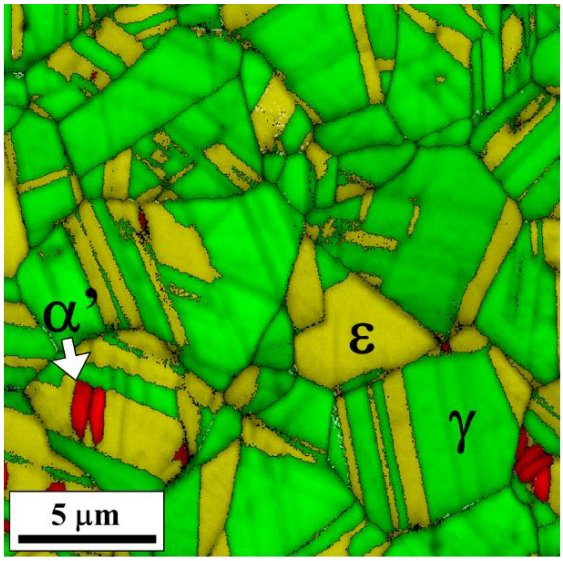

Source: elaborated by the author.

by means of phase map obtained via EBSD. The obtained microstructure is fully recrystallized and austenite is partially subdivided by athermally-formed ε-plates. Small traces of athermal α'-martensite is also found within the ε-plates. The athermal martensitic transformations will be investigated in Chapter 6.

3.4 Chemical composition

In order to evaluate the possible macro-segregation of elements, EDS measurements were conducted for the steel deformed to 80% of thickness reduction by cold rolling (Section 2.2). Fig. 3.3 (a) shows the analyzed area, imaged via the secondary electrons (SE) mode. In this figure, it is possible to observe the presence of inclusions aligned parallel to the rolling direction (RD). Details of these inclusions are revealed in the inset of Fig. 3.3 (a). The composition map displayed in Fig. 3.3 (e) confirms that these inclusions are enriched in Al. Slight Si-accumulations are also noticed in the vicinity of the inclusions, as evidenced

Figure 3.3 - Qualitative chemical analysis obtained via EDS measurements for the high-Mn steel (deformed to 80%). **(a)** Analyzed area, imaged via SE mode. Composition maps in terms of **(b)** Fe; **(c)** Mn; **(d)** Si; **(e)** Al; **(f)** Ni.

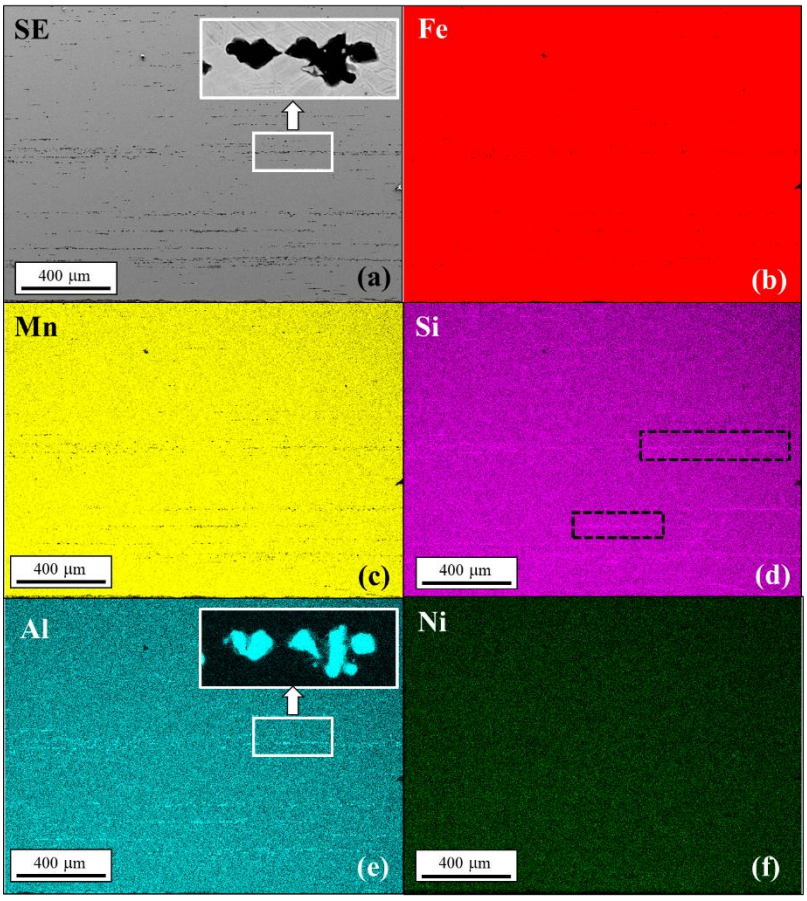

Source: elaborated by the author.

out by the frames in Fig. 3.3 (d). In spite of these minor local concentrations of Al and Si, the matrix is chemically homogeneous and no macro-segregations is observed, especially in terms of Mn. Small traces of Ni, corresponding to ~ 1.1 wt.% was also detected by the EDS analysis (Fig. 3.3f). The composition of Mn, Al, and Si in the matrix was found to be 17.4, 1.79, and 2.95 wt.%, respectively. A reasonable agreement is found between the chemical composition obtained via EDS and the one reported in Table 2.1 (ZORZI, 2014).

Chapter 4
Strain hardening mechanisms during cold rolling: interplay between submicron defects and microtexture

4.1 Introduction

There is a raising interest in high-Mn steels containing 15-25 wt.% Mn as they enable the reduction of body-car weight without compromising crashworthiness properties (FROMMEYER; BRÜX, 2006; DE COOMAN; CHIN; KIM, 2011; KIM; SUH; KIM, 2013; RAABE et al., 2014; ZHANG; RAABE; TASAN, 2017). The steels have very good mechanical properties and high ductility, enabled by the interplay of several complex strain hardening mechanisms. The stacking fault energy (SFE) of these alloys ranges between 10 and 21 mJ/m^2 (GAZDER et al., 2015; PRAMANIK et al., 2018a). Therefore, the metastable austenite (γ) in these low-SFE materials can accommodate deformation by means of partial dislocation slip, mechanical twinning, and / or transforming into ε- (hcp) or α'-martensite (bcc) (LEE; CHOI, 2000; DING et al., 2011; STEINMETZ et al., 2013). Upon straining, the dissociation of perfect dislocations into Shockley partials promotes the formation of stacking faults (SFs) which can eventually lead to the formation of twins and ε-phase (PRAMANIK et al., 2018b). In this context, twinning and ε-formation take place through the motion of Shockley partial dislocations on successive and alternating (111) planes of γ, respectively (BRACKE; KESTENS; PENNING, 2007; PRAMANIK et al., 2018b). With regard to α'-martensite, its formation has been observed to occur at the intersection of crystallographic defects created during deformation, including ε-martensite (BRACKE; KESTENS; PENNING, 2007). When the ε-phase intermediates the α'-formation ($\gamma \rightarrow \varepsilon \rightarrow \alpha'$), excellent strain hardening rates are observed upon deformation of high-Mn alloys (REMY; PINEAU, 1977; SATO; SOMA; MORI, 1982; ALLAIN et al., 2004; PISARIK; VAN AKEN, 2016). Once α'-martensite is the major phase, further deformation is accommodated in this phase by slip and shear banding (PRAMANIK et al., 2018b).

Prior to the $\varepsilon \rightarrow \alpha$' reaction, the motion of Shockley partials on the basal (0001) planes of the ε-martensite leads to the creation of intrinsic and extrinsic SFs, and also twins (PRAMANIK et al., 2018b); i.e., ε-martensite accommodates its incommensurate deformation by faults and twins. Recently, some works focused on straining of the ε-phase in Fe-Mn (KIM; DE COOMAN, 2017), Fe-Mn-C (SAHU et al., 2012), and Fe-Mn-Al-Si-C

(PRAMANIK et al., 2018b) systems. A few studies also reported about austenite in cold-rolled high-Mn steels, whose SFEs range within the interval of 12-29 mJ/m^2 (SAHU et al., 2012; BERRENBERG et al., 2017; YANUSHKEVICH et al., 2018). However, the hierarchical formation of planar defects (e.g. SFs and twins) in metastable γ and ε-martensite in high-Mn steels with SFE < 10 mJ/m^2 remains barely explored. Only a few studies have dealt with the interplay between the evolution of submicron defects and texture (GAZDER et al., 2015). In fact, studies of crystallographic texture have mainly been conducted for high-Mn steels displaying SFEs higher than 10 mJ/m^2 (GAZDER et al., 2015; BERRENBERG et al., 2017; YANUSHKEVICH et al., 2018). Therefore, the aim of the present Chapter is to throw light on the strain hardening mechanisms of high-Mn alloys with a lower SFE than those reported in refs. (GAZDER et al., 2015; PRAMANIK et al., 2018b; SAHU et al., 2012; KIM; DE COOMAN, 2017; BERRENBERG et al., 2017; YANUSHKEVICH et al., 2018). Also, the aim of obtaining better understanding of the complex superposition and interaction of several displacive and incommensurate transformation reactions, including γ → SFs, γ → twins, SFs as precursor for twins or ε, and γ → ε → α', was also taken as motivation for the present work.

Here, a systematic study of submicron structural defects evolution and their relationship with microtexture is presented for a cold-rolled 17.6 wt.% Mn steel with a SFE of ~ 8.1 mJ/m^2 (Section 3.1). For this purpose, the steel was cold rolled up to 80% thickness reduction and characterized by several probing including X-ray diffraction (XRD), electron channeling contrast image (ECCI) technique, electron backscatter diffraction (EBSD), and Vickers microhardness testing. From XRD data, the Warren's theory (1969) for planar defects in fcc and hcp structures was combined with ECCI (GUTIERREZ-URRUTIA; ZAEFFERER; RAABE, 2009; GUTIERREZ-URRUTIA; RAABE, 2011; GUTIERREZ-URRUTIA; ZAEFFERER; RAABE, 2013) to elucidate how stacking faults and twins evolve within the γ and ε-phases during cold rolling. For such a task, statistical reliability is one of the advantages of ECCI over transmission electron microscopy (TEM) (GUTIERREZ-URRUTIA; ZAEFFERER; RAABE, 2009). Furthermore, with the aid of the Popa model (POPA, 1998) for evaluation of XRD data, namely, *size-strain analyzes*, the evolution of the coherent domains size and accumulated microstrain was followed. These parameters were posteriorly used to estimate the dislocation density at several strain levels. The changes in dislocation character during deformation were also inferred using the modified Williamson-Hall method (ÚNGAR et al., 1999). By tracking the dislocation densities and character in

all γ, ε, and α'-phases, a complete hierarchy of strain accommodation mechanisms upon cold rolling in a submicron scale is proposed. Localized strain gradients induced by the ε-formation in the early beginning of rolling was also evaluated by combining misorientation analysis from EBSD data (WRIGHT; NOWELL; FIELD, 2011) with ECCI imaging (SOUZA FILHO, et al., 2017). Due to the ever-smaller fractions of austenite and ε-martensite with rolling, microtexture analysis performed via EBSD is the most suitable tool for evaluating crystallographic aspects (WRIGHT; NOWELL; FIELD, 2011). In this context, the evolution of submicron structural defects in all phases was further correlated with the microtexture of the 17.6 wt.% Mn steel. In this Chapter, the 7-mm-annealed plate (before cold-rolling) is referred to "as-received" steel.

4.2 Results

4.2.1 Phase evolution

Figure 4.1 shows the changes in the phase volume fraction of the 17.6 Mn steel during cold rolling. The as-received steel is primarily composed of austenite with relatively small fractions of athermal ε- (0.11) and α'-martensite (0.02). The fraction of α'-martensite increases with a near-parabolic behavior as a function of strain. The maximum amount of ε-martensite, in turn, is found at $\varepsilon = 0.11$. For further deformation, the fraction of ε-martensite

Figure 4.1 – Volume fraction of austenite, ε-, and α'-martensite in the 17.6 wt.% Mn steel as a function of the logarithmic equivalent strain (ε) obtained using the direct peak comparison method from X-ray diffraction data.

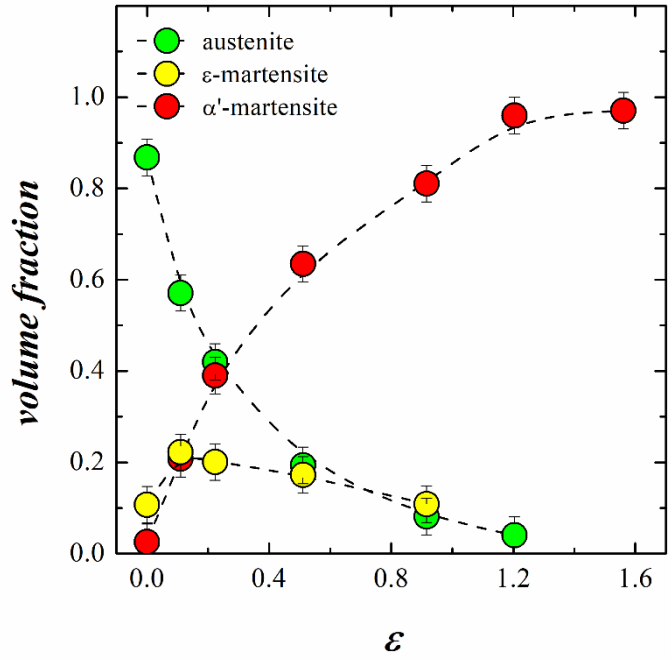

Source: elaborated by the author.

Decreases suggesting that it is an intermediate phase for α'-formation as reported for other austenitic steels (HERERRA; PONGE; RAABE, 2011; KISKO et al., 2013; SOUZA FILHO et al., 2016). At this point, it is worth mentioning that ε-martensite peaks presented low diffracted intensities for $\varepsilon > 0.92$. For this reason, these peaks were neglected for phase quantification from $\varepsilon = 0.92$ on. At the highest deformation level ($\varepsilon = 1.56$), Fig. 4.1 shows that strain-induced α'-martensite is the predominant phase in the microstructure.

4.2.2 XRD analyzes using the software MAUD

4.2.2.1 Rietveld refinement

Figure 4.2 illustrates a refined diffractogram for the steel deformed to $\varepsilon = 0.11$. The experimental and calculated data are represented by black squares and a red line, respectively. A detailed view of the frame in the main panel, as well as the corresponding deconvoluted peaks for austenite, ε- and α'-martensite can be visualized in the right-hand side inset. The lattice parameters obtained via Rietveld refinement are reported in Table 4.1 for all phases at each strain. In this table, the goodness of the fit (GoF) parameter indicates that all Rietveld analyzes hold very good reliability. Regarding austenite, its lattice parameter decreases with the progress of deformation likely due to elastic distortion imposed by deformation (SAHU et al., 2012). The lattice parameter of α'-martensite remains nearly unchanged. Similarly, ε-martensite lattice parameters, as well as its c/a ratio are practically the same up to $\varepsilon = 0.22$. Table 4.1 also shows that the c/a ratio is generally higher than the ideal value of 1.633. An anomalous behavior is observed at $\varepsilon = 0.51$ when c/a drops to 1.619. A similar finding was also reported by Sahu and co-authors (2012) for a cold-rolled 26Mn-0.14C steel (wt.%). These authors attributed this phenomenon to thermal expansion effects.

Table 4.1 - Evolution of the lattice parameter of austenite, ε- and α'-martensite during cold rolling, obtained via Rietveld refinement. The reliability of the analysis is evaluated by means of the goodness of fit (GoF) parameter.

Strain (ε)	austenite a ± 0.001 (nm)	ε-martensite c ± 0.001 (nm)	ε-martensite a ± 0.0005 (nm)	ε-martensite c/a	α'-martensite a ± 0.001 (nm)	GoF
0	0.3592	0.4132	0.2528	1.634	0.2871	1.35
0.11	0.3590	0.4133	0.2525	1.637	0.2876	1.32
0.22	0.3590	0.4134	0.2527	1.636	0.2871	1.27
0.51	0.3586	0.4100	0.2532	1.619	0.2873	1.40
0.92	0.3582	-	-	-	0.2874	1.39
1.20	0.3577	-	-	-	0.2874	1.36
1.56	-	-	-	-	0.2875	1.27

Source: elaborated by the author.

Figure 4.2 - Diffracted data obtained for the 17.6 wt.% Mn steel cold rolled at $\varepsilon = 0.11$ (black squares). The corresponding Rietveld refinement (calculated diffractogram) is represented by the red line. A detailed view of the frame in the main panel is depicted in the top right-hand side inset. The bottom right-hand side inset shows the corresponding deconvoluted peaks for austenite, ε and α'-martensite.

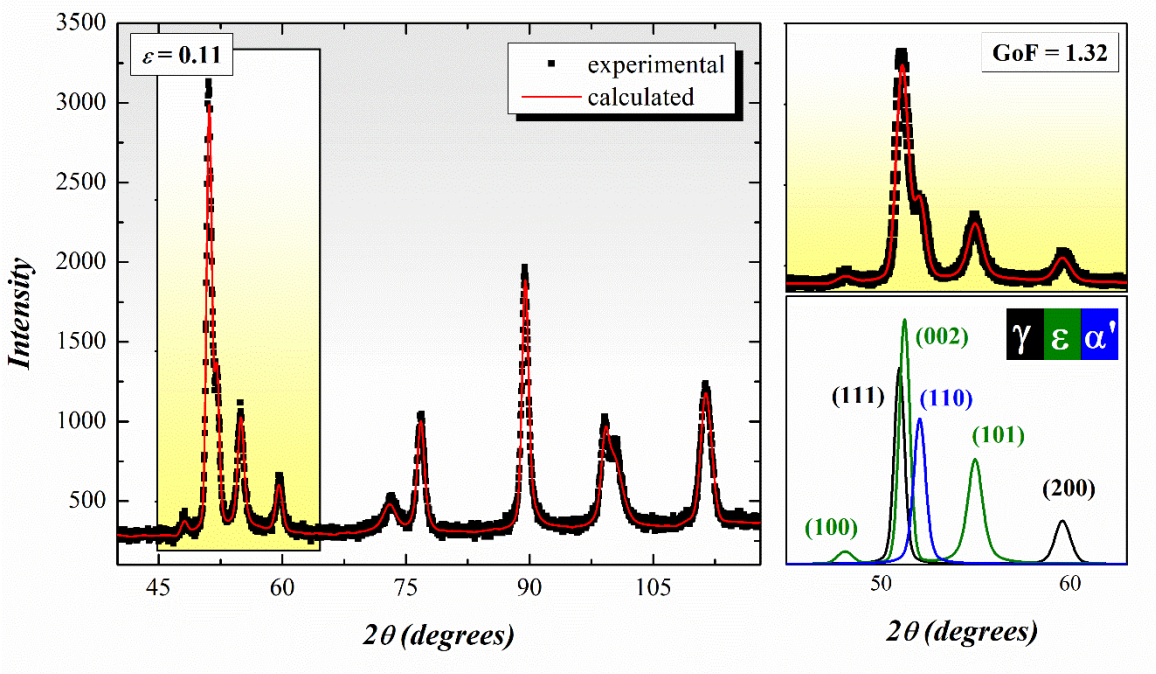

Source: elaborated by the author.

4.2.2.2 Size-strain analysis

The formation of extended crystallographic defects during deformation destroys the long-range-ordered arrangement of the crystal. Thus, the coherent diffraction domains (crystallites) are expected to become smaller with strain. As a result, peak broadening is readily observed in XRD analysis (ANAND et al., 2018). Analogously, short-range crystallographic defects (i.e., microstrain) are also responsible for creating aberrations on diffracted peaks and substructural changes can be followed by microstrain analysis (ÚNGAR, 2004). Since both, crystallite size and microstrain affect peak broadening, it is necessary to sort out both influences. In addition, there is a contribution of SFs and twinning on peak broadening as mentioned in Section 2.4.1.2. For this reason, it was used the combination of the Popa and Warren models to perform the *size-strain* analysis. These approaches allowed the separation of all contributions to peak broadening arising from crystallite size, microstrain and planar defects (LUTTEROTTI; SCARDI; MAITRELLI, 1990; LUTTEROTTI, 2006).

Figures 4.3 (a) and (b) show the evolution of the effective crystallite size (D_{eff}) and accumulated microstrain $<\varepsilon^2_{hh}>^{1/2}$ for all phases. From Fig. 4.3 (a), it is noticed relatively

Figure 4.3 - (a) Evolution of the effective crystallite size (D_{eff}) for all phases during cold rolling. **(b)** evolution of the accumulated microstrain $< \varepsilon^2_{hh}>^{1/2}$ values during cold rolling. Both parameters were obtained using the Popa model implemented in the software MAUD.

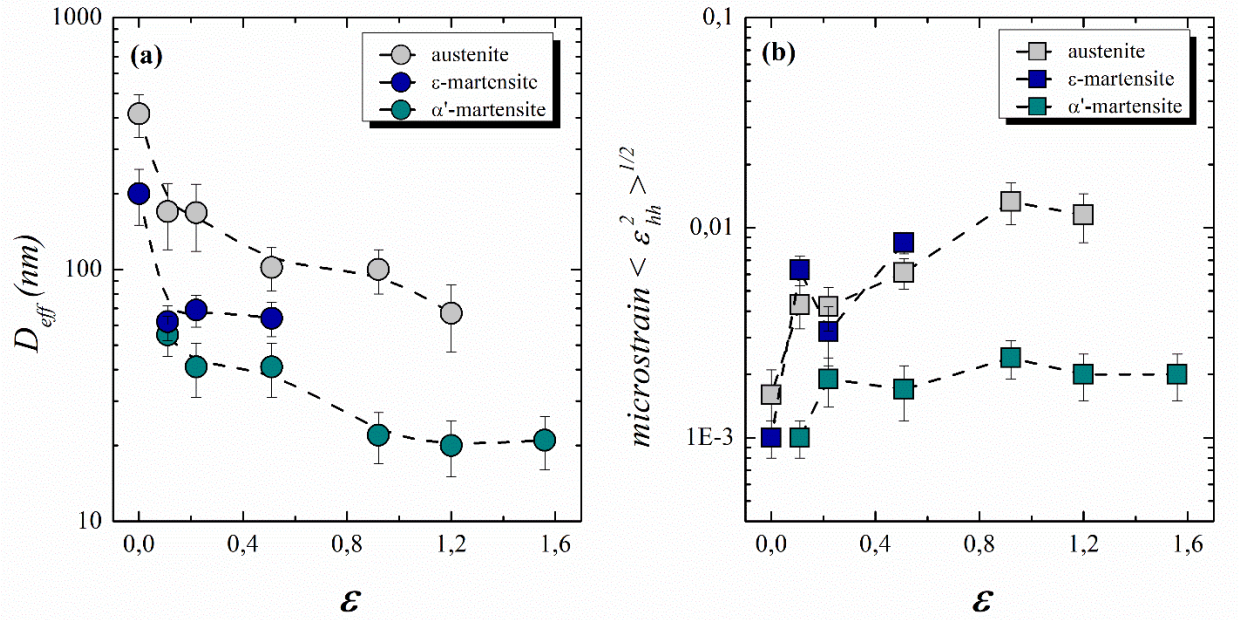

Source: elaborated by the author.

large diffraction domain sizes in the as-received condition. Over the course of deformation, austenite possesses the largest D_{eff} values. Regarding the α'-martensite, its D_{eff} values slightly drop from ~ 50 nm ($\varepsilon = 0.11$) to ~ 20 nm at $\varepsilon = 0.92$ and level off for larger strains. D_{eff} values for ε-phase decreases to ~ 65 nm at $\varepsilon = 0.22$ and remain nearly unchanged up to $\varepsilon = 0.51$. Fig. 4.3 (b) shows that the accumulated microstrain is rather low (10^{-3}) in the as-received steel, as expected for the fully recrystallized condition. Microstrains build up preferentially in both the γ and ε-phase as a function of rolling reduction, whereas strains in α' remain nearly constant at a low level of ~ 0.002 within the evaluated strain range.

4.2.2.3 Planar defects in austenite and ε-martensite

Figure 4.4 shows the behavior of the planar defects in both γ and ε-martensite, expressed in terms of their respective stacking fault (P_α) and twinning (P_β) probabilities. For the austenite Fig. 4.4 (a) shows that both P_α and P_β are negligible in the as-received condition ($\varepsilon = 0$). 10% thickness reduction ($\varepsilon = 0.11$), however, is sufficient to drastically increase the density of planar defects within γ. At this strain level, P_α increases to values of ~ 10^{-3} whilst P_β is even higher, namely one order of magnitude above P_α (~ 10^{-2}). At $\varepsilon = 0.22$, the austenite has the same probabilities for both SFs and twins (~ 8 *x* 10^{-3}). Interestingly, P_β and P_α split

Figure 4.4 - Probabilities of stacking fault formation (P_α) and twinning (P_β) within **(a)** austenite and **(b)** ε-martensite as a function of the logarithmic equivalent strain (ε). Both parameters were obtained with the aid of Warren's theory for planar defects in fcc and hcp metals implemented in software MAUD.

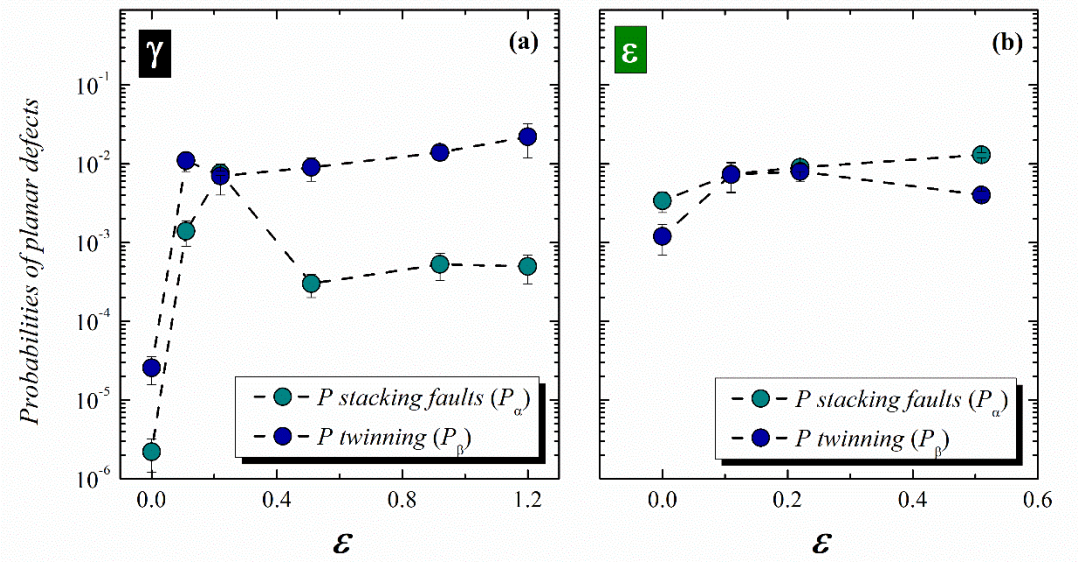

Source: elaborated by the author.

in population development at a medium strain of $\varepsilon = 0.51$, i.e. P_α drops to ~ 3 *x* 10^{-4} while P_β increases to ~ 9 *x* 10^{-3}. For strains above $\varepsilon = 0.51$, both parameters increase monotonically, yet maintaining a difference of about two orders of magnitude between them. With regard to Fig. 3.4 (b), ε-martensite in the as-received steel presents higher probabilities of SFs and twinning, when compared to austenite. An overall view of Fig. 4.4 (b) reveals that both P_β and P_β display similar trends and do not change significantly over the course of deformation. Only a slight decrease in P_β is noticed at $\varepsilon = 0.51$.

4.2.2.4 Dislocation density

The dislocation densities of austenite, ε- and α'-martensite were estimated by means of Eq. (2.9) and are displayed in Fig. 4.5. The dislocation density of austenite (ρ_γ) increases from ~ 1 *x* 10^{14} m^{-2} to ~ 7 *x* 10^{14} m^{-2} after 20% of thickness reductions ($\varepsilon = 0.22$). From this strain on, ρ_γ increases monotonously reaching a value of ~ 3 *x* 10^{15} m^{-2} at $\varepsilon = 1.2$. The athermal ε-martensite in the as-received steel presents nearly the same dislocation density (ρ_ε) as the starting austenite (~ 1 *x* 10^{14} m^{-2}). At $\varepsilon = 0.11$, ρ_ε increases one order of magnitude but drops to ~ 7 *x* 10^{14} at $\varepsilon = 0.22$. No significant modifications are observed for larger strains. Compared to the γ and ε-phases, strain-induced α'-martensite formed at $\varepsilon = 0.11$ has the lowest dislocation content ($\rho_{\alpha'}$ ~ 5 *x* 10^{14} m^{-2}). $\rho_{\alpha'}$ increases to values of ~ 3 *x*

Figure 4.5 - Evolution of the dislocation density in austenite, ε- and α'-martensite during cold rolling.

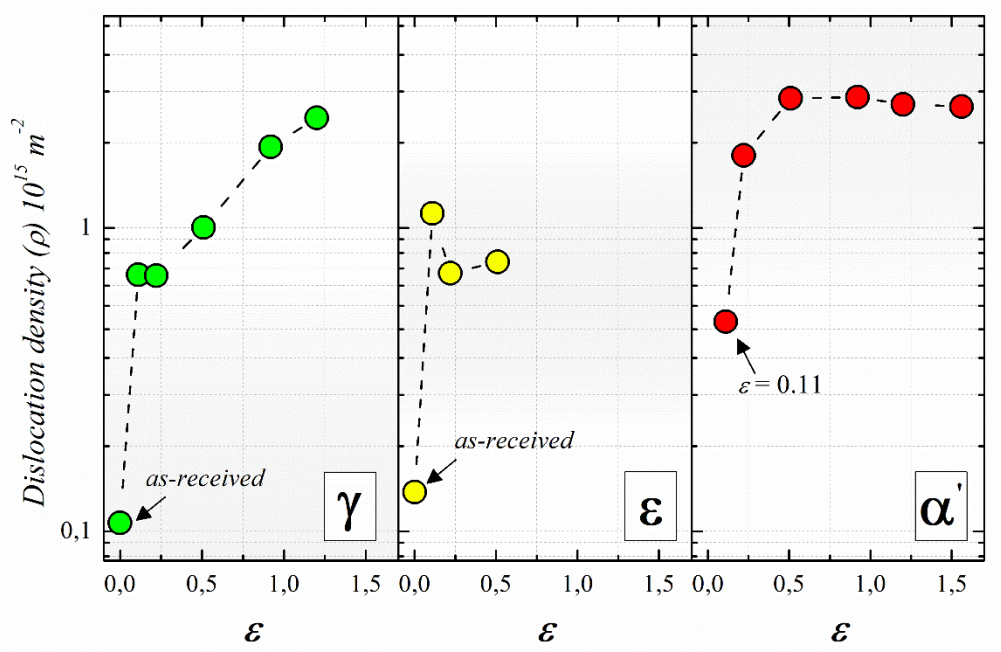

Source: elaborated by the author.

10^{15} m^{-2} at $\varepsilon = 0.51$ and levels off for larger strains. The dislocation densities of γ and α' are practically the same at $\varepsilon = 1.2$.

4.2.2.5 Dislocation character

The dislocation character (q parameter) in γ and α'-phases was evaluated by means of the modified Williamson-Hall method (Eq. 2.10). As previously mentioned, the values of q for each strain level were adopted as those which promoted the best linear fit for Eq. (2.10), as displayed in Fig. 4.6. Figs. 4.7 (a) and (b) show the changes in q values as a function of strain for γ and α', respectively. In this figure, the values of q for pure edge and pure screw dislocations were estimated adopting the procedure proposed by Úngar et al. (1999), using the elastic constants reported in ref. (PIERCE et al., 2013). It was found that pure edge and screw dislocations in the austenite display q values of ~ 1.20 and ~ 2.13, respectively. For α'-martensite, q varies from ~ 0.97 (edge dislocations) to ~ 2.64 (screw dislocations). Regarding austenite, Fig. 4.7 (a) shows that q decreases from ~ 2.5 in the as-received condition to ~ 2.0 at $\varepsilon = 0.51$. In other words, all q values lie in the vicinity of the upper limit of ~2.13, which suggests that the dislocations in austenite remain mostly of screw-type within the evaluated deformation range. In contrast, as revealed in Fig. 4.7 (b) dislocations in α'-martensite change from screw-type (q ~ 2.4) in the early beginning of rolling to edge-type (q ~ 1.2) at $\varepsilon = 1.56$. Such modification is a strong evidence that cross-slip of screw

Figure 4.6 - Modified Williamson-Hall plots for **(a)** austenite and **(b)** α'-martensite.

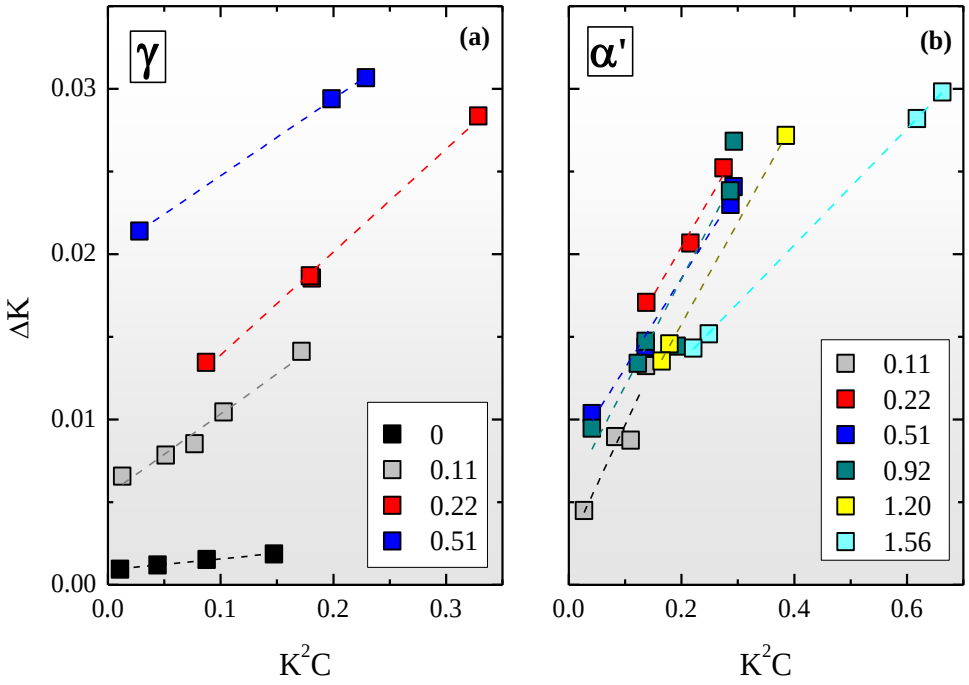

Source: elaborated by the author.

Figure 4.7 - Evolution of the dislocation character (*q* parameter) in **(a)** austenite and **(b)** α'-martensite during cold rolling. The values of *q* were obtained with the aid of the modified Williamson-Hall method.

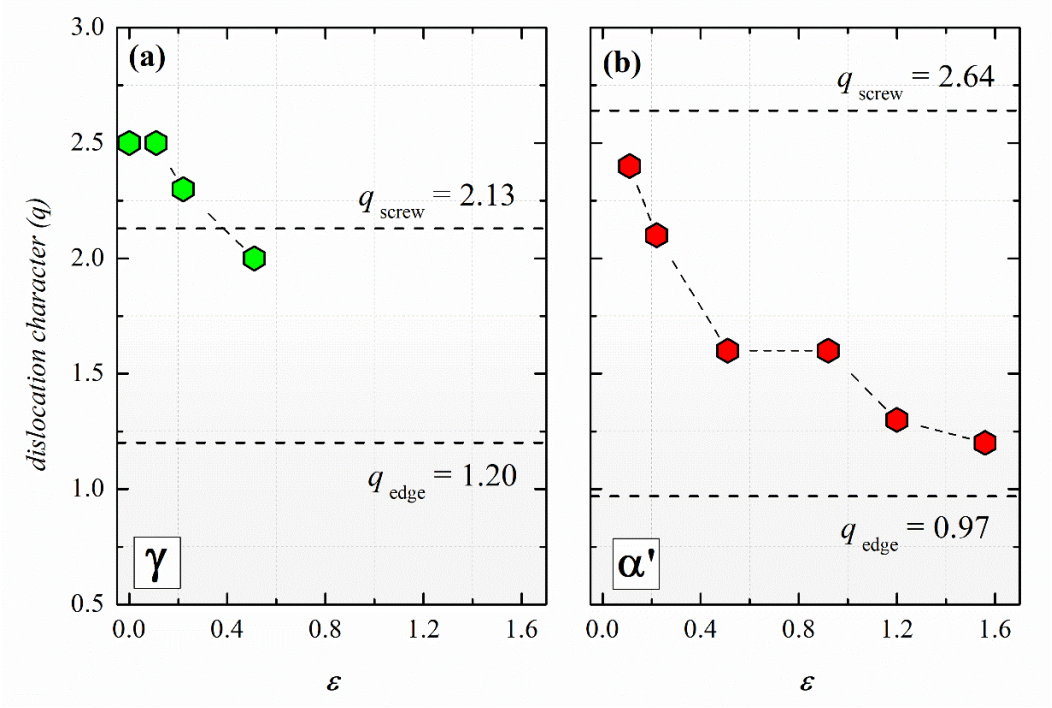

Source: elaborated by the author.

dislocations takes place in this phase during deformation. Consequently, the annihilation of screw dislocations (dynamic recovery) in α' leads to an increase in the fraction of the edge ones.

4.2.3 Microstructural characterization via EBSD

The microstructural changes of the 17.6 Mn steel during cold rolling were evaluated by means of phase maps obtained via EBSD. Figures 4.8 (a-e) display the microstructures at $\varepsilon = 0$, 0.11, 0.22, 0.51, and 1.56, respectively. The as-received steel consists of recrystallized γ-grains, partially subdivided by athermally formed ε-plates as shown in Fig. 4.8 (a). The figure shows that athermally formed α'-laths are only found within the ε-plates. Fig. 4.8 (b) shows that most of the γ-grains are fragmented by both strain-induced ε- and α'-martensite

Figure 4.8 – Microstructural evolution represented by means of phase maps obtained via EBSD. In these maps, austenite, ε- and α'-martensite are shown in green, yellow, and red, respectively. Cold-rolled samples at **(a)** $\varepsilon = 0$; **(b)** $\varepsilon = 0.11$; **(c)** $\varepsilon = 0.22$; **(d)** $\varepsilon = 0.51$; **(e)** $\varepsilon = 1.56$.

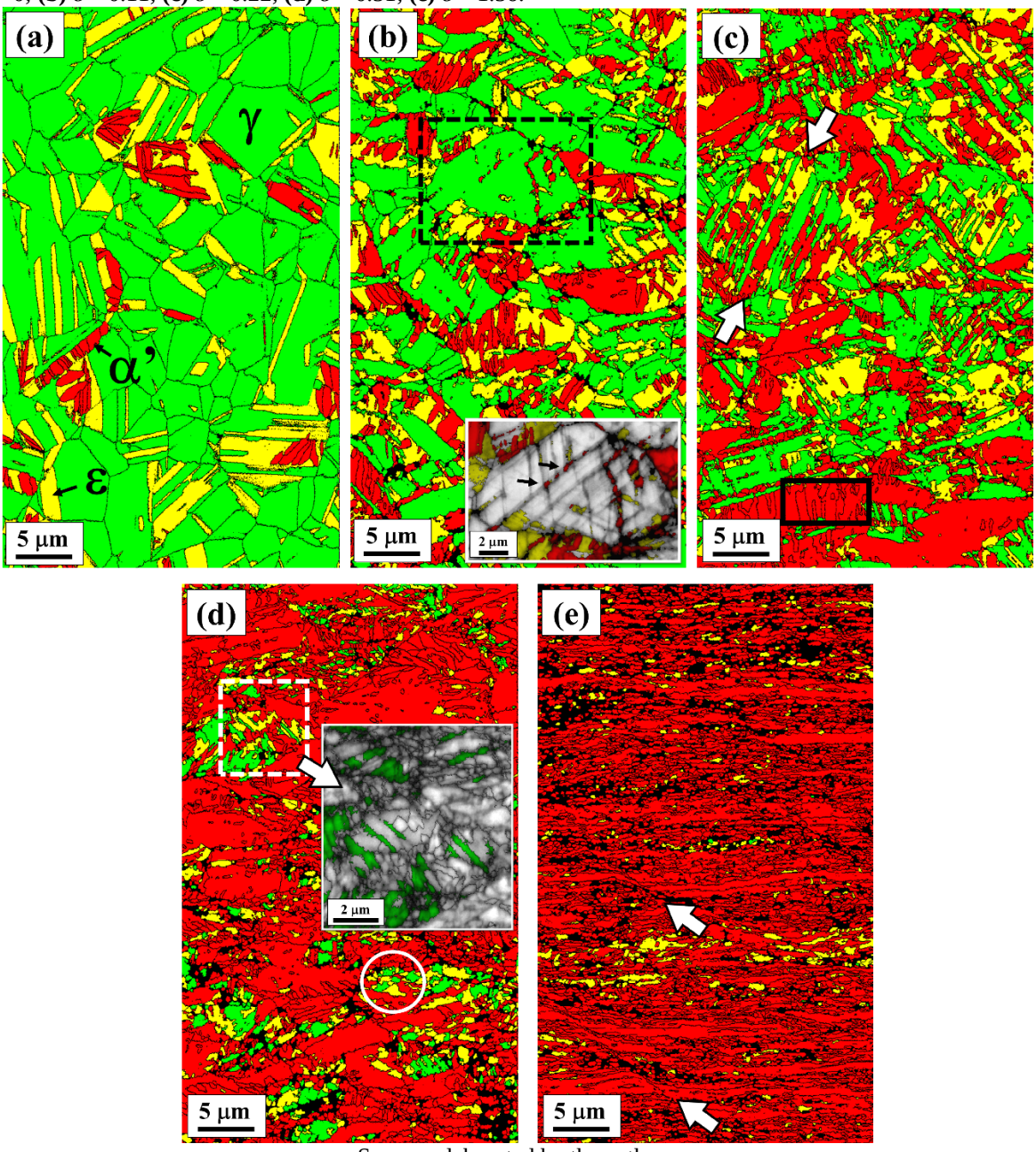

Source: elaborated by the author.

At $\varepsilon = 0.11$. Ultrafine α' is also found along thin ε-plates which were not properly indexed due to their small dimensions, but they are noticeable in the corresponding image quality map (see arrow in the inset of Fig. 4.8 b). Yet, Fig. 4.8 (b) suggests that α' is predominantly associated to ε-martensite. This observation is another evidence that the ε-phase is a precursor for α'-formation in this steel. At $\varepsilon = 0.22$ (Fig. 4.8c), α' is found within ε-plates which cross γ-grains from one grain boundary to the opposite one (see arrows). Furthermore, Fig. 4.8 (c) also provides indications that entire γ-grains have been consumed by α' (see frame).

The phase map of Fig. 4.8 (d) shows that α' is the major phase at $\varepsilon = 0.51$. At this strain level, α'-grains start to align parallel to the rolling direction (RD). The remaining γ and ε-martensite regions assume both tube-shape and ultrafine equiaxed morphologies (see inset and circle in Fig. 4.8 d). At the largest strain ($\varepsilon = 1.56$), the α'-grains are lamellar and they lie parallel to the RD (Fig. 4.8 e). In some regions, shear bands are also noticeable in Fig. 4.8 (e), as indicated by arrows. At this strain, the remaining ε-martensite is elongated and mostly parallel to the RD as well. The change in morphology of the ε-martensite indicates that it co-deforms upon cold rolling, as previous inferred by means of XRD analysis.

4.2.4 Microstructural characterization via ECCI

Submicron and nanosized defects can be imaged at a wide field of view with the aid of ECCI (GUTIERREZ-URRUTIA; ZAEFFERER; RAABE, 2009; GUTIERREZ-URRUTIA; RAABE, 2011; GUTIERREZ-URRUTIA; ZAEFFERER; RAABE, 2013), Fig. 4.9. The microstructure of the as-received steel is shown in Fig. 4.9 (a). Enlarged views of the highlighted regions in the main panel are given by the corresponding insets. Inset *"a_1"* reveals one athermal ε-plate containing α'-laths and profuse fragmentation by nanotwins. α'-laths, in turn, are composed of dislocation tangles. Inset *"a_2"* shows a γ-grain subdivided by thin ε-plates and minor arrays of SFs. Fig. 4.9 (b) shows the interior of a γ-grain which is subdivided by ε-plates into blocks at $\varepsilon = 0.11$. These γ-blocks are further fragmented by wide SFs (see arrows in Fig. 4.9b) and arrays of nanotwins.

Figure 4.9 (e) shows one γ-grain surrounded by α'-martensite at $\varepsilon = 0.22$. The austenite is fragmented by profuse nanotwins and SFs are only observed within non-twinned regions, as observed in inset *"c_1"*. Despite the fact that dislocation structures in the bulk may vary locally, Fig. 4.9 (e) displays a large area imaged via ECCI where dense dislocation

Figure 4.9 - Microstructural evolution observed with the aid of ECCI to resolve submicron structural defects such as stacking faults, mechanical twins and arrangement of dislocations. **(a)** as-received condition; cold-rolled samples at **(b)** $\varepsilon = 0.11$; **(c)** $\varepsilon = 0.22$; **(d)** $\varepsilon = 0.51$; **(e)** $\varepsilon = 1.56$.

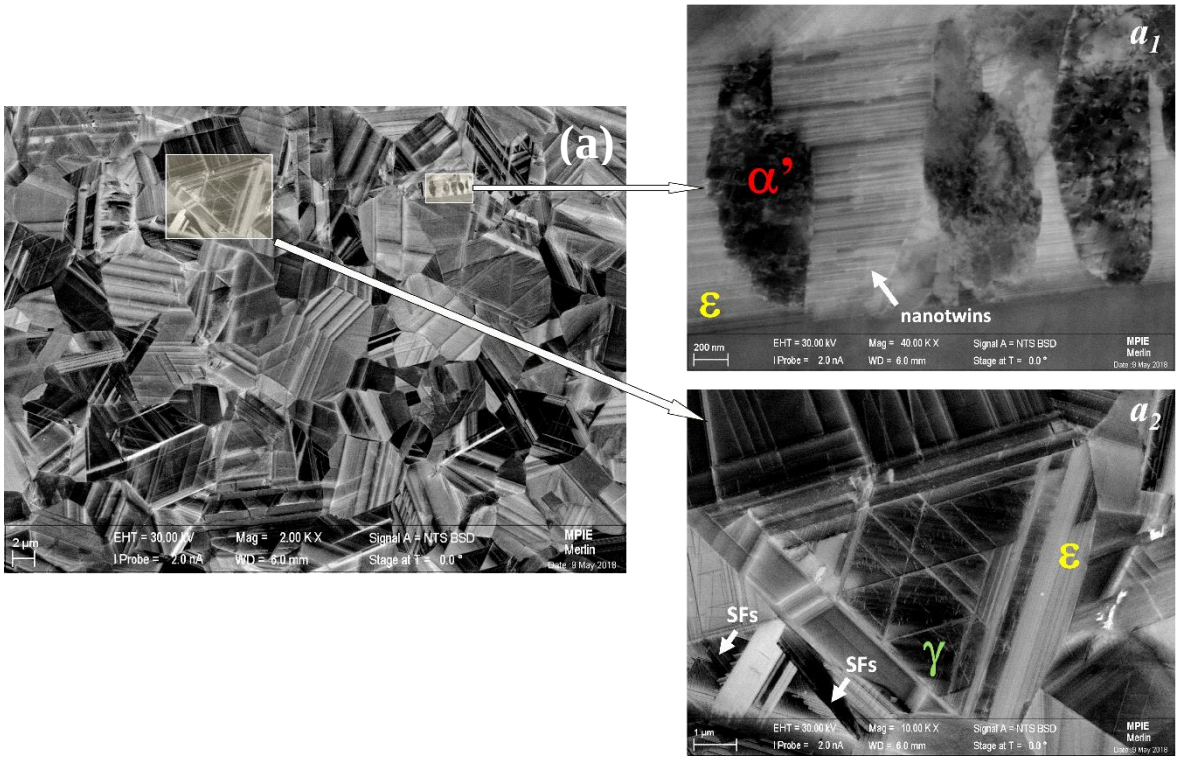

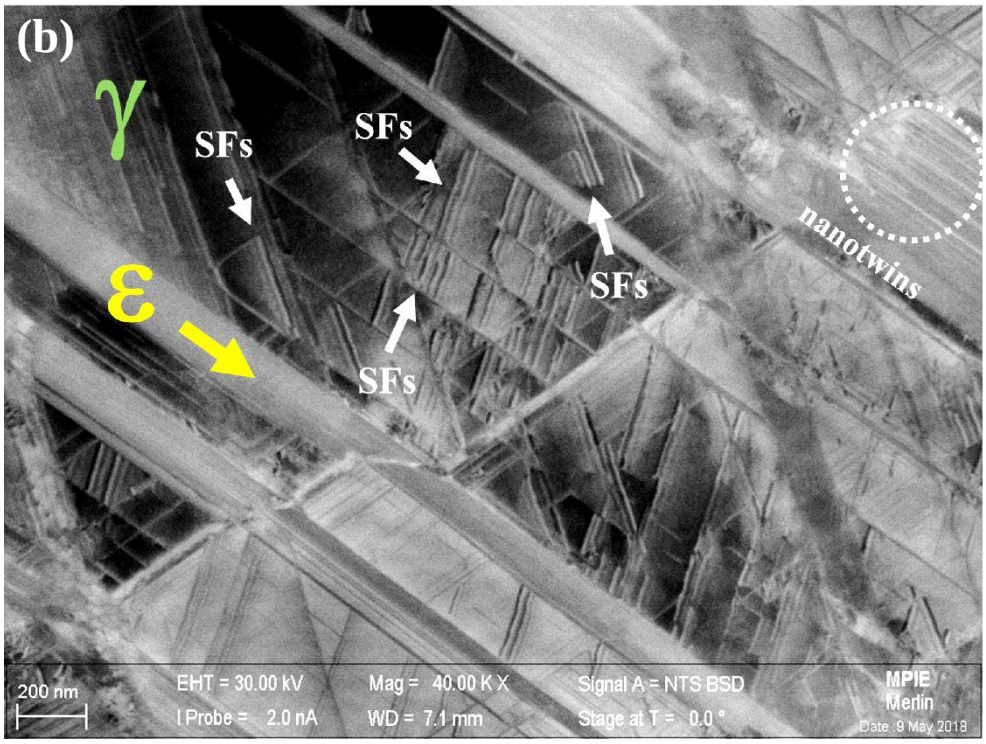

To be continued

Continuation

Figure 4.9 - Microstructural evolution observed with the aid of ECCI to resolve submicron structural defects such as stacking faults, mechanical twins and arrangement of dislocations. **(a)** as-received condition; cold-rolled samples at **(b)** $\varepsilon = 0.11$; **(c)** $\varepsilon = 0.22$; **(d)** $\varepsilon = 0.51$; **(e)** $\varepsilon = 1.56$.

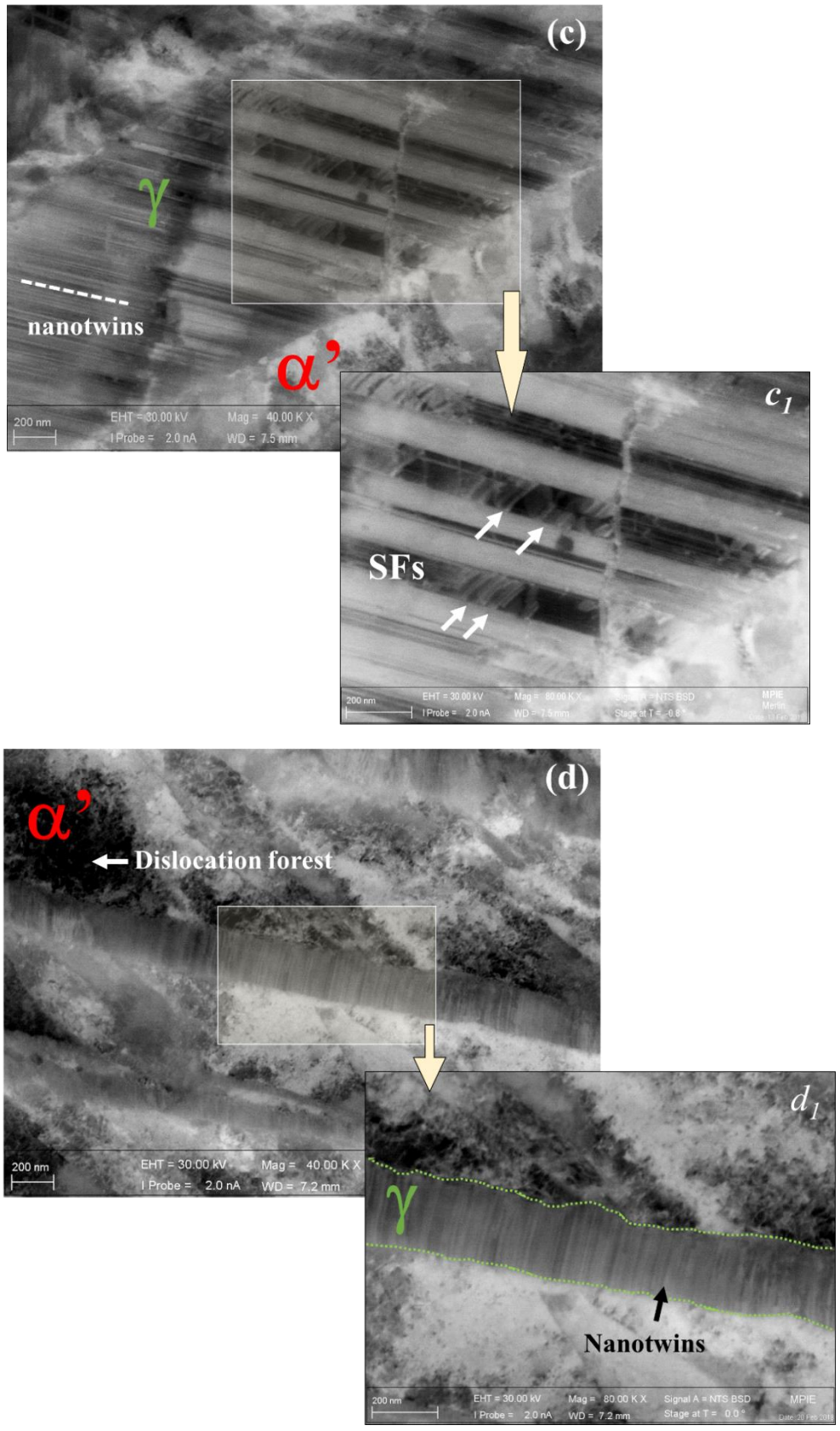

To be continued

Figure 4.9 - Microstructural evolution observed with the aid of ECCI to resolve submicron structural defects such as stacking faults, mechanical twins and arrangement of dislocations. **(a)** as-received condition; cold-rolled samples at **(b)** $\varepsilon = 0.11$; **(c)** $\varepsilon = 0.22$; **(d)** $\varepsilon = 0.51$; **(e)** $\varepsilon = 1.56$.

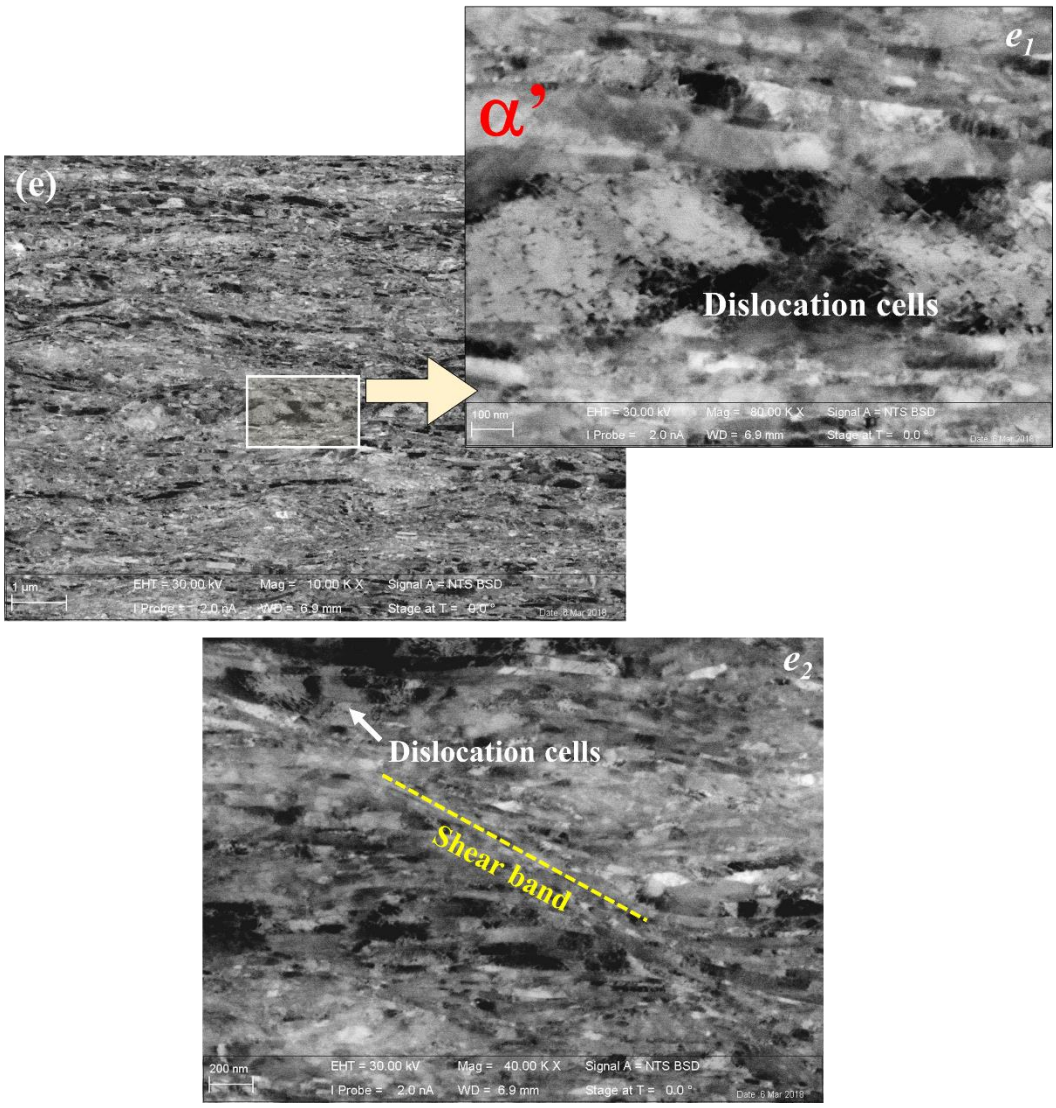

Source: elaborated by the author.

tangles can be noticed in α'-martensite. Straining to $\varepsilon = 0.51$ decreases the γ-grain size and changes its morphology into a tube-like shape, as shown in Fig. 4.9 (d) (GUTIERREZ-URRUTIA; ZAEFFERER; RAABE, 2010). At this strain level, γ is highly subdivided by nanotwins and no evidence of SFs is visible in Fig. 4.9 (d) (see inset *"d_1"*). In this figure, α'-martensite shows dislocation forests in the vicinity of the γ/α' interface. Fig. 4.9 (e) reveals that the α'-grains at $\varepsilon = 1.56$ are composed of dislocation cells (see inset *"e_1"*). Shear bands tilted 30 ± 4° relative to the RD are also noticeable, as exemplified by the dashed line in Fig. 4.9 (e_2).

4.2.5 Microhardness measurements

The strain hardening behavior of the 17.6 Mn steel is shown in Fig. 4.10. By differentiating the hardness values, it was obtained an approximate measure for the strain hardening rate as also shown in Fig. 4.10. From this figure, it is observed that the hardness of the steel increases considerably between $\varepsilon = 0.11$ and 0.22. For the same range of strain, it was noticed in Fig. 4.1 that the volume fraction of α' increases to ~ 0.40. However, the maximum strain hardening rate is observed at $\varepsilon = 0.11$ which coincides with the maximum fraction of ε-martensite (Fig. 4.1) as well as with the significant increase of planar defects in austenite. With the progress of deformation, the strain hardening rate decreases as well as the rate of α'-formation.

Figure 4.10 - Strain hardening behavior of the 17.6 wt.% Mn steel during cold rolling. The corresponding strain hardening rate was obtained by differentiating the values of hardness as a function of the logarithmic equivalent strain (ε).

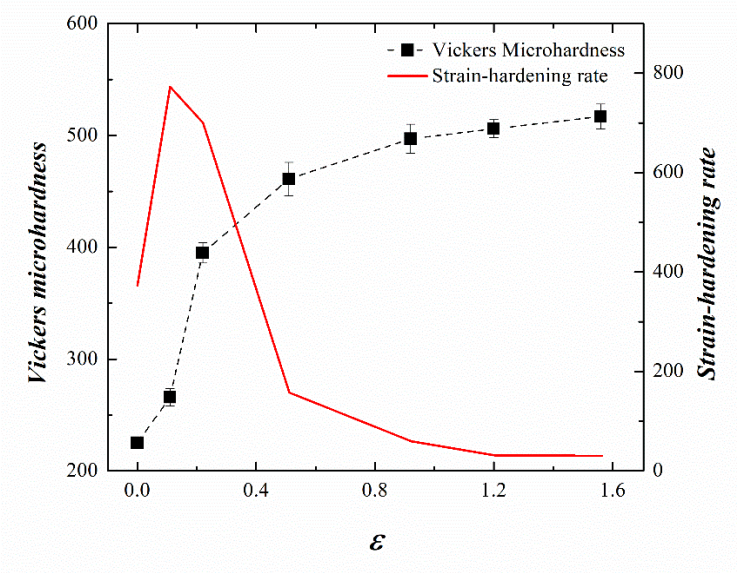

Source: elaborated by the author.

4.2.6 Microtexture

From the EBSD data, it was also assessed the microtexture evolution of the 17.6 Mn steel during cold rolling. The results are shown in Fig. 4.11 by means of orientation distribution functions (ODF), derived using the Bunge notation (BUNGE, 1982). For the austenite Fig. 4.11 (a) shows only the representative sections φ_2 = 0, 45, and 65° (HÖLSCHER; RAABE; LÜCKE, 1994). From this figure, it was noticed that austenite develops the Brass {011} <211> texture component up to $\varepsilon = 0.92$. The microtexture of α'-martensite is represented in Fig. 4.11 (b) by means of the representative φ_2 = 0 and 45°

Figure 4.11 - Microtexture evolution of the 17.6 wt.% Mn steel during cold rolling represented by means of orientation distribution functions (ODFs). Representative sections φ_2 = 0, 45, and 65° are shown for austenite in **(a)**; For α'-martensite the representative sections φ_2 = 0, 45° are given in **(b)**; For ε-martensite, the representative sections φ_2 = 0, 30° are shown in (c).

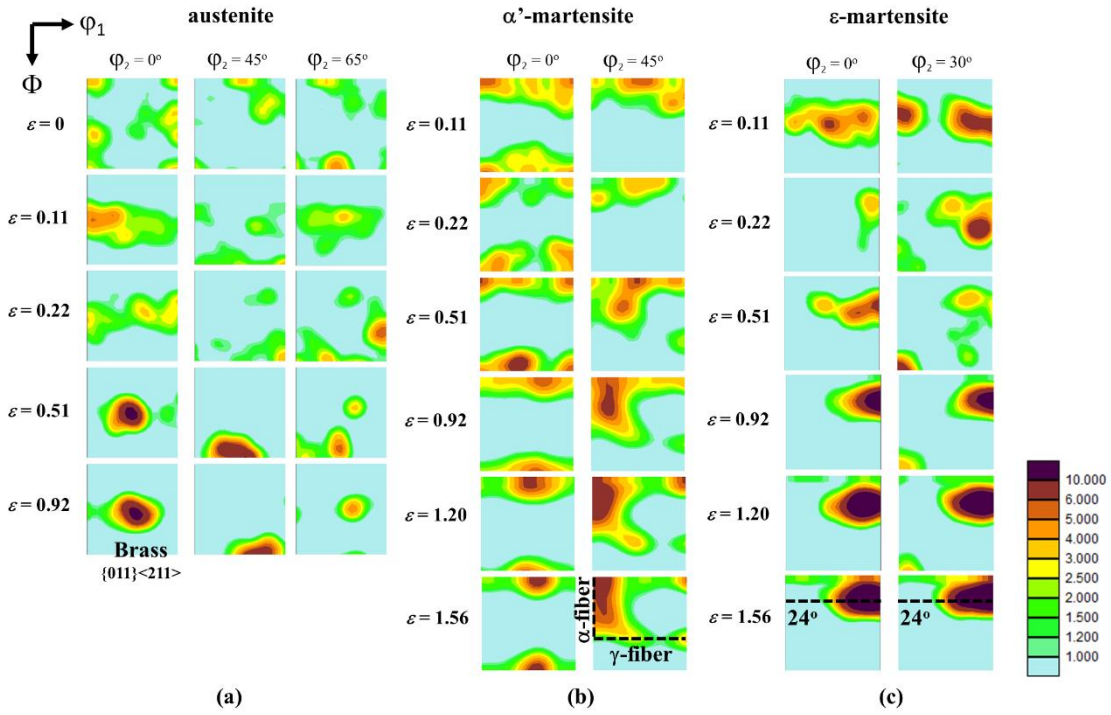

Source: elaborated by the author.

sections. In this figure, it is clearly seen the formation and strengthening of α- and γ-fibers from ε = 0.92 on. For the ε-martensite the sections φ_2 = 0, 30° in Fig. 4.11 (c) show that this phase develops a {hkil} fiber-type texture deviating ~ 24° from the ideal basal fiber located at Φ = 0°. In other words, over the course of rolling the basal planes of ε-martensite tilts ~ 24° from the normal direction (ND) of the plate towards the RD. Deformations larger than ε = 0.92 further strengthen this texture component.

4.3 Discussion

4.3.1 Stacking fault energy

The stability of austenite in high-Mn steels is commonly linked to the SFE. In the present steel, a SFE of ~ 8.1 mJ/m^2 was calculated by means of thermodynamic modelling as reported elsewhere (SOUZA FILHO et al., 2019a). According to this low SFE value, the results presented in Section 4.2 show that strain-induced α'-martensite formation is the predominant mechanism to accommodate deformation at large strains, viz. $\varepsilon \geq 0.51$ (BALDO; MÉSZÁROS, 2010). However, in the present work it is also highlighted the importance of the co-deformation of the remaining γ and ε-phase regions on the overall bulk

strain hardening behavior, especially at low strains. The next sections will discuss the strain hardening mechanisms of all phases, in particular austenite.

4.3.2 Strain hardening of the austenite

The microstructural evolution of austenite during cold rolling is schematically summarized in Fig. 4.12. The microstructural changes in this phase are given by its subdivision into ever-smaller units varying from blocks ($\varepsilon = 0.11$) to small tube-like shaped grains at $\varepsilon = 0.51$. At the submicron perspective, fragmentation is observed to occur by the formation of planar defects. At low cold rolling strains ($\varepsilon = 0.11$), γ-blocks are composed of pronounced amounts of wide SFs and arrays of nanotwins, as calculated by means of the Warren's theory (Fig. 4.4) and confirmed by inspection of ECCI micrographs (Fig. 4.9). The high density of SFs created and retained within γ-blocks hints that not all SFs were consumed to form ε-phase or twins (PRAMANIK et al., 2018b; SAHU et al., 2012). At $\varepsilon = 0.22$, the calculated probability of SFs (P_α) within austenite increases about one order of magnitude (~ 0.01) and becomes similar to the probability of twinning (P_β). As revealed by ECCI, such SFs are confined within non-twinned regions and are hence much narrower than those SFs observed at the previous strain level. SFs are preferential sites for ε-martensite nucleation (IDRISSI et al., 2009). In the present case, the ε-martensite fraction has been experienced a reduction since $\varepsilon = 0.11$. Therefore, the increasing SFs probability at $\varepsilon = 0.22$ suggests that the newly formed SFs are not consumed by the SFs $\rightarrow$ ε transformation, as well. In light of these observations, it is possible to conclude that both mechanical twinning and formation of further SFs are the main mechanisms of strain accommodation in remaining the γ regions at low rolling strains. Further straining to $\varepsilon = 0.51$, on the one hand, decreases the stacking fault probability of the remaining tube-shaped γ-grains to ~ 3×10^{-4}. On the other hand, such a strain slightly increases the probability of twinning to ~ 9×10^{-3}. These opposite trends suggest that the occurrence of twinning is more likely than faulting in austenite, at least at large deformations. At this point, it has also to be considered that a substantial reduction of P_α is a likely consequence of SF consumption by the further formation of nanotwins (PRAMANIK et al., 2018b). In other words, one can say that the overlapping of fresh formed SFs leads to the formation of nanotwins (GALINDO-NAVA; RIVERA-DÍAZ-DEL-CASTILLO, 2017). Idrissi et al. (2009) reported that intrinsic SFs are precursors for mechanical twinning in an alloy with similar chemical composition to the present steel, viz. Fe-19.7Mn-3.1Al-2.9Si (wt.%). The results obtained via Warren's theory (P_α and P_β) for

Figure 4.12 - Schematic representation of the microstructural evolution of the austenite during cold rolling in terms of morphology and submicron planar defects.

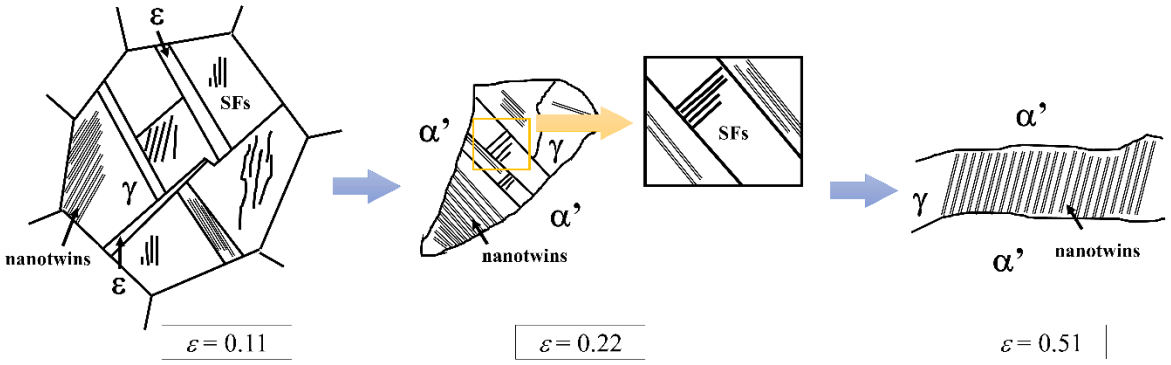

Source: elaborated by the author.

ε = 0.51 are confirmed by the ECCI observations where it was noticed the absence of SFs and the presence of profuse nanotwins within the γ tube-like shaped grains. Therefore, it is plausible to assume that twinning is the main strain hardening mechanism of austenite at large strains.

Twinning is responsible for subdividing the coherent domains (crystallite) into smaller units, as mentioned in Section 2.4.1.2. The influence of twinning on the effective crystallite size of austenite (D_{eff}^{γ}) is given in Fig. 4.13 (a). A linear relationship is observed between P_β and the inverse of the effective crystallite size $(D_{eff}^{\gamma})^{-1}$. In other words, the fragmentation of the coherent domains by twinning occurs under a constant rate of $\frac{d(D_\gamma^{-1})}{d(P_\beta)}$ ~ 0.55. By taking the inverse of the intercept (D_0), the size of a non-twinned crystallite is obtained as being 417 nm, which is the coherent domain size of austenite in the as-received condition (see also Fig. 4.3a).

Deformation nanotwins also act as obstacles for dislocation slip by diminishing the mean free path (Λ) for their movement (DE COOMAN; CHIN; KIM, 2011). Once Λ is progressively lower, the interaction of new dislocations become prominent which contributes to the strengthening of remaining γ. For the present case, the evolution of ρ_γ can be associated to the probability of twinning (P_β) as depicted in Fig. 4.13 (b). In this figure, it is noticed that ρ_γ increases with a linear dependence of P_β. Assuming that twinning is the major contributor to the increase of ρ_γ, one can say that dislocation density evolves under a constant rate of $\frac{d(\rho_\gamma)}{d(P_\beta)}$ ~ 1 *x* 10^{17} m^{-2} as the density of nanotwins increases.

Figure 4.13 - (a) Linear relationship between the inverse of the coherent domain size of austenite (D_{γ}^{-1}) and the probability of twinning (P_{β}); **(b)** Linear relationship between dislocation density of austenite (ρ_{γ}) and the corresponding probability of twinning (P_{β}).

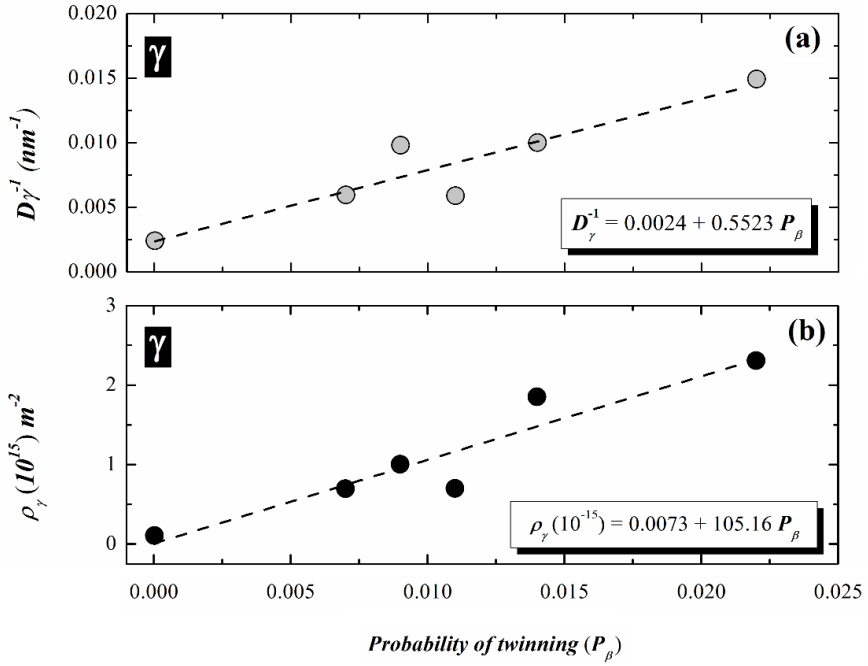

Source: elaborated by the author.

Results from Fig. 4.13 (b) and Section 4.2.2.4 show that ρ_{γ} does not saturate during rolling. Also, the dislocation density in austenite for strains $\varepsilon \geq 0.51$ increases with a higher rate when compared to α'-martensite, as shown in Fig. 4.5. This observation suggests that austenite is softer than α'-martensite and, therefore, it is more readily deformed (SHINTANI; MURATA, 2011). The ever-increasing values of ρ_{γ} in Fig. 4.5 also indicate the absence of substantial dynamic recovery in austenite. In this context, dynamic recovery would be mainly achieved through the annihilation of screw dislocations by cross-slip. Since the SFE of the present steel is very low (~ 8.1 mJ/m^2), cross-slip in γ is expected to be rather difficult. This observation is confirmed by Fig. 4.7 (a) where it is observed that dislocations in γ remain mostly of screw-type during deformation.

4.3.3 Strain hardening of the ε-martensite

Athermal ε-martensite in the as-received condition is considerably more faulted than the starting austenite, as observed via both Warren's treatment and ECCI analysis. It was discussed before that the prior presence of ε-martensite likely acts as precursor for α'-formation, i.e. γ → ε → α'. In fact, the maximum amount of ε-martensite was observed at ε = 0.11 which coincides with the maximum strain hardening rate (see Fig. 4.10). At this strain,

dislocations are mainly stored within the ε-phase (Fig. 4.5). Larger strains lead to ε-consumption and an increase in its microstrain (Fig. 4.3). These results suggest that the ε-martensite is rather soft and co-deforms with austenite before the $\varepsilon \rightarrow \alpha'$ reaction (PRAMANIK et al., 2018b). These observations are supported by the high probabilities of SFs and twins presented in Fig. 4.4 (b). Therefore, it can be concluded that these mechanisms are found to operate similarly for achieving strain accommodation in this phase.

4.3.3.1 Local strain partitioning induced by ε-formation at ε = 0.11

To evaluate the contribution of ε-formation to the strain hardening behavior at low rolling strains, additional EBSD analyses were conducted for the material deformed to ε = 0.11. Fig. 4.14 (a) reproduces a portion of the EBSD map previously displayed in Fig. 4.8 (b). The corresponding kernel average misorientation (KAM) and the inverse pole figure (IPF) maps are depicted in Figs. 4.14 (b) and (c), respectively. The arrows in Fig. 4.14 (a) clearly show that the ε-plates are responsible for subdividing austenite into smaller γ-blocks with lengths of ~ 1.5 μm (as already discussed in Section 4.3.2). By using the KAM approach for austenite, Fig. 4.14 (b) reveals that local misorientation gradients (lattice distortion) accumulate at the γ/ε interfaces as clearly evidenced by the inset "b_1". This result is a strong evidence that the ε-formation at ε = 0.11 promotes local strain partitioning between the adjacent ε- and γ- phases. Reversely, the interior of the γ-blocks seems to maintain its orientation, as suggested by both Figs. 4.14 (b) and (c).

Aiming at determining the magnitude of the misorientation gradients near the γ/ε interfaces, three misorientation profiles were collected along the arrows 1, 2, and 3 depicted in Fig 4.14 (c). The obtained results are shown in Fig. 4.14 (d) in terms of the "*point-to-point*" and "*point-to-origin*" misorientation profiles. Since the ε-plates at this strain are only a few nanometers thick (see Section 4.2.4), their corresponding orientation data were not properly acquired in Fig. 4.14 (d). Nevertheless, with the aid of the "*point-to-point*" profiles, the positions of the ε-phase can be sufficiently estimated in Fig. 4.14 (d). The "*point-to-origin*" profiles reveal that the accumulation of misorientation within each evaluated γ-block (related to its interior) reaches up to ~ 5° near the γ/ε interface. Additionally, Fig. 4.14 (d) also confirms that the γ-blocks maintain a near constant orientation far from the interface.

According to Wu et al. (2016) and several other authors (TASAN et al., 2014a; TASAN et al., 2014b), strain partitioning across phase interfaces is a consequence of the different flow stresses in adjacent phases. Moreover, strain gradients are accommodated by

Figure 4.14 - EBSD map of the 17.6 wt.% Mn steel cold rolled at $\varepsilon = 0.11$. **(a)** phase map overlapped to its corresponding image quality. In this map, austenite, ε- and α'-martensite are represented by gray, yellow, and red, respectively; **(b)** kernel average misorientation (KAM) map, constructed by considering the third neighbors; **(c)** inverse pole figure (IPF) map; **(d)** misorientation profiles obtained from arrows 1, 2, and 3 depicted in (c).

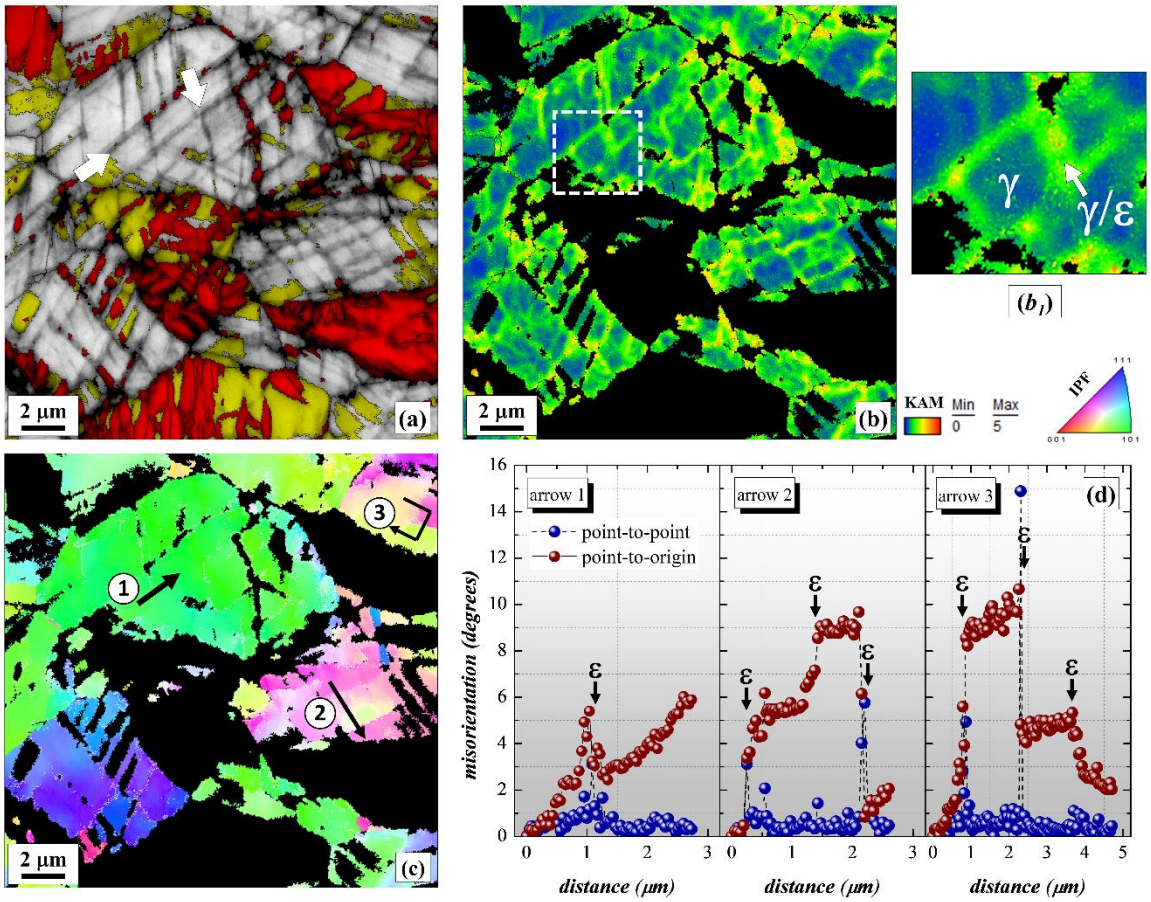

Source: elaborated by the author.

accumulation of geometrically necessary dislocations (GND), which are responsible for locally increasing the strain hardening of the material (CALCAGNOTTO et al., 2010). For the present case, a detailed ECCI inspection was also performed near one γ/ε interface for the steel deformed at $\varepsilon = 0.11$, as shown in Fig. 4.15. An enlarged view of Fig. 4.15 (a) is given in Fig. 4.15 (b) and a schematic representation in Fig. 4.15 (c). This enlarged view shows several GNDs piled up at a γ/ε interface. Such observation agrees with the statement from refs. (CALCAGNOTTO et al., 2010; WU et al., 2016) and corroborates our analysis of local strain accumulation. These observations also suggest that strain hardening at the early stages of cold rolling has an important contribution from local strain partitioning induced by ε-formation. Furthermore, one must bear in mind that the martensitic transformation can be triggered by the presence

Figure 4.15 - (a) Microstructure of the 17.6 wt.% Mn steel cold rolled at $\varepsilon = 0.11$, observed with the aid of ECCI; **(b)** enlarged view of the dashed frame in (a); **(c)** corresponding schematic representation.

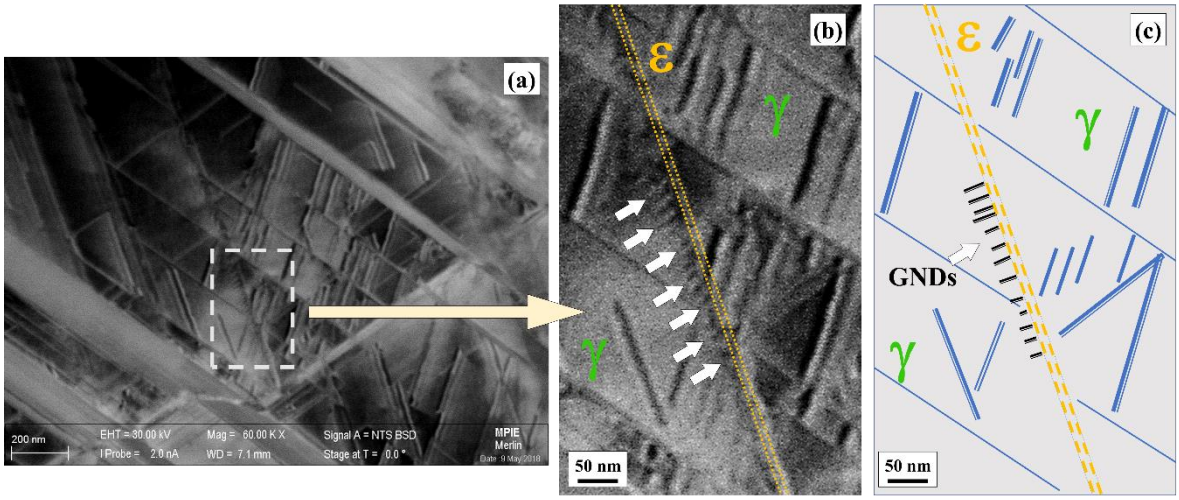

Source: elaborated by the author.

of local strain or stress gradients (WU et al., 2016). Therefore, with the progress of rolling it is plausible to expect that further formation of martensite may likely occur towards the γ-regions displaying misorientation gradients as those shown in Fig. 4.14.

4.3.4 Strain hardening of the α'-martensite

Strain-induced α'-martensite forms at $\varepsilon = 0.11$ with a lath-type morphology and it is primarily associated to ε-plates. At $\varepsilon = 0.22$, the volume fraction of α'-martensite is close to the austenite one, but dislocations are preferably stored in α' (1.7×10^{15} m^{-2}) (see Fig. 4.5). It was also found that the highest increase in hardness occurs at this strain (see Fig. 4.10). Therefore, the progress of the ε → α' reaction in conjunction with the preferable accumulation of dislocations in α' suggests that α'-formation starts to play a more prominent role on the strain hardening of this steel.

From $\varepsilon = 0.51$ on, formation of strain-induced α'-martensite is a main mechanism for strain accommodation. Since the dislocation density in α' saturates at $\varepsilon = 0.51$ (3×10^{15} m^{-2}), it can be inferred that large deformations are accommodated by the rearrangement of dislocation tangles into cells as revealed by large areas imaged via ECCI (Fig. 4.9). In fact, a fairly constant dislocation density in α'-martensite upon cold rolling was also reported by Shintani and Murata (2011) for an AISI 304 steel. Differently from austenite, the saturation of $\rho_{\alpha'}$ with deformation (Fig. 4.5) can be ascribed to dynamic recovery as previously evidenced in Fig. 4.7 (b). From this figure, it is observed that dislocations in the α'-phase

changes from screw- to edge-type during cold rolling. This observation indicates pronounced cross-slip which promotes annihilation of screw-dislocations by dynamic recovery, so that the total dislocation density in this phase remains nearly unchanged during rolling. Another important information from Fig. 4.7 (b) is the evidence of cross-slip between $\varepsilon = 1.2$ and 1.56, when the $\varepsilon \rightarrow \alpha'$ transformation seems to be ceased (Fig. 4.1 and 4.8e). At $\varepsilon = 1.2$, it is plausible to expect that α'-martensite contains dislocations inherited by the ε-phase (due to the displacive $\varepsilon \rightarrow \alpha'$ reaction) and those generated by the martensitic transformation itself. Therefore, the occurrence of cross-slip in the deformation range between $\varepsilon = 1.2$ and 1.56 provides evidence that both types of dislocations are mobile in α'. Finally, at the largest strain ($\varepsilon = 1.56$), shear banding occurs in α'-martensite as well.

4.3.5 Microtextural evolution

Fig. 4.11 (a) shows that austenite develops the Brass {011} <211> texture component up to a rolling reduction of $\varepsilon = 0.92$. The strengthening of this texture component even at large strains confirms the absence of dislocation cross-slip as the primary deformation mechanism in austenite (HÖLSCHER; RAABE; LÜCKE, 1994). Mechanical twinning is well accepted to play an important role for the development of the Brass-type component in low-SFE steels, allowing normal slip in twinned regions (VAN HOUTE, 1978; DONADILLE et al., 1989; RAABE, 1997). Previously, it was noticed that the pronounced activity of mechanical twins was an essential deformation mechanism in the remaining austenite. Therefore, it is plausible to infer that mechanical twinning in austenite is responsible for development of the Brass texture.

α'-martensite develops the typical texture components of bcc ferrite during cold rolling (HÖLSCHER; RAABE; LÜCKE, 1991). From Fig. 4.11 (b) an important observation is the presence of the rotated cube ($\varphi1 = 0°$, $\Phi = 0°$, $\varphi = 45°$) pertaining to the α-fiber. α'-grains with such orientation are derived from Brass-oriented austenite holding the Kurdjmov-Sachs (KS) orientation relationship but they also form through regular dislocation slip during cold rolling (KUMAR et al., 2004; RAABE; LÜCKE, 1993; KUNDU; BHADESHIA, 2007). Indeed, literature shows that the development of α'-textures depends very much on the γ-parent texture, independently on the intermediary presence of the ε-phase, viz. $\gamma \rightarrow \varepsilon \rightarrow \alpha'$ (KUNDU; BHADESHIA, 2007). For the present

case, the reported results are similar to those reported in ref. (GAZDER et al., 2015) for a 17 wt.% Mn steel.

The development of textures in hcp metals is related to their c/a ratio (WUANG; HUANG, 2003). From Table 4.1, it can be noticed that the c/a ratio for ε-martensite during cold rolling is higher than the ideal one (1.633). In this case, the basal planes of ε-martensite are generally expected to be tilted ~ 25° from the ND towards the RD, in accordance with the results observed in Fig. 4.11 (c). According to ref. (GAZDER et al., 2015), the development of such texture is also due to the combination of both basal slip and twinning. For the present case, this observation is in good agreement with the fact that mechanical twinning is an essential deformation mechanism in ε-martensite, as observed in Fig. 4.4 (b).

4.4 Summary and conclusions

The strain hardening mechanisms of austenite (γ), ε- and α'-martensite were followed during cold rolling of a 17.6 wt.% Mn steel. By combining high-resolution SEM with XRD data, the hierarchical formation of submicron defects is proposed. Based on the experimental results, the following conclusions are drawn:

i) Austenite changes its morphology from blocks (at ε = 0.11) into tube-like shaped grains at ε = 0.51. At low strains, γ-blocks are subdivided by ε-plates, wide stacking faults (SFs), and mechanical twins. SFs are consumed for further formation of mechanical twins at ε = 0.51, suggesting that austenite accommodates large strains by twinning together with dislocation flow and multiplication. The ever-increasing dislocation density in austenite (ρ_γ) is due to the absence of cross-slip during deformation.

ii) The maximum amount of ε-martensite was observed at ε = 0.11, which coincides with the largest strain hardening rate. At this strain level, ε-formation induces misorientation (strain) gradients within austenite near the γ/ε interfaces, which are accommodated by GNDs. ε-martensite co-deforms with austenite by creating SFs and mechanical twinning.

iii) From ε = 0.51 on, α'-formation is the main strain hardening mechanism. Larger deformations are accommodated in α'-martensite by the rearrangement of dislocation tangles into cells. The dislocation density in α'-martensite saturates from ε = 0.51 on as a result of dynamic recovery. Shear banding is also noticed at ε = 1.56.

iv) Austenite develops the Brass-type texture component, which was associated to mechanical twinning. ε-martensite presented its basal planes tilted ~ 24° from the normal direction of the plate towards the rolling direction. α'-martensite develops and strengthens the α- and γ- fibers during rolling.

Chapter 5

Martensite to austenite reversion: partitioning-dependent two-stage kinetics revealed by atom probe tomography, in-situ magnetic measurements and simulation

5.1 Introduction

Advanced Mn-based steel variants have been designed by means of precipitation reactions, grain refinement (ZHANG; RAABE; TASAN, 2017), and grain boundary segregation engineering (RAABE et al., 2013). The absence of pronounced anisotropy in both mechanical properties and crystallographic textures are among the advantages of strengthening by grain refinement (ESCOBAR; DAFÉ; SANTOS, 2015). This can be achieved by austenite reversion ($\alpha' \rightarrow \gamma$) treatments, as reported for austenitic high-Mn TRIP steels (ESCOBAR et al., 2015; DASTUR et al., 2017). In this scenario, Mn diffusion plays a key role since it exhibits very low diffusivity in austenite with a diffusion constant of D_γ = 5.89 x 10^{-24} m^2s^{-1} (DMITRIEVA et al., 2011). The high Mn diffusivity in α'-martensite ($D_{\alpha'}$ = 7.56 x 10^{-21} m^2s^{-1}), however, creates a Mn flux into the growing austenite. As a result, strong partitioning and segregation effect can occur at α'/γ interfaces and grain boundaries (DMITRIEVA et al., 2011).

The complex interplay of elemental redistribution and the associated thermodynamics and kinetics of the reversion from α' into γ on the one hand (NAKADA et al., 2012; NAKADA et al., 2013; NAKADA et al., 2014) and the importance of this transformation for a variety of steels on the other hand (WANG et al., 2014; WANG et al., 2015; KUZMINA et al., 2015; KOYAMA et al., 2017) have thus served as motivation for the present study. In order to observe these phenomena in a well-controlled manner and at the same enable tracking the reversion by a variety of probes including magnetism, dilatometry, microstructure, and atom probe tomography slow continuous annealing treatments were conducted. In this case the development and influence of elemental partitioning can be well studied during γ-reversion, particularly in Fe-Mn alloys owing to the high difference in Mn diffusion between the two phases (MOSZNER et al., 2014). At slow heating rates, long-range diffusional processes favor matrix partitioning into solute-rich (e.g. Mn) and solute-depleted zones. In this case, Mn-enriched and depleted regions are observed to be reversed austenite and remaining α', respectively. Due to lower amounts of

solute in the remaining α', its transformation to austenite is delayed to higher temperatures. Therefore, a splitting of the γ-reversion into two stages is clearly observed under such annealing conditions.

γ-reversion during slow continuous annealing has been reported to proceed in different kinetic steps in maraging steels (KAPOOR; KUMAR; BATRA, 2003; KAPOOR; BATRA, 2004), binary and ternary alloys such as Fe-Mn/Fe-Mn-Pd (MOSZNER et al., 2014). In all these studies, however, the initial martensitic microstructures from which the γ-reversion proceeds were of lath-type, obtained by quenching. Here, austenite reversion is evaluated for strain-induced martensite in a 17.6Mn-TRIP steel. For this purpose, the steel was cold rolled up to 80% of thickness reduction ($\varepsilon = 1.56$). Slow annealing treatments were conducted using both continuous dilatometry and *in-situ* magnetic probing up to 800°C. Further interrupted dilatometry was also performed at intermediate stages of γ-reversion. The microstructure was characterized by high-resolution electron backscatter diffraction (EBSD). Chemical gradients between austenite and martensite for representative samples were investigated by atom probe tomography (APT) (RAABE et al., 2013; DMITRIEVA et al., 2011; KUZMINA; PONGE; RAABE, 2015; KWIATKOWSKI DA SILVA et al., 2017; KWIATKOWSKI DA SILVA et al., 2018a). The experimental data were compared with thermo-kinetic and thermodynamic simulations, using DICTRA and Thermo-Calc, respectively. The growth of austenite during isothermal annealing was also evaluated by combining thermo-kinetic simulations with APT results. In a recent work, Dastur et al. (2018) evaluated the Mn partitioning in an 18 wt.% Mn steel by tracking changes of the Curie temperature (T_{Curie}) of α'-martensite. Here the elemental partitioning observed by APT and predicted by simulation was used to calculate T_{Curie} of the 17.6Mn-TRIP steel. The results were comparable to the T_{Curie} values observed experimentally by means of *in-situ* magnetic measurements. These results show that the ferromagnetic behavior of the α'-martensite is linked to its elemental partitioning (viz. Mn, Al, and Si) which takes place during austenite reversion.

5.2 Results

5.2.1. Dilatometry experiments

Starting from the 80% cold-rolled state (Fig. 4.8e), the stability of the α'-martensite was evaluated during slow continuous annealing. The relative changes in length $\frac{\Delta L}{L_0}$ of the cold-rolled material as a function of temperature are shown in Fig. 5.1 (a). The corresponding

Figure 5.1 - Dilatometry measurements for the 80% cold-rolled steel. For this measurement the specimen was annealed from room temperature up to 800°C with a heating rate of 0.05 °C/s. In this figure, L_o is the initial length of the specimen, taken parallel to the RD of the 80% cold-rolled plate. **(a)** Relative changes in length ($\Delta L/L_o$) of the specimen. **(b)** Corresponding derivative curve $d(\Delta L/L_o)/dT$ for the heating process.

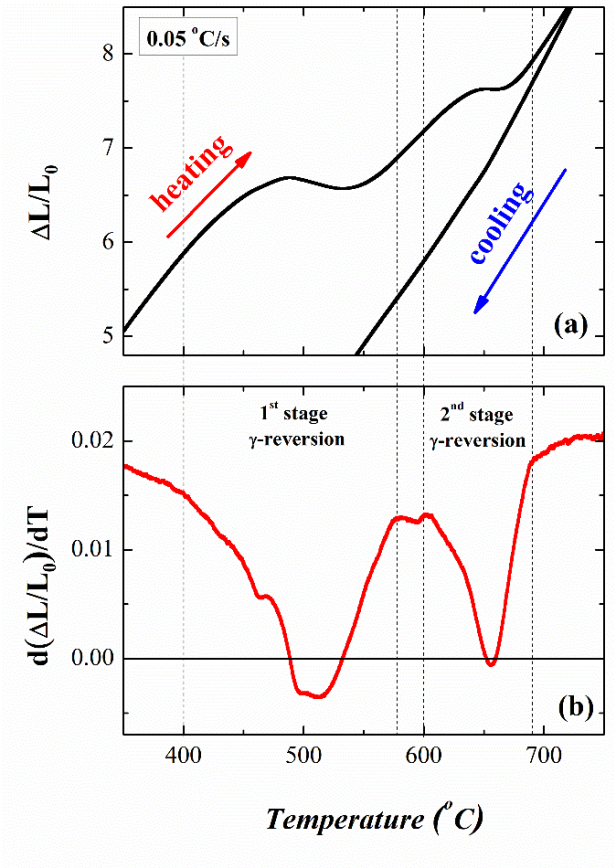

Source: elaborated by the author.

derivative curve over the course of the heating process is depicted in Fig 5.1 (b). Fig. 5.1 (a) reveals two contraction events, indicating that the α' → γ transformation splits into two distinct stages (GARCÍA DE ANDRÉS et al., 2002; LÜ et al., 2010). Consequently, two negative peaks are observed in the derivative $\frac{d\left(\frac{\Delta L}{L_0}\right)}{dT}$, viz. at 505 and 660°C (Fig. 5.1 b). For both stages of the γ-reversion, the starting (A_s) and finishing (A_f) temperatures were determined as those values where $\frac{\Delta L}{L_0}$ deviates from linearity. Therefore, the first stage of γ-reversion starts and finishes at ~ 390 ($A_s^{1st\text{-}stage}$) and ~ 575°C ($A_f^{1st\text{-}stage}$), respectively. By using the same approach for the second stage of γ-reversion, $A_s^{2nd\text{-}stage}$ and $A_f^{2nd\text{-}stage}$ are, respectively, ~ 600 and ~ 685°C. Fig. 5.1 shows that the first stage of γ-reversion extends over a broader temperature range when compared to the second one. Additionally, the observed magnitude of contraction is smaller for the second stage. Similar results were reported by Mozsner et al. (2014) for binary Fe-Mn alloys containing 5 and 10 wt.% Mn.

5.2.2 In-situ magnetic measurements

The magnetization (M) of the material during heating (red curve) and cooling (blue curve) is reported in Fig. 5.2 (a). The corresponding derivative $\frac{dM}{dT}$ during the heating stage is displayed in Fig 5.2 (b). Fig 5.2 (a) reveals that the magnetization of the material starts to decrease at ~ 375ºC. From this temperature on, the ever-decreasing values of M reach a maximum rate at 505°C, as clearly evidenced by the first peak (at 505°C) in the $\frac{dM}{dT}$ curve (Fig. 5.2b). Such loss in magnetization with temperature can be firstly attributed to relaxation of the magneto-crystalline constants (CULLITY; GRAHAM, 2009). However, the main reason for such behavior is the reduction in volume fraction of the ferromagnetic phase (α'-martensite), i.e. the progressing γ-reversion. Besides, these results agree well with measurements (Fig. 5.1 b). As shown in Fig. 5.2 (a), the magnetization continuously decreases for higher temperatures until it sharply drops to values lower than 1 emu/g at 625ºC, evidencing that the Curie temperature of the remaining α'-martensite has been

Figure 5.2 - (a) *In-situ* magnetic measurements (heating) conducted from room temperature up to 800°C with a rate of 0.05°C/s, in the presence of an external magnetic field of 90 Oe (red curve). The cooling process was performed using a rate of - 0.05°C/s with the same external magnetic field (blue curve). **(b)** Corresponding derivate curve (dM/dT) for the heating process.

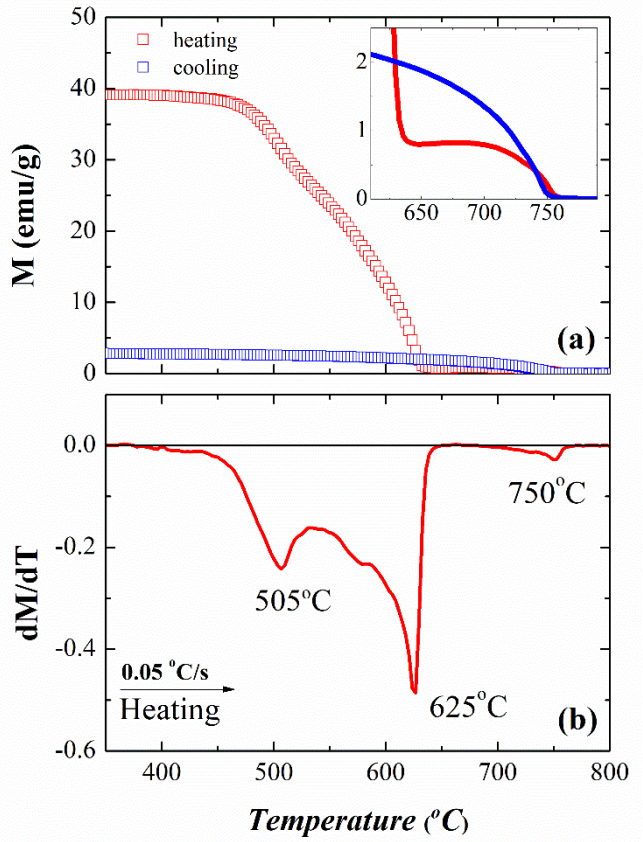

Source: elaborated by the author.

Figure 5.3 - Metallographic inspection of the 80% cold-rolled steel after being submitted to the *in-situ* magnetic measurements. EBSD maps were conducted in the central region of the sample **(a)**, as well as near its surface **(b)**.

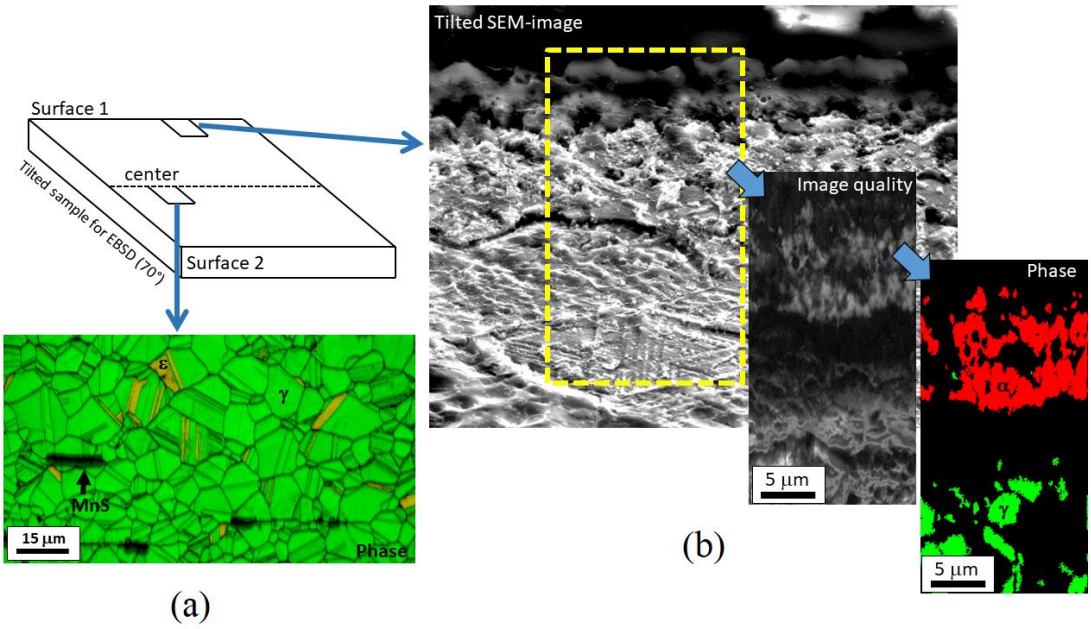

Source: elaborated by the author.

reached. A careful inspection of Fig 5.2 (a), however, reveals that a completely paramagnetic behavior is only reached for temperatures above ~ 750°C. By cooling the system in the presence of the external field, a low magnetic signal re-appears at ~ 750ºC as shown in the inset of Fig 5.2 (a). Such results evidence that the analyzed sample presents a second Curie temperature at ~750°C, arising from a residual ferromagnetic phase.

Further metallographic inspection of the specimen subjected to this *in-situ* magnetic measurement reveals the absence of remaining α'-martensite in the bulk, as demonstrated by Fig. 5.3 (a). Besides, ferrite zones mixed with oxidized regions near the surface are clearly distinguished in Fig. 5.3 (b). This observation leads to the conclusion that the formation of complex Fe-Mn-based oxides during the experiment allows the stabilization of Mn-depleted zones (ferrite) close to the surface, whose Curie temperature was found to be ~ 750°C (JIANG et al., 1995; JIANG et al., 1996).

5.2.3 Microstructural characterization at intermediate stages of the γ-reversion

To obtain further microstructural information at intermediate stages of the γ-reversion, EBSD characterization was conducted on samples annealed up to 505 and 660ºC from dilatometry testing. As previously seen in Fig. 5.1 (a), such temperatures presented the

Figure 5.4 - (a) EBSD map of the 80% cold-rolled sample continuously annealed up to 505°C. **(b)** EBSD map of the 80% cold-rolled steel continuously annealed up to 660°C. In both figures, austenite and α'-martensite are represented by green and red, respectively.

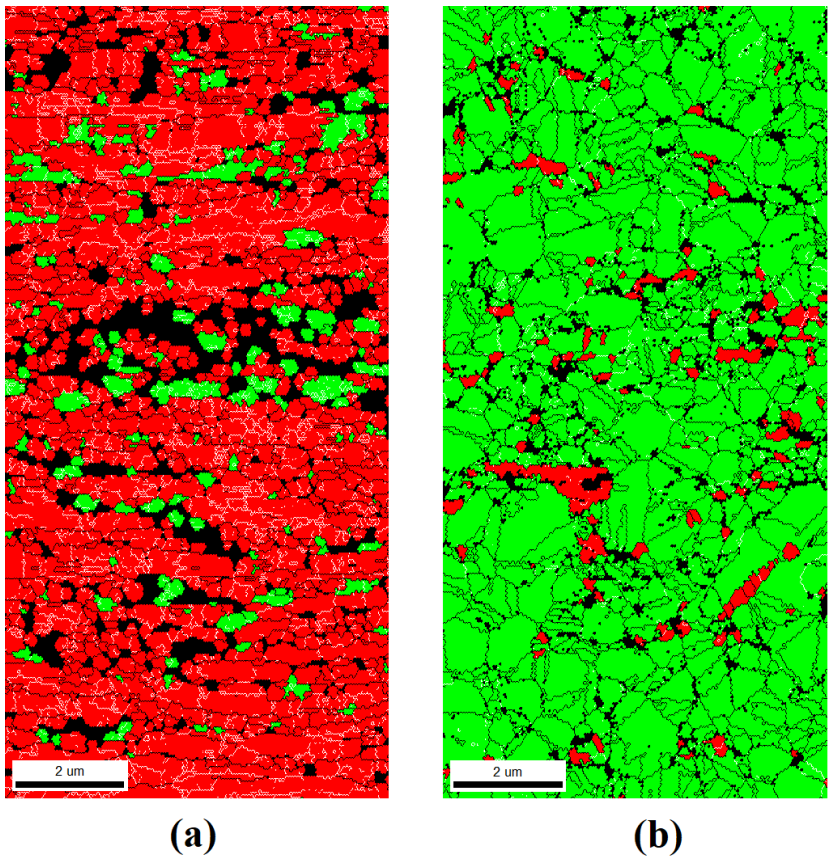

Source: elaborated by the author.

maximum rate of contraction $\frac{d\left(\frac{\Delta L}{L_0}\right)}{dT}$ during annealing, i.e. the maximum rate of γ-formation. Fig. 5.4 (a) shows the phase map of the material annealed up to 505ºC, where ultrafine reversed austenite (0.12 ± 0.09 μm^2) is observed to be dispersed within a tempered α'-matrix. Some austenite grains in this microstructure assume a near-equiaxial shape, while others are elongated. Fig. 5.4 (b) shows the phase map related to the sample continuously annealed up to 660ºC. In this case, a predominant equiaxed microstructure is observed, which is primarily austenitic, as expected. In turn, remaining α'-martensite is dispersed in the microstructure displaying both equiaxed and elongated morphologies.

5.2.4 Diffusion-controlled transformations simulated using the DICTRA method

Diffusion simulations in the vicinity of the γ/α' interface were performed by means of the DICTRA approach. For this purpose, a linear cell geometry with a planar interface between the phases is used as has been suggested in preceding studies (DMITRIEVA et al.,

2011). In the present case, the α'-martensitic microstructure of the cold-rolled steel was represented by a cell of 1 μm length. Fig. 5.5 (a) schematically shows the growth of a 0.3 μm region corresponding to γ during the simulations. At this point, it is worth to mention that bcc α'-martensite is usually taken as ferrite α in thermodynamic calculations (DMITRIEVA et al., 2011). Although kinetic parameters may vary between ferrite and α'-martensite due to lattice distortion and the enhanced dislocation density, satisfactory results were obtained when using the ferrite parameters as will be shown below.

The cell was also discretized as a linear grid and set as a geometric series. The density of points becomes higher near the interface. The chemical composition adopted for α' was the global chemical composition of the steel (Table 2.1). Because of the relatively low amounts of C and N in this steel only Fe, Mn, Al, and Si were considered in the kinetic DICTRA simulations. When C was included in the simulations, DICTRA did not succeed at finding the equilibrium point for austenite by considering that $M_{23}C_6$ carbide is the stable phase at 400°C rather than austenite. The possible effect of C on the austenite reversion kinetics was discussed in ref. (KWIATKOWSKI DA SILVA et al., 2018a). It was shown that for a Fe7Mn0.5Si0.1C (wt.%) alloy annealed at 450°C, Mn-enriched γ-nuclei can be poisoned by C and get converted into carbide nuclei, delaying the kinetics of γ-formation. For the present steel, the equilibrium amount of C remaining in the bcc α'-martensite matrix was calculated after the possible formation of the $M_{23}C_6$ with the aid of Thermo-Calc. Results showed that most of C is consumed by $M_{23}C_6$ formation so that austenite nucleation and growth at 400°C would occur in the near absence of C, allowing to neglect C from DICTRA simulations. In Section 5.2.6, it will be demonstrated that there is a very good agreement between the kinetic simulations (without considering C) and the experimental results. These observations reveal that the thermo-kinetic simulations are sufficiently reliable, suggesting that the low amount of C in the present steel (0.19 at.%, which corresponds to 0.042 wt.%) plays a minor effect on austenite nucleation and growth. After setting the boundary conditions, the simulation was performed using a heating rate of 0.05°C/s within the temperature range of 400 to 800°C.

Figure 5.5 (b) displays the DICTRA predicted changes in chemical composition across the γ/α' interface over the course of the continuous annealing. The first important observation is the partitioning of Mn between γ and α'. In fact, at the onset of the simulations (400°C), 27 at.% of Mn is observed on the γ-side of the interface whilst the α'-side displays a drastically Mn-depleted zone with a composition of 4.9 at.%. As the annealing proceeds

Figure 5.5 - (a) Schematic representation of the cell used for thermo-kinetic simulations (DICTRA). The cell (1 μm) shows the growth of a 0.3 μm austenite as an example. The density of points becomes higher near the surface. **(b)** Changes in chemical composition across γ/α' interface during continuous annealing with a heating rate of 0.05 °C/s, predicted by means of thermo-kinetics simulations with the aid of software DICTRA.

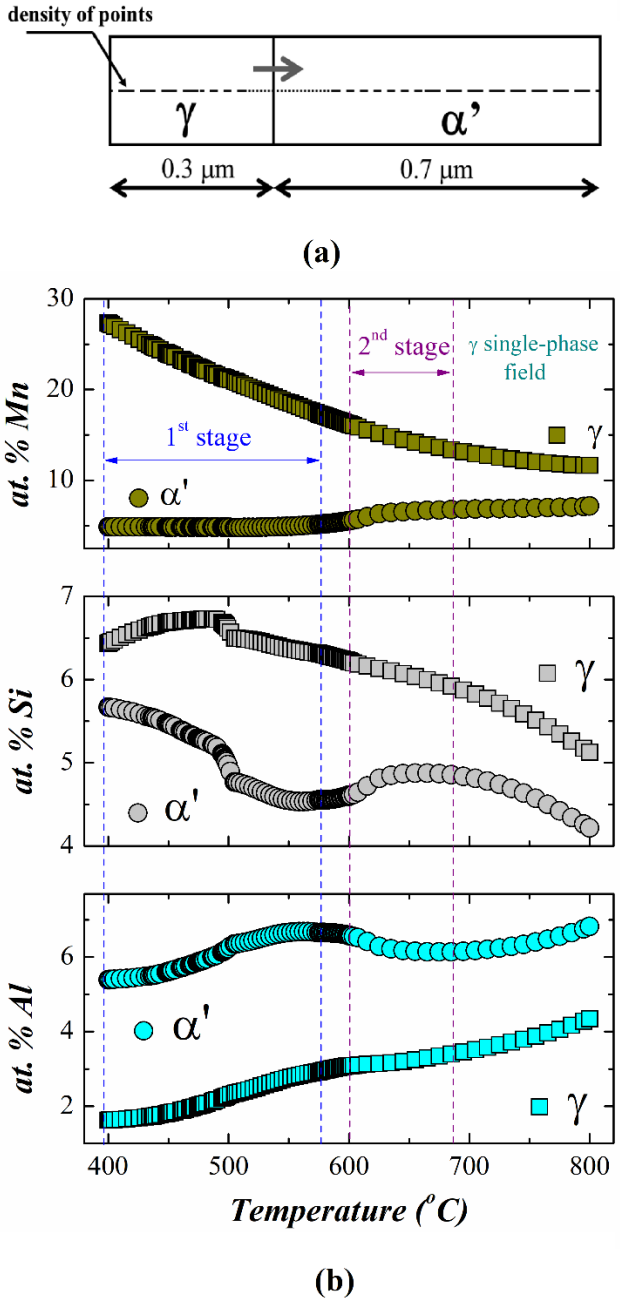

Source: elaborated by the author.

up to 600°C (i.e. onset of the second stage of the γ-reversion), the composition of Mn in the austenite continuously decreases until reaching 16.20 at.%. The Mn-composition profile inside the α'-martensite remains nearly unchanged up to 575°C. From this temperature on, its composition slightly increases reaching a value of 5.53 at.% at 600°C. Within the temperature range of 400-600°C, an overall view of the chemical profiles shows that Si on

the γ-side of the interface remains nearly unchanged with values of 6.4 ± 0.2 at.%. On the α'-martensite side, however, the Si content drops from 5.7 to 4.5 at.% at 600°C. Regarding the Al compositions, α'-martensite seems to be prone to retain a higher Al content during annealing. Both, γ and α' adjacent to the interface display an increase in Al composition with increasing annealing temperature up to 600°C. These results clearly support the observation that long-range diffusion is required within the temperature range of the first stage of γ-reversion. As a consequence of the Mn depletion in the remaining martensite, its reversion is expected to be delayed to higher temperatures.

By continuing the simulations from 600°C on, results suggest that the remaining α'-martensite is stable not only along the second stage of the γ-reversion but also in the expected γ single-phase field. These results clearly deviate from the observations made by using dilatometry and *in-situ* magnetic measurements (sections 5.2.1 and 5.2.2). DICTRA simulations are based on diffusion-controlled reactions (INDEN; NEUMANN, 1996; BORGENSTAM et al., 2000; SCHNEIDER; INDEN, 2005). Therefore, the discrepancy presented here suggests that long-range partitioning does not entirely control the course of the second stage of the γ-reversion.

5.2.5 Atom Probe Tomography (APT) measurements

APT measurements were conducted for the sample annealed up to 505°C to obtain detailed data on chemical gradients across the γ/α' interfaces developed during the first stage of the γ-reversion. Fig. 5.6 (a) presents the three-dimensional reconstruction for the sample annealed up to 505°C, for which two γ/α' interfaces were investigated. In this figure, the blue arrow indicates the sense of rotation of the tomographic reconstruction to facilitate visualization of the second interface. Iso-composition surfaces for Mn (yellow) corresponding to threshold values of 20 at.% are also included in this figure. The precipitation of Al-rich nanoparticles is revealed in terms of iso-composition surfaces with a 5 at.% threshold in Fig. 5.6 (a). Further characterization of these precipitates is beyond the scope of the present work. Nevertheless, they seem to be formed within the remaining α'-martensite indicating that precipitation aging in this phase can take place before or concurrently to γ-reversion.

The composition profiles calculated along the cylinders shown in Fig. 5.6 (a) are plotted in Fig. 5.6 (b) and (c). Mn compositions as high as 29.37 at.% can be found in the interior of γ whilst the remaining α'-martensite contains only ~10 at.% of Mn. Furthermore,

Figure 5.6 - Atom probe tomography results for the 80% cold-rolled sample continuously annealed up to 505°C. **(a)** Three-dimensional reconstruction of the specimen. Yellow and blue spheres represent Mn and Al ions, respectively. The iso-composition surfaces for Mn were constructed by using a threshold value of 20 at.%. Blue clusters indicate Al-rich nanoparticles in α'-martensite. **(b)** chemical profile obtained from the volume delimitated by the cylinder "1" in (a). **(c)** chemical profile obtained from the volume delimited by cylinder "2" in (a). **(d)** two-dimensional composition maps obtained from the reconstructed specimens in (a). **(e)** Enlarged view of the black frames displayed in (d).

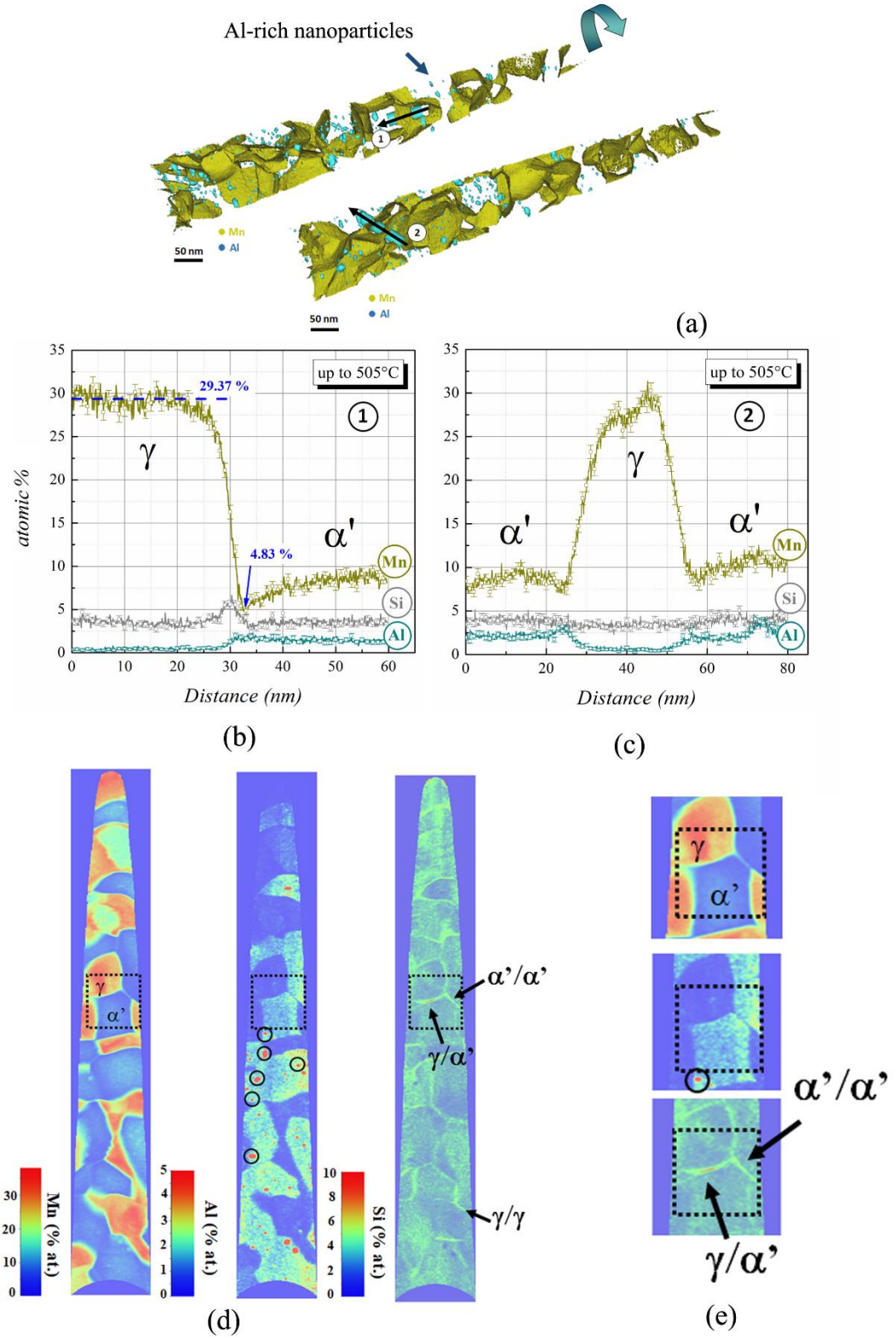

Source: elaborated by the author.

Mn-depletion is also noticeable near the interface on the α'-side (4.83 at.%). Al seems to partition preferentially to α'. At this point it is important to mention that these Al composition values may present a slight underestimation due to partial overlapping Fe and Al peaks in the mass spectrum (SEOL et al., 2012). In this case, one can also bear in mind the likely influence of instrumental parameters on non-preferential evaporation of certain ions (MILLER; SMITH, 1981). The partitioning of Si at γ/α' interfaces can be evaluated using the two-dimensional composition maps displayed in Fig. 5.6 (d). From this figure, both austenite and α'-martensite can be clearly distinguished in terms of their respective compositions, particularly their Mn and Al content. The presence of Al-clusters is also evident within the α'-martensite. Therefore, by using such differences in the Mn and Al content inside the grains, it is possible to identify γ/γ, γ/α', and α'/α' interfaces (see black frames in this figure). Additionally, Si accumulates to practically all of these interfaces and thus also helps revealing them in the APT data sets, as highlighted in Fig. 5.6 (e). At this point, one can bear in mind a minor influence of preferred evaporation of elements (i.e. instrumental artifacts) (MILLER; SMITH, 1981). However, the most prominent cause for Si enrichment at the interfaces can be attributed to the differences of its kinetics within both γ and α', since solute partitioning takes place to keep the local equilibrium at the interfaces.

Further APT analysis was conducted on a sample annealed at 600°C for 5 min. An isothermal annealing treatment was performed and mapped by EBSD to ensure that representative regions were chosen for extracting specimens for APT probing, Fig. 5.7 (a). Also, this temperature lies in the vicinity of the Curie temperature (viz. 625°C). In light of these observations, this short isothermal annealing at 600°C should trigger the second stage of the γ-reversion. The corresponding reconstructed APT dataset is shown in Fig. 5.7 (b). Mn ions in this figure are represented by yellows spheres. The iso-composition surfaces for Mn, in turn, were constructed using a threshold value of 12 at.%. From the volume delimitated by the cylinders in Fig 5.7 (b), chemical profiles were collected, as displayed in the same figure. From these profiles, partitioning of Mn and Al across the γ/α' interfaces is still observed. The compositions of Mn vary from ~ 18 to 24 at.% within the austenite, and ~ 6 at.% of Mn in the remaining α'. Again, Al partitions to α', although no Al-rich particles were observed in this sample. Si segregation on the γ-side of the interface is also quite noticeable. For this condition, the C profile obtained from APT probing from the region highlighted by cylinder 1 (Fig. 5.7b) is also shown as an example. As expected, higher

Figure 5.7 - (a) EBSD map of the 80% cold-rolled steel isothermally annealed at 600°C for 5 min. Green and red regions represent austenite and remaining α', respectively. **(b)** Corresponding three-dimensional reconstructed APT specimen. Yellow spheres represent Mn ions. Iso-composition surfaces were constructed with a threshold value of 12 at.%. The chemical profiles displayed in this figure were taken from the cylinders labeled as "1" and "2" within the reconstructed specimen. **(c)** Two-dimensional composition maps taken from (b).

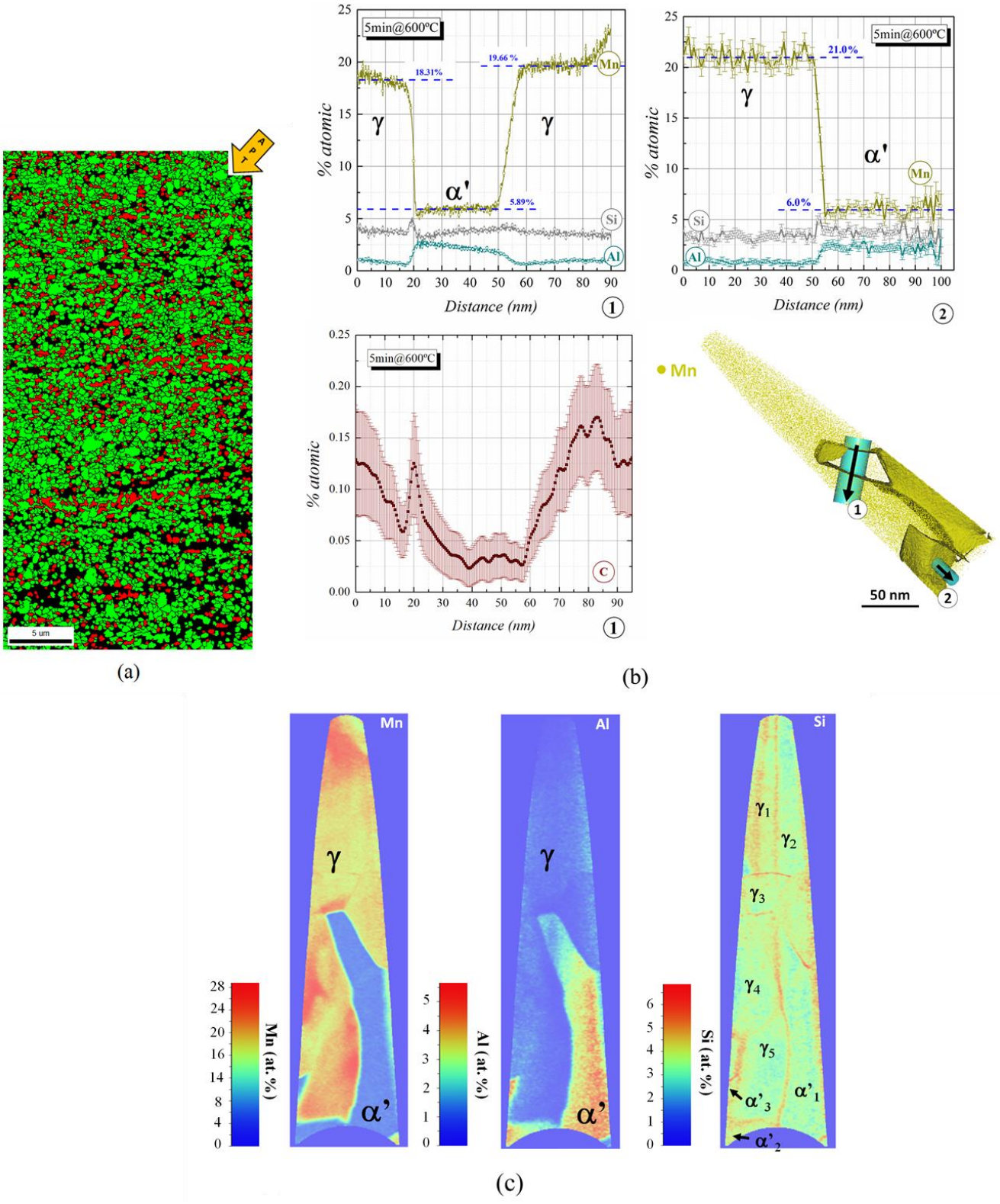

Source: elaborated by the author.

amounts of C are observed within γ compared to α'-martensite. Accumulations of C at the left-hand side of the γ/α' interface are also evident.

Figure 5.7 (c) shows two-dimensional composition maps collected from the reconstructed specimen (Fig. 5.7 a). In this figure, it is possible to distinguish austenite and α'-martensite grains due to the composition of their elements. Regarding Al and Mn profiles, heterogeneous distributions are clearly present within γ and α'. The presence of confined γ-zones with 24 at.% of Mn will be discussed below. In this figure, local Si accumulation is noticed near the γ/γ and γ/α' interfaces, whose composition ranges from 5 to 6 at.%. Similarly to Fig. 5.6 (d), solute partitioning is required to keep the local equilibrium at the interfaces. Therefore, different Si kinetics between phases may explain its piling up. For this sample, however, no information regarding Si accumulation at α'/α' interface can be inferred since we did not succeed in acquiring such boundary type.

5.2.6 Comparison between DICTRA simulated and APT results

The changes in Mn composition across the moving γ/α' interface simulated by DICTRA and displayed above in Fig. 5.5 (b) are reproduced in this section in the form of Mn-profiles for a continuous annealing process up to 505°C (Fig. 5.8a) and 600°C (Fig. 5.8b), respectively. For comparison, Figs. 5.8 (a) and (b) also display the Mn-profiles obtained from APT measurements as shown in Figs. 5.6 (b) and 5.7 (b) (cylinder 1), respectively. Fig. 5.8 clearly demonstrates that the partitioning behavior observed for Mn between γ and α' is practically the same as the one predicted by the DICTRA simulations for the local equilibrium at the interface. As mentioned in Section 5.2.4, Thermo-Calc calculations showed that most of C in our steel is expected to be consumed during $M_{23}C_6$ formation in the early beginning of the continuous annealing. Consequently, only a negligible amount of C would be available to participate of the γ-reversion. These observations and the very good quantitative agreement revealed in Fig. 5.8 lead us to conclude that the low C content of the present steel (0.19 at.%, which corresponds to 0.042 wt.%) exerts only a minor effect on the austenite formation kinetics, differently from medium-Mn steels containing higher amounts of C (0.1 wt.%) (KWIATKOWSKI DA SILVA et al., 2018a).

Figure 5.8 - Comparison between the Mn profiles obtained via APT with those obtained via DICTRA simulations (where no C content was included in the calculation) for **(a)** the continuous annealing up to 505°C and **(b)** at 600°C.

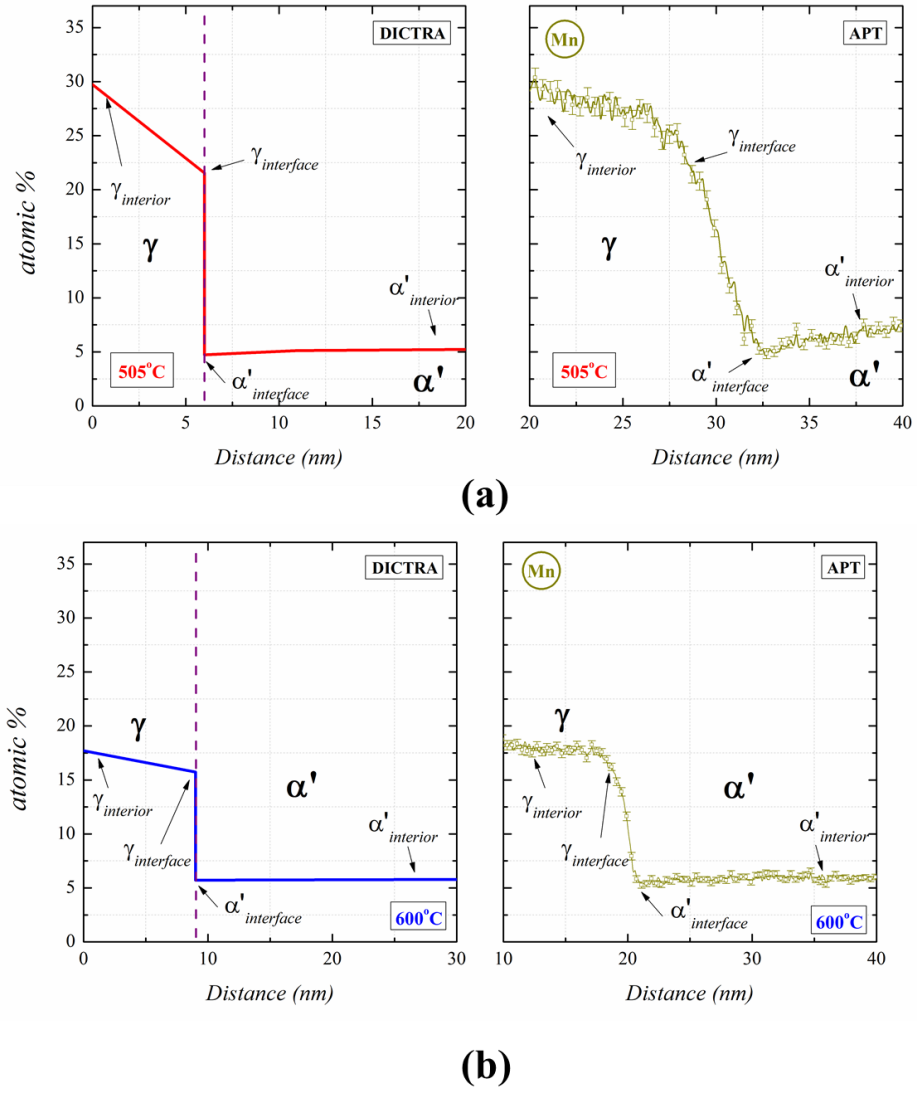

Source: elaborated by the author.

5.3. Discussion

5.3.1 Thermodynamic simulations and dilatometry results

Figure 5.9 shows an isopleth of the Fe-Mn-Al-Si-C system, calculated using Thermo-Calc. Differently from the kinetic simulations (section 5.2.4), here C was also considered for the thermodynamic simulations. The phase stability of this steel was previously shown in Section 3.2 (Fig. 3.1). However, Fig. 3.1 was constructed considering the presence of the impurities (e.g. S and P). In Fig. 5.9, the chemical composition of the present steel is highlighted, as well as the start (A_s) and finish (A_f) temperatures for both γ-reversion stages. By using the lever rule and taking into account the dilatometry values of $\frac{\Delta L}{L_0}$ from Fig. 5.1 (a), the volume fractions of austenite during continuous annealing were also determined

Figure 5.9 - Isopleth of the Fe-Mn-Al-Si-C system, calculated using the software Thermo-Calc. The global chemical composition of the present steel is highlighted by the blue-dashed vertical line. The start (A_s^1) and finish (A_f^1) temperatures for the first stage of γ-reversion are indicated by green stars; Analogously, A_s^2 and A_f^2 for the second stage of γ-reversion are represented by orange stars. The volume fraction of austenite for representative temperatures is represented as well.

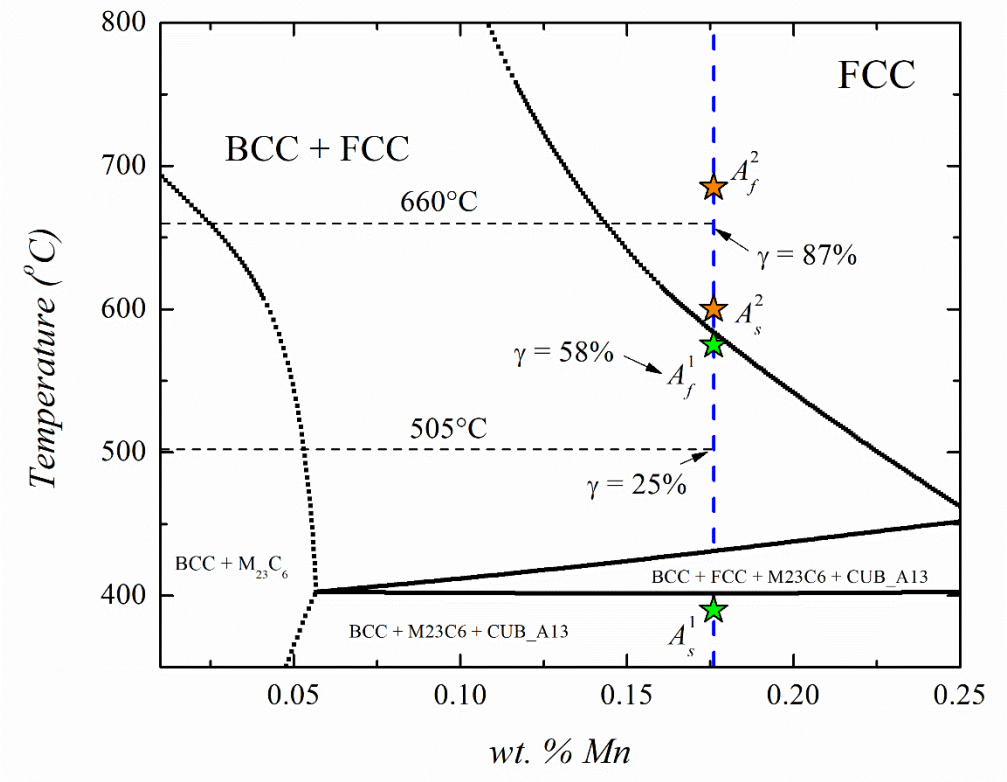

Source: elaborated by the author.

(LIU; SOMMER; MITTEMEIJER, 2003) and values are reported in Fig. 5.9. In this figure, the experimental value for $A_s^{1st\text{-}stage}$ lies approximately in the beginning of the intercritical field (α + γ). However, at $A_f^{1st\text{-}stage}$ = 575°C, 42% of the microstructure is still composed of remaining α'-martensite. In other words, the α' → γ transformation is not complete when the γ single-phase field is expected to initiate, viz. at 585°C. As previously observed by means of APT and DICTRA simulations, such differences arise from the strong chemical partitioning between γ and α'. The thermodynamic equilibrium used as a basis for constructing Fig. 5.9 provides only long-term (infinite) partitioning ranges and phase regions. However, the growth of austenite is controlled by local equilibrium (LE) at the interface (RAABE et al., 2013; DMITRIEVA et al., 2011). For instance, at $A_f^{1st\text{-}stage}$, the γ/α' interface grows towards α' under a local equilibrium given by 17.3 and 5.1 at.% of Mn at γ and α' sides, respectively (see Fig. 5.5). As a first consequence, the chemical composition of reversed austenite differs considerably from the global chemical composition of the steel (Table 2.1). Due to such changes, new equilibrium conditions are established and the remaining depleted-solute α' transforms into γ at higher temperatures. In addition, the second

peak associated with the reversion occurs just after the loss of ferromagnetism of the remaining α' (625°C), i.e. the remaining α' transforms back to austenite in a state of paramagnetism.

5.3.2 γ-reversion mechanisms

After nucleation, austenite grows essentially by either a diffusion- or an interface-controlled mechanism. The former involves long-range diffusion of elements, while for the latter, diffusion takes place only in a short-range, i.e. near the moving γ/α' interface. In this case, both parent and product phases assume the same chemical composition, i.e. the transformation proceeds locally partitionless (AARONSON; ENOMOTO; LEE, 2010). For the investigated steel, Fig. 5.10 shows the driving force for austenite formation driven by long-range (partitioning) and short-range (partitionless) diffusion. In this context, the driving force demonstrates how far the system is driven locally from the global equilibrium suggested by the phase diagram. The driving force magnitude for the α' → γ reaction controlled by the long-range partitioning regime was evaluated according to the approach implemented in Thermo-Calc for driving force calculations. For the present case, the partitioning driving force is approximated as the local difference in free energy between the matrix (α') and the equilibrium point of a α'/γ mixture. It is worth mentioning that the additional free energy contribution due to the capillarity of the nucleus (interfacial energy) is not considered in such procedure. The partitionless driving force, in turn, is given by the difference in free energy of the parent and product phases.

In Fig. 5.10, T_0 is the temperature where the free energies of γ and α'-martensite are identical (without taking into account the additional free energy contribution due to the capillarity of the nucleus). For temperatures below T_0 = 350°C, the partitionless driving force is negative and the γ-reversion can only be driven by the partitioning mechanism. In this work, the temperature of the onset of the γ-reversion is higher than T_0; i.e., in the temperature range where both mechanisms could be expected. However, the pronounced elemental partitioning observed by APT and DICTRA simulations between the adjacent phases (Fig. 5.5) suggests that the γ-reversion is mainly driven by the partitioning mechanism at its onset. By increasing the temperature to a value above T_0, the behavior of both, the partitioning and the partitionless curves, displays opposite trends. However, within the range of 350-660°C, the driving force for a partitioning reversion is always higher than the corresponding value obtained when assuming a partitionless transformation mechanism. The progress of the

Figure 5.10 - Driving force for austenite formation driven by partitioning and partitionless mechanisms, calculated using the software Thermo-Calc. T_0 denotates the temperature where the free Gibbs energy of both austenite and α'-martensite is the same.

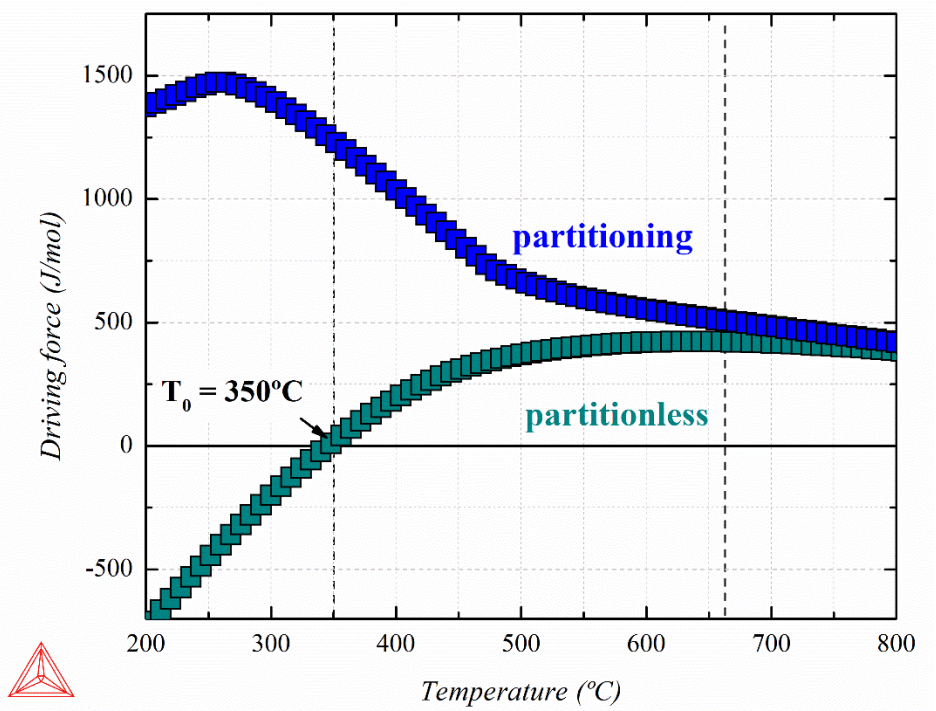

Source: elaborated by the author.

α' → γ reaction is hence mainly achieved by means of long-range diffusion during the first stage of austenite reversion, which is supported by the drastic chemical composition changes observed between the growing austenite and the remaining α'-martensite as revealed by APT data.

Yet in Fig. 5.10, the driving forces for both mechanisms seem to be the same for temperatures above 660°C. From the dilatometry measurements (Fig. 5.1a), the second stage of γ-reversion extends to a narrower range of temperature (85°C) when compared to the first one. Furthermore, the derivatives of these curves (Fig. 5.1b) show that the magnitude of contraction associated to this stage is smaller, as reported in other studies (MOSZNER et al., 2014). According to ref. (MOSZNER et al., 2014), such observations indicate a partitionless mechanism ruling the γ-reversion. Diffusion-based DICTRA simulations performed within the temperature range of 600-800°C (Fig. 5.5) predicted the stabilization of the remaining α'-martensite until the expected γ single-phase field. Such results clearly deviate from the experimental observations made by dilatometry. Therefore, it is plausible to infer that the partitioning mechanism is not the major responsible mechanism for transforming α'-martensite from 660°C on in this steel.

5.3.3 γ-nucleation and growth

In this section, the γ-nucleation and growth is discussed with the aid of thermo-kinetic simulations combined with experimental observations made via APT. Owing to the Gibbs-Thomson effect, the chemical composition of γ-nuclei may differ from the equilibrium composition of the α'/γ mixture given by the lever-rule (AARONSON; ENOMOTO; LEE, 2010; PORTER; EASTERLING; SHERIF, 2009). Bearing such effect in mind, the composition of a critical nucleus was calculated adopting the "parallel tangent construction" in diagrams G_p *vs* x_i, where G_p is the free energy of a phase "*p*"; and x_i the molar fraction of an element *"i"* (HILLERT, 1999). Fig. 5.11 shows the composition of the critical γ-nucleus within the temperature range of 350-600°C for the present steel.

Figure 5.11 - Critical composition of the γ-nucleus for several temperatures, calculated according to the parallel tangent construction in free energy curves as reported in ref. (HILERT, 1999).

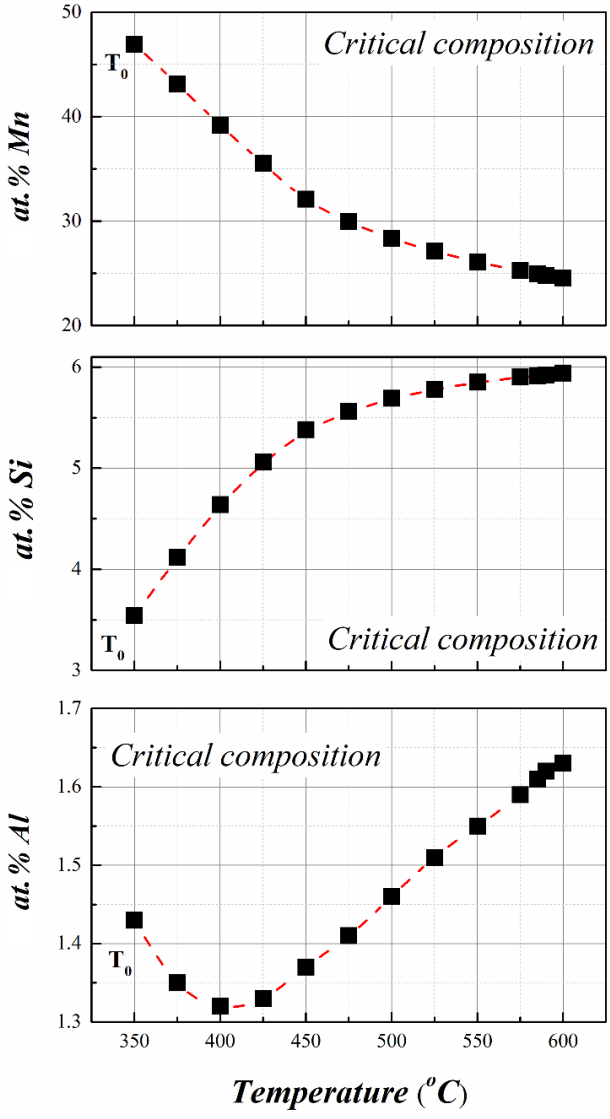

Source: elaborated by the author.

At the onset of the first (~ 400°C) and second (600°C) stages of the γ-reversion, the critical γ-nuclei display compositions of Mn considerably higher than the global chemical composition of the steel (viz. Mn = 16.9 at.%; Al = 3.4 at.%; Si = 6.1 at.%). Contrastingly, relative lower amounts of Si and Al are observed in the critical γ-nuclei. Results from Fig. 5.11 demonstrate once again the importance of long-range diffusion and elemental partitioning for providing the local chemical concentrations and thus driving forces required for a successful γ-nucleation event. In a recent work, Kwiatkowski da Silva et al. (2018b) showed that such chemical fluctuations in Fe-Mn alloys are caused by the segregation of Mn to the grain boundaries followed by the formation of spinodal-like fluctuations. These local compositional variations can be regarded as intermediate precursor states preceding the actual reversion. In other words, local spinodal Mn enrichment lowers the remaining barriers for nucleation. In light of these observations, it is possible to assume that γ-nucleation at a given temperature may occur predominantly at Mn enriched regions, whose composition reaches those values displayed in Fig 5.11.

5.3.3.1 γ-nucleation and growth at 500°C

To better understand the growth of γ-nuclei, further thermo-kinetic simulations were conducted reproducing isothermal annealings at 500°C and 600°C. Fig. 5.12 shows the composition profiles across γ/α' interfaces after 5 and 120 min at 500°C. In this figure, the critical composition of the nucleus is indicated by arrows. After 5 min, the Mn content of the former nucleus is nearly equal to the critical one (Fig. 5.12 a). Concerning Si in Fig. 5.12 (b), its pronounced piling up tendency (6.4 at.%) is noticed on the γ-side of the interface, after 5 min. DICTRA approach makes no consideration related to effects of solute drag on the mobility of the interface (BORGENSTAM et al., 2000). Therefore, the different Si kinetics within γ and α' may explain its pile up near the moving γ/α' interfaces.

After 120 min, the composition of the nucleus slightly depletes in Mn (Fig. 5.12 a). In fact, such reduction is expected to occur until reaching the local equilibrium that rules the interface motion. However, the simulations displayed in Fig. 5.12 show that homogenization of the growing austenite proceeds slow, due to the fact that the diffusion rates of Mn in austenite are low (DMITIREVA et al., 2011). In an opposite trend, the Si content in the former nucleus enriches to values similar to the local equilibrium of the interface (120 min). After 120 min, lower levels of Si accumulation in γ remain near the moving interface (Fig. 5.12 b). This observation suggests that the former Si-enriched interfacial zone is gradually

Figure 5.12 - Evolution of chemical profiles across γ/α' interface during austenite growth at 500°C. Results obtained by means of thermo-kinetics simulation using DICTRA. The corresponding critical composition of each element is also highlighted. Chemical profiles shown in terms of **(a)** Mn; **(b)** Si; **(c)** Al. The dotted vertical lines represent the position of the γ/α' interface for a time of 5 min.

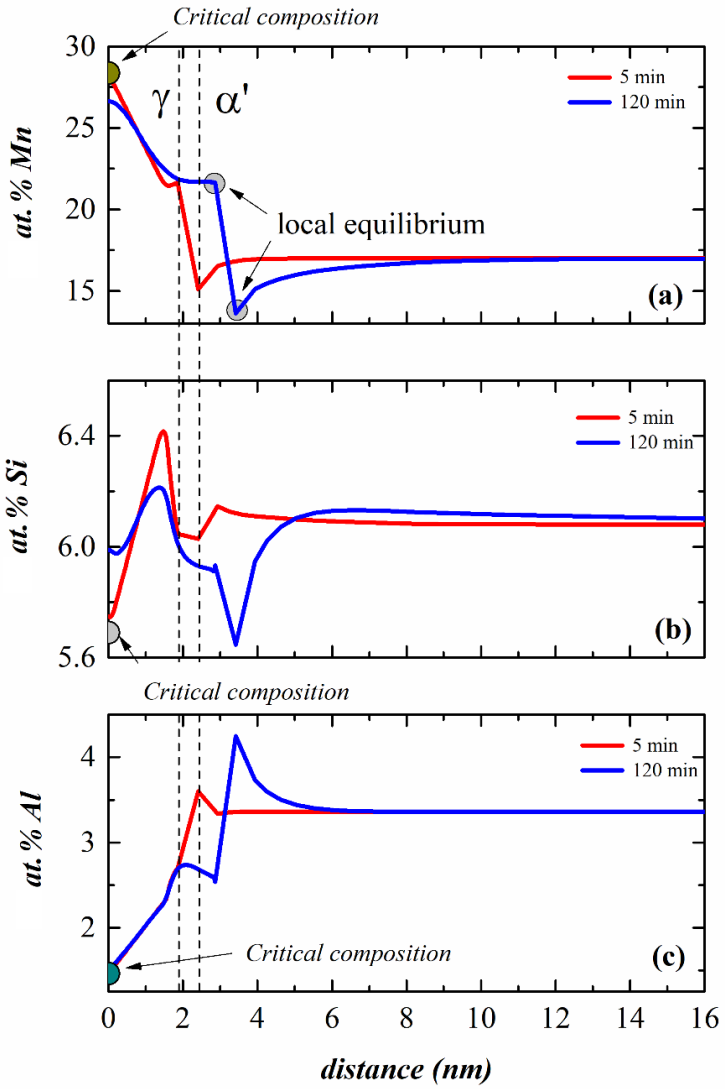

Source: elaborated by the author.

redistributed within γ with progressing annealing time. On the α'-side, the presence of a Si-depleted zone near the interface indicates a mass flux of Si towards γ. These simulations show the importance of local Si enrichment on the homogenization of γ. These results also demonstrate that γ-growth is followed by a significant consumption of Si from the α'-martensite. Finally, Fig. 5.12 (c) indicates that the local Al accumulation on the α'-side moves jointly with the interface. An overall view of Fig. 5.12 shows that γ-homogenization is preceded by local accumulation of Si and Al. The Si piling up trend is clearly supported by means of the two-dimensional composition maps (APT) displayed in Fig. 5.6, where Si-enriched interfaces were observed with similar compositions as those observed in Fig. 5.12.

5.3.3.2 γ-nucleation and growth at 600°C

Experimental observations of nucleation events are challenging. Nevertheless, Fig. 5.7 (b) throws light onto nuclei formed at 600°C. As an example, regions containing approximately 24 at.% Mn appear in the profile calculated from cylinder "1" in Fig. 5.7 (b), at a position of about 90 nm in the *"x"* axis. Notice that this value is similar with the critical composition at 600°C (5.9 at.% Si, 24.6 at.% Mn, and 1.6 at.% Al), which strongly suggests the presence of a former γ-nucleus.

Figure 5.13 - Evolution of chemical profiles across γ/α' interface during austenite growth at 600°C. Results obtained by means of thermo-kinetics simulation using DICTRA. The starting chemical composition were taken from the experimental APT results displayed in Fig. 8. The corresponding critical composition of each element is also highlighted. Chemical profiles shown in terms of **(a)** Mn; **(b)** Si; **(c)** Al. The dotted vertical line represents the position of the γ/α' interface for a time of ~ 5 min.

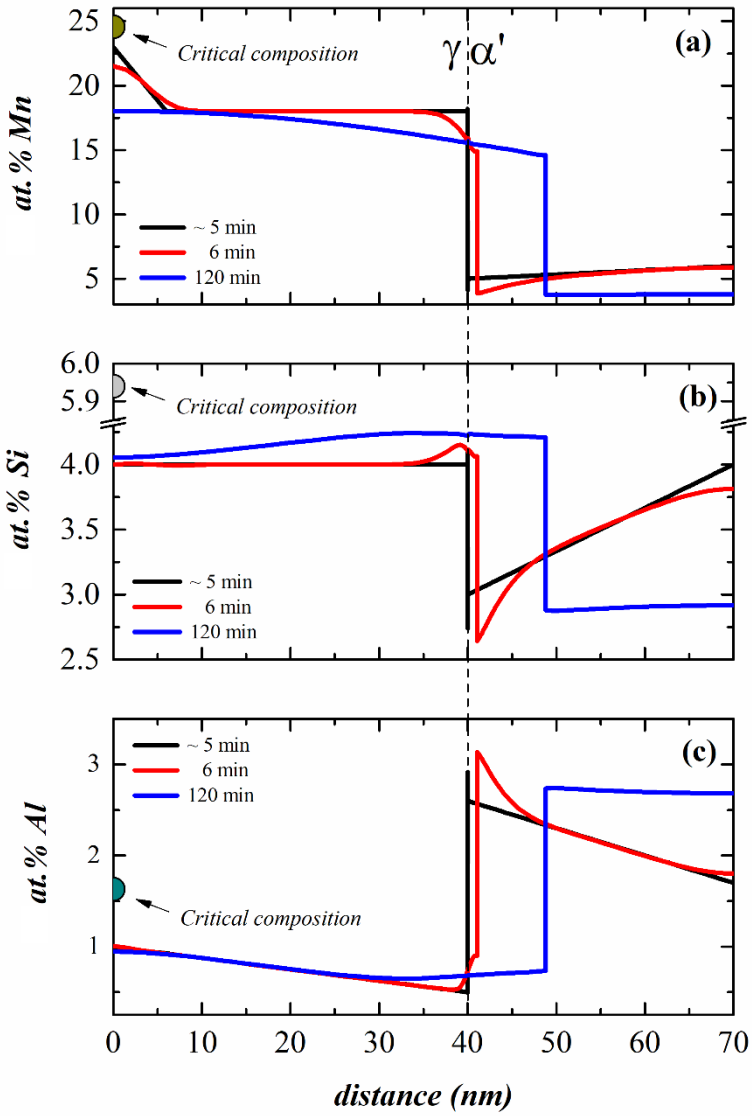

Source: elaborated by the author.

Using both chemical composition and phase size obtained experimentally in Fig. 5.7, additional simulations were performed and the results are shown in Fig. 5.13. The calculated critical compositions are also highlighted. Fig. 5.13 (a) shows that the Mn content of the nucleus gradually decreases to 18 at.% for 120 min simulation time at 600°C. As mentioned in section 5.3.3.1, this decrease is expected until compositional homogenization of the austenite is reached. Regarding Si, Fig. 5.13 (b) shows that accumulation near the interface is present at the beginning of the simulation. However, as the annealing proceeds, the Si profile broadens and a relatively homogenous composition is found in austenite. Consequently, the former nucleus slightly enriches in Si. Finally, no significant changes are observed for the Al profile in austenite. For 120 min, the Al profile is homogenous in the α'-martensite and the former local accumulation is not observed anymore. This result also shows that compositional γ-homogenization is controlled by the redistribution of piled-up solutes, as discussed in section 5.3.3.1.

5.3.4 Influence of elemental partitioning on the Curie temperature

With the aid of Thermo-Calc, the T_{Curie} of the present steel was calculated taking into account several chemical compositions for the α'-martensite reported in this work. Details about the calculation of the T_{Curie} are found in Chapter 7. Table 5.1 summarizes the results from our simulations in comparison to the experimental T_{Curie} (625°C). This table shows that if no long-range diffusion had occurred during annealing, the chemical composition of the α'-martensite would have been the same as the global chemical composition. Therefore, a T_{Curie} of 445°C would be expected. On the other hand, the chemical compositions of the α'-martensite experimentally determined via APT and simulated using DICTRA are in good agreement. Smaller Al contents in APT specimens are likely caused by instrumental errors, as already discussed. In spite of this, all values of T_{Curie} corresponding to these compositions are in very good agreement with the experimental value of 625°C. They also agree with a recent study on the influence of partitioning on the Curie temperature reported by Dastur et al. (2018) for a steel containing 18 wt.% Mn, 2 wt.% Al, 2 wt.% Si, and 0.04 wt.% C. These results show that elemental partitioning which occurs during austenite nucleation and growth strongly influences the ferromagnetic behavior of α'-martensite.

Table 5.1 - Curie temperatures of α'-martensite predicted for different chemical compositions, taken from APT measurements and predicted with the aid of DICTRA, as well as the experimentally observed Curie temperature.

Condition	at.% Mn	at.% Si	at.% Al	T_{Curie} (°C)
ε = 1.56 cold-rolled	16.9	6.1	3.4	445
up to 600°C (DICTRA)	5.54	4.61	6.59	632
isothermal at 600°C (APT, cylinder 1)	5.89	3.64	2.30	653
isothermal at 600°C (APT, cylinder 2)	6.02	3.67	2.20	651
in-situ magnetic measurements	-	-	-	625

Source: elaborated by the author.

5.4 Summary and conclusions

Austenite reversion in a cold-rolled 17.6 wt.% Mn steel was studied during slow continuous annealing by means of dilatometry and *in-situ* magnetic measurements. In light of the results reported in this work the following conclusions are drawn:

i) During slow continuous annealing, austenite reversion is not yet complete when the equilibrium γ single-phase field as predicted by Thermo-Calc is reached. According to thermo-kinetic simulations, strong elemental partitioning is required for austenite nucleation and growth, as was clearly confirmed by APT. The APT results showed that Mn-enriched regions corresponded to reversed-γ while Mn-depleted zones were the remaining α'-martensite. Due to its lower Mn content, the remaining α' experienced the $\alpha' \rightarrow \gamma$ reaction at higher temperatures. Therefore, austenite reversion during continuous heating was observed to be split into two stages, with maximum transformations rates at 505 and 660°C. The second peak, i.e. the second distinct step of the austenite reversion (660°C) occurred for a paramagnetic α'-martensite, whose Curie temperature was 625°C.

ii) Under isothermal conditions at 500 and 600°C, thermo-kinetic simulations demonstrated that the compositional homogenization of growing austenite is determined by the redistribution of the piled-up solutes, especially of Si. Such simulations were also confirmed by means of APT, which clearly demonstrated the strong tendency of local Si accumulation to interfaces, occurred to keep the local equilibrium.

iii) Finally, the Curie temperature of the alloy was calculated taking into account the chemical composition of the remaining α' determined via simulations and APT. It turned out that the obtained values hold excellent agreement with the experimental value of 625°C, determined by *in-situ* magnetic measurements. Therefore, elemental partitioning influences not only austenite nucleation and growth but also the ferromagnetic behavior of the α'-martensite.

Chapter 6

Magnetic properties: study of strain-induced martensite formation, austenite reversion, and athermal α'-formation

6.1 Introduction

In addition to the strain-induced martensite, many high-Mn steels also experience athermal formation of ε- and α'-martensites upon cooling. The athermal formation of ε- occurs when the driving force for $\gamma \rightarrow \varepsilon$ reaction ($\Delta G^{\gamma \rightarrow \varepsilon}$) is greater than the increase in energy associated to the creation of new γ/ε interfaces ($\sigma^{\gamma/\varepsilon}$) (PISARIK; VAN AKEN, 2014). These two energy terms are, in turn, associated to the staking fault energy (SFE) of the material according to Eq. (3.1), as proposed by Olson and Cohen (1976).

Similarly, spontaneous formation of α' takes place when the driving force for $\gamma \rightarrow \alpha'$ reaction counterbalances the increase in energy associated to lattice distortion in austenite caused by α'-martensite formation (FIELD; BAKER; VAN AKEN, 2017). In any case, α'-martensite is observed to nucleate either directly from γ (PISARIK; VAN AKEN, 2014) or to be dependent on the presence of prior ε phase (KELLY, 1965; LU et al., 2011). Athermal martensite formation is also influenced by the annealing temperature, austenite grain size, cooling rate, and chemical composition (LU et al., 2011; TAKAKI; NAKATSU; TOKUNAGA, 1993; SAHU et al., 2007; DAFÉ et al., 2013; LI et al., 2018).

Both, the strain-induced and the athermal α'-martensite variants are ferromagnetic and therefore magnetic measurements are an excellent non-destructive tool for tracking bulk α'-martensite formation upon deformation or cooling. Since magnetization saturation (M_s) is related to the volume fraction of the ferromagnetic phase, it is commonly used for evaluating the amount of SIM in several austenitic steels (TAVARES et al., 2002; MITRA et al., 2004; MUMTAZ et al., 2004a; MÉSZÁROS; PROHÁSZKA, 2005; SOUZA FILHO et al., 2016; MA et al., 2018). Important information regarding size and distribution of α' can also be obtained by means of coercive field (H_c) probing, as reported elsewhere (SOUZA FILHO et al., 2016). In comparison to other austenitic steels, only a few studies focused on magnetic properties of high-Mn steels (MUMTAZ et al., 2004a; GARSHELIS; FIEGEL, 1982). To the best of our knowledge, the correlation between H_c and microstructural evolution has not been reported in the literature for high-Mn steels yet. The aim of this Chapter is to understand the influence of SIM formation and austenite reversion on the

magnetic properties of the 17.6 wt.% Mn steel. For this purpose, the steel was cold rolled up to 80% of thickness reduction (ε = 1.56) and further isothermally annealed up to 800°C. Magnetic measurements were conducted at room temperature for both deformed and annealed states. Further *in-situ* magnetic measurements were used to track the athermal formation of α'-martensite during controlled cooling after complete austenite reversion. Here, it is important to mention that the austenite reversion upon continuous annealing was already reported in Chapter 5.

Since α'-martensite is a ferromagnetic phase, textured and elongated α'-grains developed during cold-rolling may present some magnetocrystalline anisotropy, which is highly dependent on their crystallographic orientation (CULLITY; GRAHAM, 2009). Furthermore, related to the morphology of α'-grains, shape anisotropy effects arising from demagnetizing fields exert a strong influence on coercive field (SOUZA FILHO et al., 2016; ELMASSALAMI, et al., 2011), one of the magnetic parameters investigated in this work. In this context, the combination of such anisotropic effects leads to an easy magnetization axis along the rolling direction (RD). For this reason, in this study all magnetic fields were applied parallel to the RD of the rolled plates. In combination with magnetic measurements, microstructural characterization of the samples was also performed using electron backscatter diffraction (EBSD), electron channeling contrast imaging (ECCI), X-ray diffraction, and thermodynamic modelling.

6.2. Results and discussion

6.2.1 Magnetic properties of the cold-rolled steel

Figure 6.1 (a) shows the evolution of M_s values as a function of strain. From this figure, M_s increases with strain with a parabolic-like behavior, a clear evidence of SIM formation previously discussed in Chapter 4. According to the literature, M_s = 155 emu/g can be assumed as the intrinsic saturation magnetization of α'-martensite in high-Mn steels (MA et al., 2016). Using such value and the M_s results depicted in Fig. 6.1 (a), the amount of α'-martensite was calculated as a function of strain, as also shown in Fig. 6.1 (a). From this figure, the amounts of SIM obtained via magnetic measurements are in very good agreement with those obtained by XRD (Fig. 4.1). Fig. 6.1 (b) shows the corresponding H_c values for the cold-rolled samples. The coercivity sharply increases at ε = 0.22 but drops for larger strains. The coercive field of SIM in austenitic steels is strongly dependent on its size, shape, and distribution (MUMTAZ et al., 2004a). In a previous work, it was also evaluated

Figure 6.1 - (a) Evolution of the saturation magnetization (M_s) of the 17.6Mn-TRIP steel as a function of equivalent strain (ε), represented by black circles. Yellow circles show the volume fraction of α'-martensite, calculated by taking into account the M_s values and the intrinsic M_s value of 155 emu/g reported in ref. (MA et al., 2016). **(b)** evolution of the coercive field (H_c) of the 17.6Mn-TRIP as a function of strain (ε).

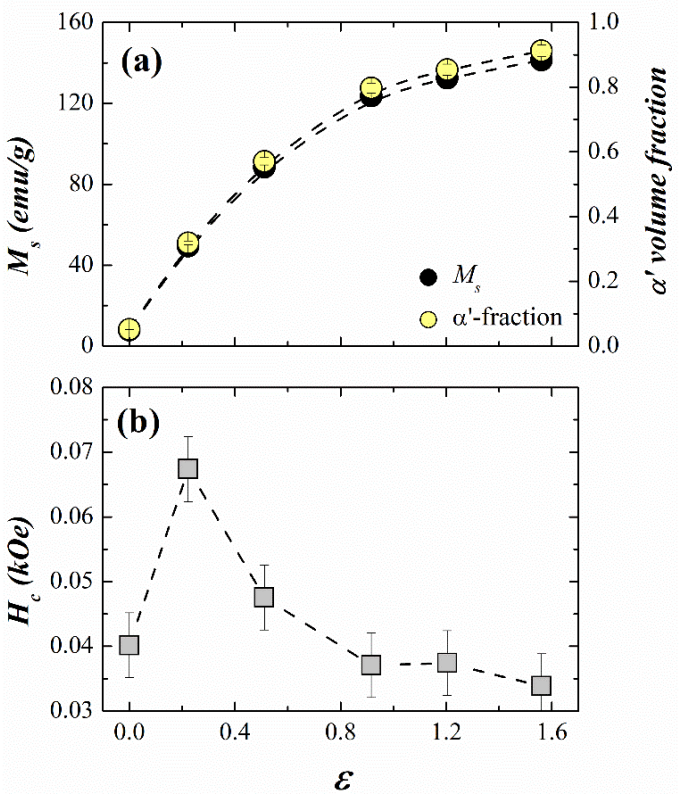

Source: elaborated by the author.

a similar behavior for a cold-rolled AISI 201 steel (SOUZA FILHO et al., 2016). Strong magnetic shape anisotropy is found when the α' fraction is small and relatively dispersed in the austenite matrix. As a consequence, large H_c values are detected. Contrastingly, when coalescence of α' occurs due to deformation, one can expect a decrease of such anisotropy which leads to lower values of H_c. Back to Fig. 4.8, it can be noticed that amount, morphology, and distribution of α'-martensite drastically change from thin dispersed laths at $\varepsilon = 0.22$ to elongated and coalesced grains at $\varepsilon = 1.56$. Based on these results and in light of refs. (MUMTAZ et al., 2004a; SOUZA FILHO et al., 2016), it is plausible to assume that magnetic shape anisotropy rules the coercivity of α'-martensite in this steel.

6.2.2 Isothermal annealing of cold-rolled samples (ε = 1.56)

Figure 6.2 shows both M_s and H_c values taken from the hysteresis loops obtained at room temperature (not shown) of the rolled 17.6 Mn-TRIP steel ($\varepsilon = 1.56$) annealed up to 800ºC for several annealing times. From Fig. 6 (a), in comparison with the deformed material, a slight increase of M_s can be noticed at 350ºC, as clearly evidenced by the inset in

Fig. 6.2 (a). Such anomalous increase in magnetization at low temperatures have been observed in other steels with martensitic microstructures (GUY; BUTTLER; WEST, 1983; PADILHA; PLAUT; RIOS, 2003). In the present work, this phenomenon will be carefully investigated in Chapter 7. By increasing the annealing temperature, a monotonic decrease in M_s is noticeable evidencing the austenite reversion. Interestingly, M_s presents an annealing time dependence at 500 and 600°C, an indication of long-range diffusional transformation (TOMIMURA; TAKAKI; TOKUNAGA, 1991; TAKAKI; TOMIMURA; UEDA, 1994). On the other hand, for $T_{isothermal} \geq 700$°C, annealing for 5 min is sufficient to decrease M_s nearly to zero, i.e. complete austenite reversion. Regarding the $\alpha' \rightarrow \gamma$ transformation, important information regarding the distribution of martensite can be obtained from the H_c values. From Fig. 6.2 (b), the values of H_c increase considerably at 500 and 600°C,

Figure 6.2 - (a) Magnetization saturation of the 17.6Mn-TRIP steel ($\varepsilon = 1.56$ steel) isothermally annealed up to 800°C for several times. **(b)** Corresponding coercive field (H_c) for the same isothermal conditions. Both parameters were taken from hysteresis loops (not shown) obtained at room temperature.

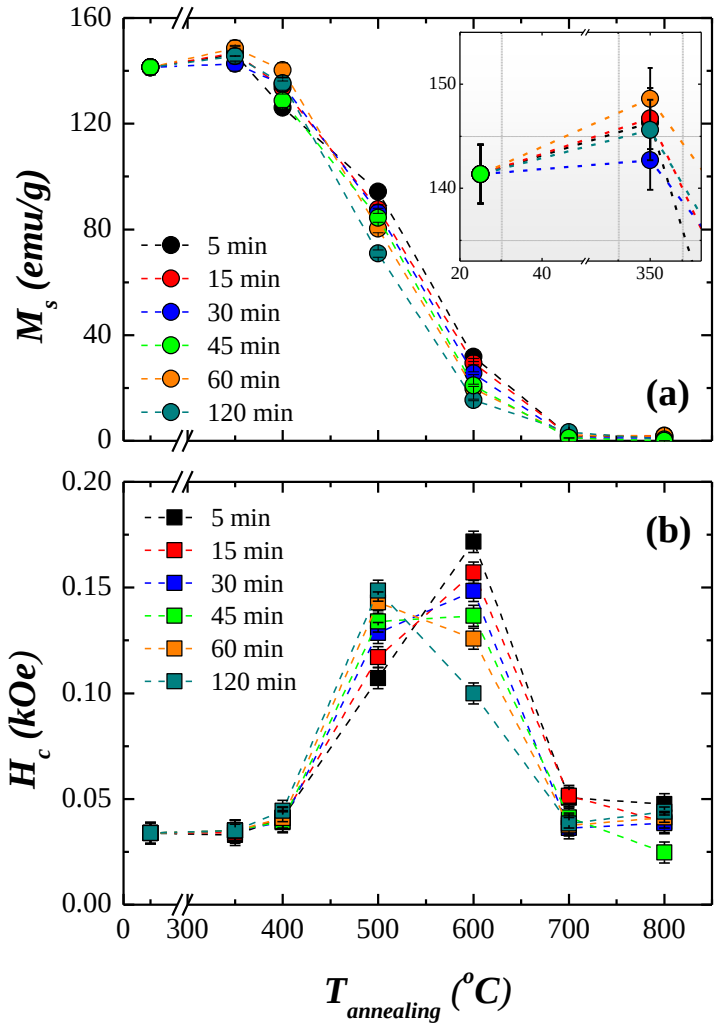

Source: elaborated by the author.

in correspondence to the decreasing values of M_s. As consequence of austenite reversion, the increasing number of γ/α interfaces leads to the fragmentation of the prior cold-rolled α'-martensite. Therefore, the ferromagnetic zones become less connected and the peak values of H_c at 500 and 600°C are due to localized demagnetizing fields, i.e. strong magnetic shape anisotropy (MUMTAZ et al., 2004b). Even from Fig. 6.2 (b), it is worth mentioning that the annealing time dependence of H_c at 500 and 600°C presents opposite trends. At 500°C, the ever increasing H_c values with annealing time shows that the maximum number of α/γ interfaces is not reached at this temperature. Such maximum number, however, can be achieved for 5 min of annealing at 600°C. For longer annealing times at 600ºC, the number of α/γ interfaces decreases with the increasing amounts of austenite, and H_c decreases as well. Finally, at higher temperatures (e.g., 700 and 800ºC) where austenite reversion can occur by an interface-controlled mechanism, the fast shrinkage of α'-martensite reduces H_c to zero.

To corroborate the observations shown in Fig. 6.2, representative samples were imaged via the ECCI-SEM technique. In this regard, Fig. 6.3 shows the microstructural evolution of the 80% cold-rolled steel annealed within the temperature range of 500-800°C for 5 min. With the aid of the ECCI technique, very fine substructures can be identified within the microstructure (ZAEFFERER; ELHAMI, 2014; WU et al., 2016). Consequently, it allows the differentiation of austenite from α'-martensite in the beginning of austenite reversion in each condition of isothermal annealing. Fig. 6.3 (a) shows the microstructure of the material after 5 min of annealing at 500ºC. In this figure, diffuse areas with a high dislocation density corresponding to recovered α'-martensite are pointed out by arrows. Dispersed γ-nanograins are also observed in these microstructures, as highlighted in Fig. 6.3 (a). This result shows that the formation of very small austenite regions is sufficient to induce high demagnetizing fields on α' in the early stages of austenite reversion (high values of H_c). At 600°C (Fig. 6.3 b), α' is present in a lesser amount, explaining the sharp drop in M_s in Fig. 6.2 (a). It is also observed in this figure the presence of nanotwins subdividing the austenite in this microstructure. Finally, annealing for 5 min at 700 and 800°C is enough to remove the α'-martensite, leading to a fully γ-recrystallized microstructure, as seen in Figs 6.3 (c) and (d), respectively. Also, it is noticed the presence of annealing nanotwins as well as stacking faults within austenite.

Figure 6.3 - Microstructural evolution of the 17.6Mn-TRIP steel (ε = 1.56 steel) annealed for 5 min at **(a)** 500°C; **(b)** 600°C; **(c)** 700°C; and **(d)** 800°C. Images obtained with the aid of electron channeling contrast image (ECCI).

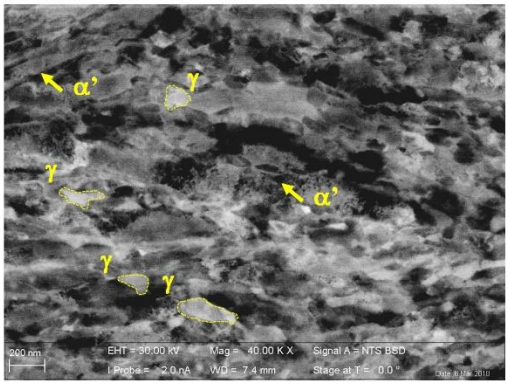

(a)

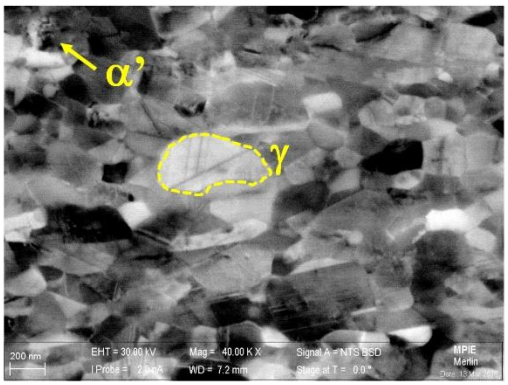

(b)

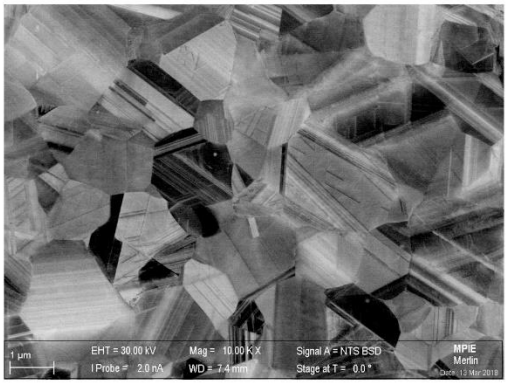

(c)

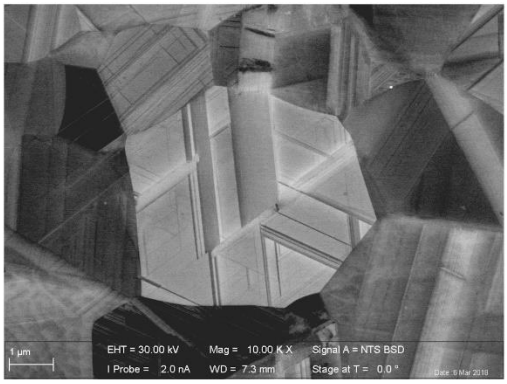

(d)

Source: elaborated by the author.

6.2.3 In-situ magnetic measurements taken during cooling of samples (ε = 1.56) *isothermally annealed at 800°C*

The cooling temperature dependence of the magnetization of the 17.6Mn-TRIP steel (ε = 1.56), after isothermal annealing at 800ºC for several annealing times, is displayed in Fig. 6.4 (a). The corresponding derivative of *M(T)* curves are displayed in Fig. 6.4 (b). Upon cooling, the material displays a paramagnetic behavior between 800 and 743°C. The presence of a ferromagnetic signal at 743°C can be attributed to the formation of ferrite layers on surface of the samples as a consequence of oxidation, as previously discussed (Section 5.2.2). However, with the progress of cooling, we see a further increase in magnetization at ~ 690°C for all samples (see the corresponding peaks in Fig. 6.4 b). Metallographic inspection revealed the origin of such ferromagnetic signal. EBSD maps taken next to the surface of the sample annealed at 800°C for 30 min are also shown in Fig. 6.4 (b). In this figure, the microstructure is represented by means of image quality (IQ), inverse pole figure (IPF), and phase maps. In Fig. 6.4 (b), from the top to the bottom it is possible to clearly distinguish four different regions. The first one is comprised of a mixture of remaining fcc phase interspersed within oxides. Right below it, relatively coarse bcc-grains are observed (second region), followed by thin and vertically oriented bcc-grains (third region). Finally, in the fourth region a mixture of bcc, fcc and hcp phases coexists with oxidized areas. The presence of both hcp- and bcc phases in the fourth region is a likely consequence of the destabilization of austenite due to Mn-loss to Fe/Mn-based oxides. Based on Fig. 6.4 (b), it is also plausible to infer that the chemical composition of ferrite varies according to the region it belongs to. Therefore, it is possible to assume that the ferromagnetic signal observed at ~ 690°C in Fig. 6.4 (b) comes from the bcc-phase formed as a consequence of oxidation developed on the surface of the samples.

Back to Fig. 6.4 (a), with exception of the sample annealed for 5 min, all samples display a slight upturn of *M* for $T_{cooling}$ < 100°C. From Figs. 6.2 and 6.3 (d), it was previously seen that austenite reversion is complete after 5 min annealing at 800ºC. Therefore, the increase in *M* for $T_{cooling}$ < 100°C is certainly due to the formation of athermal α'-martensite, as reported for other austenitic high-Mn steels (MITRA et al., 2004; PISARIK; VAN AKEN, 2014). The temperature corresponding to the onset of athermal α' formation is termed $M_s^{\alpha'}$. To determine the values of $M_s^{\alpha'}$, all curves from Fig. 6.4 (a) were accordingly fitted between 200-100°C. The last experimental value of *M* belonging to the fitted curves was considered to be $M_s^{\alpha'}$, as depicted in Fig 6.5, for a representative sample. Using this protocol, it was

Figure 6.4 - (a) Cooling temperature dependence of the magnetization (M) of the 17.6 Mn-TRIP steel (ε = 1.56 steel), after isothermal annealing at 800ºC for several times. The inset shows the upturn of M for $T_{cooling}$ < 100°C, evidencing the formation of athermal α'-martensite. **(b)** Corresponding derivative curves showing peaks at ~ 690°C, regarding the increase in magnetization. EBSD maps conducted near the surface of the 80% cold-rolled sample annealed at 800°C for 30 min. These maps reveal the origin of the magnetic signal at ~690°C: formation of bcc-phase as a consequence of oxidation near the surface of the sample.

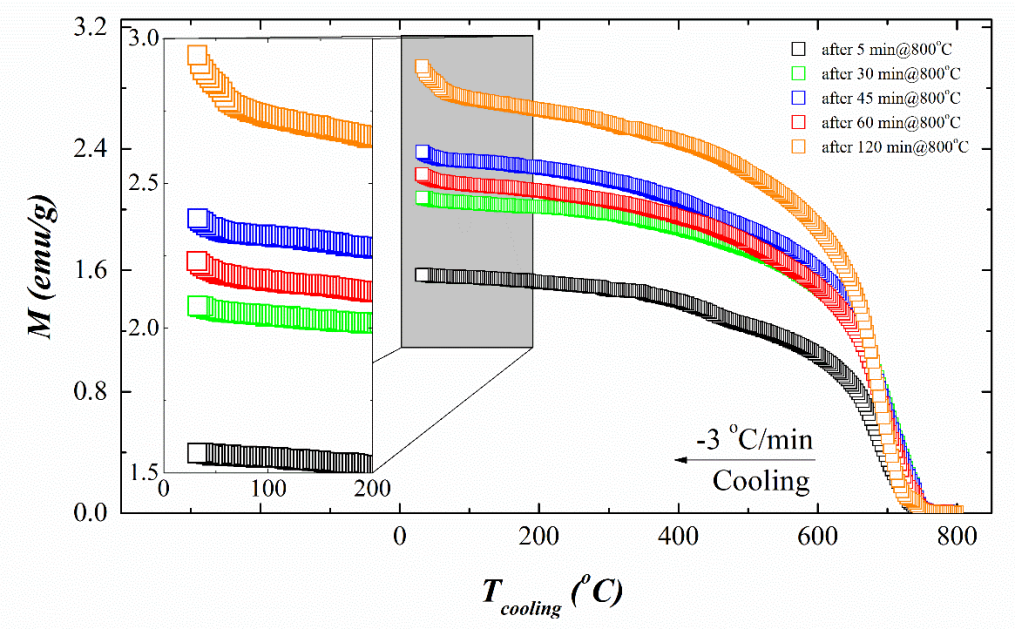

(a)

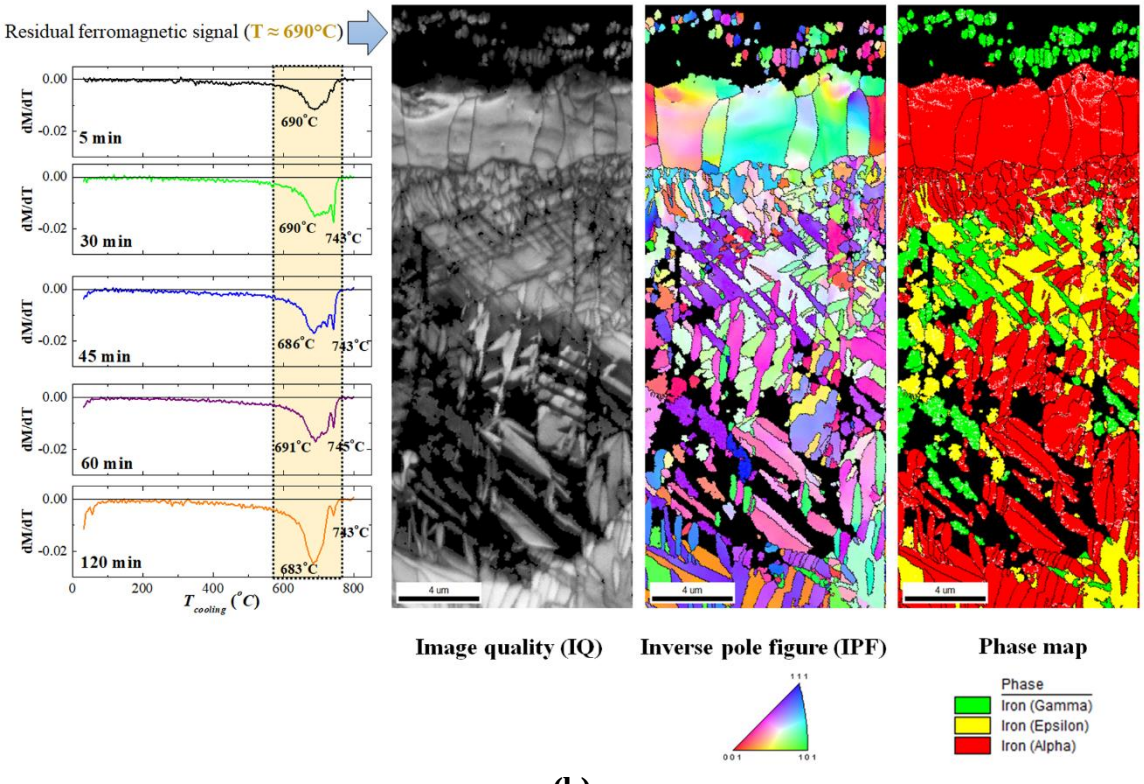

(b)

Source: elaborated by the author.

Figure 6.5 - Protocol used to determine the temperature corresponding to the onset of athermal α' formation ($M_s^{\alpha'}$). In this figure, it is taken as an example the cooling process for the $\varepsilon = 1.56$ steel annealed at 800°C for 60 min. The complete curve for this condition can be seen in Fig. 8 (a).

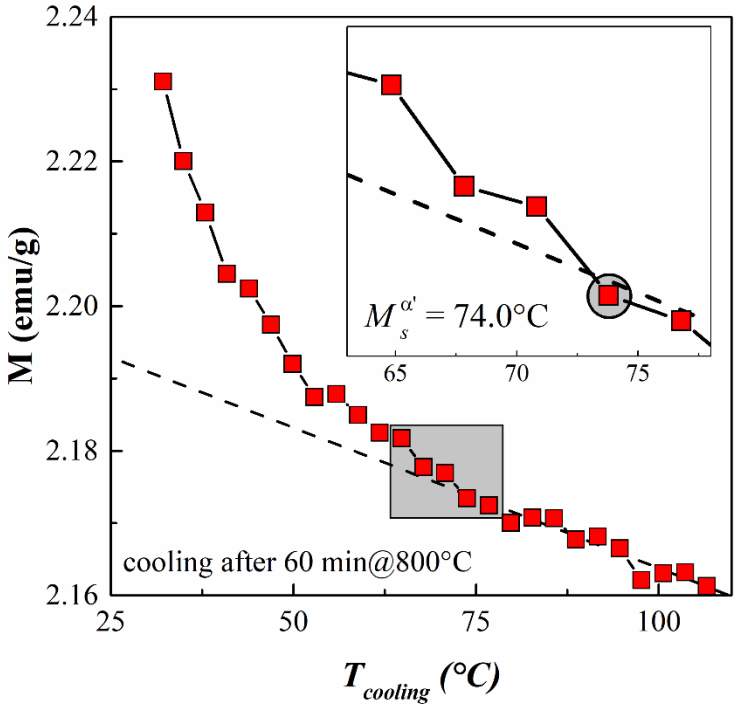

Source: elaborated by the author.

found that the samples annealed for 30, 45, and 60 min present nearly the same values of $M_s^{\alpha'}$ (71, 71, and 74°C, respectively). However, increasing the time of annealing to 120 min, $M_s^{\alpha'}$ shifts to a value of ~ 95°C.

Figures 6.6 (a-c) show the microstructures after annealing for 5, 30, and 120 min at 800°C, respectively. From Fig. 6.6 (a), after 5 min, the microstructure consists of recrystallized γ-grains (5 ± 1 μm) subdivided by athermal ε-plates with a negligible amount of athermal α'-martensite not detected by magnetic measurements (see Fig. 6.4 a). Larger γ-grains, also subdivided by ε-plates, are noticed after 30 min of annealing (Fig 6.6 b). For this condition, athermal α' seems to nucleate preferentially at γ/ε interfaces and grows towards the interior of ε-martensite, displaying a tiny lenticular morphology. After 120 min, austenite grain growth is evident (17 ± 6 μm), as well as the intersection of ε-plates associated with the increasing amount of athermal α' (Fig. 6.6 c). The characteristics of ε-plates regarding their growth is in a quite good agreement with the results reported by Takaki and co-authors for a Fe-15%wt. Mn model alloy (TAKAKI; NAKATSU; TOKUNAGA, 1993).

The influence of grain size on martensitic transformation is reported for several authors (TAKAKI; NAKATSU; TOKUNAGA, 1993; JIANG et al., 1995; JIANG et al.,

Figure 6.6 - *Post-mortem* microstructures of the 17.6Mn-TRIP steel (ε = 1.56 steel) after being annealed at 800°C for **(a)** 5 min, **(b)** 30 min, **(c)** and 120 min and controlled-cooled to room temperature in the presence of an external magnetic field.

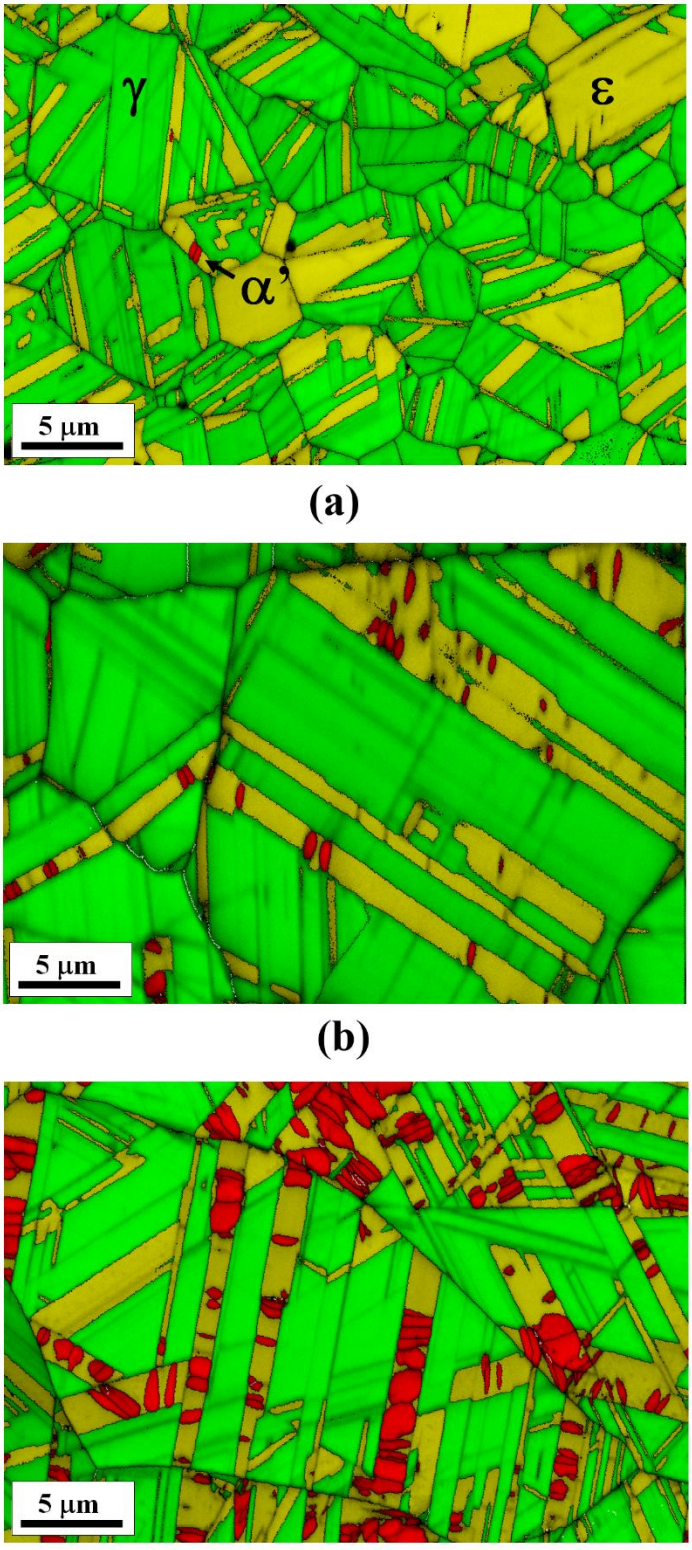

Source: elaborated by the author.

1996; JUN; CHOI, 1998). According to Jiang and co-authors (1995), the athermal formation of ε-martensite in high-Mn steels is related to the presence of stacking faults within austenite. These authors claim that the larger the grain, the higher the probability of stacking faults overlapping, favoring ε-nucleation. Thus, when the intersection of ε-plates becomes important and more frequent, the higher the possibilities of finding α'-nucleation sites as well. In this context, Jun and Choi (1998) proposed a thermodynamic approach to calculate the ε-martensite start temperature (M_s^{ε}) as a function of the stacking fault energy (SFE) for a binary Fe-Mn alloy, as follows:

$$M_S^{\varepsilon}\ (°C) = \left(364.8 + \frac{370.6}{SFE}\right) - 273.15 \qquad (6.1)$$

where SFE is given in mJ/m^2 and can be calculated according to Eq. (3.1).

According to refs. (TAKAKI; NAKATSU; TOKUNAGA, 1993; LI et al., 2018; SAEED-AKBARI et al., 2009; PIERCE et al., 2014), an excess free energy (ΔG_{ex}) arising from grain size is considered to exert an important influence on ε-formation, as experimentally observed in this work. Adopting the procedure reported in ref. (SAEED-

Figure 6.7 - ε-martensite start temperature (M_s^{ε}) as a function of austenite grain size for the 17.6Mn-TRIP steel, calculated using the approach reported by Jun and Choi (1998) and modified by Saeed-Akbari (2009). M_s^{ε} values corresponding to austenite-grain sizes found for both minimum and maximum annealing times at 800ºC (5 min and 120 min) are indicated by arrows.

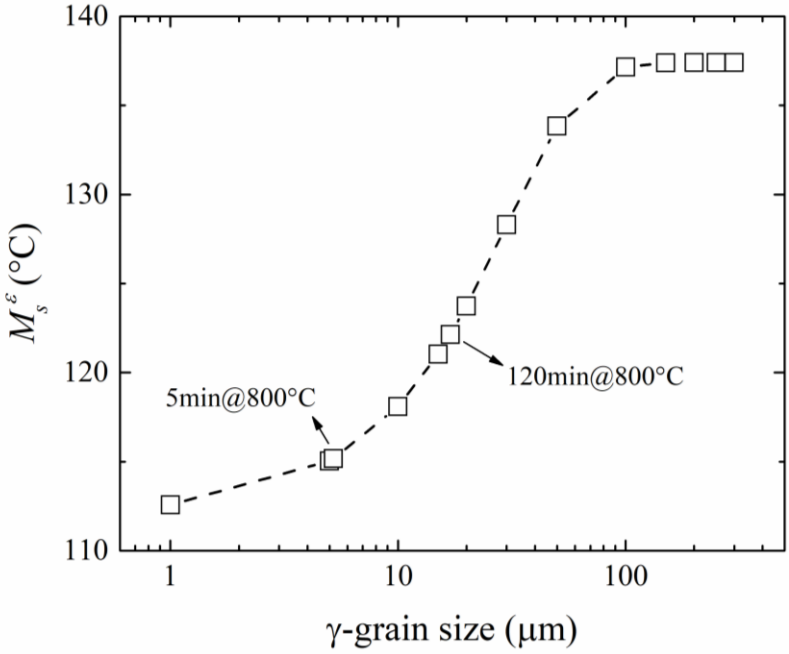

Source: elaborated by the author.

AKBARI et al., 2009), an excess free energy (ΔG_{ex}) arising from grain size can be added to Eq. (6.1), as follows:

$$M_S^{\varepsilon}\ (°C) = \left(364.8 + \frac{370.6}{\left[SFE + 2.\rho.170.06\exp\left(\frac{-d}{18.55}\right)\right]}\right) - 273.15 \quad (6.2)$$

where d is the mean austenite grain size, given in μm. ρ is the molar surface density along the {111} planes of austenite (see Section 3.1).

The SFE of the present steel is ~ 8.1 mJ/m^2 (Chapter 3). Using this value and Eq. (6.2), the obtained values of M_s^{ε} were plotted as a function of the austenite grain size in Fig. 6.7. In this figure, the calculated M_s^{ε} (°C) values corresponding to γ-grain sizes found for both minimum and maximum annealing times at 800°C (5 min and 120 min) are highlighted. It was found no drastic changes in the calculated M_s^{ε} values for the entire range of austenite grain size. In all cases, however, M_s^{ε} is always higher than $M_s^{\alpha'}$ values found from M(T) curves displayed in Fig. 6.4 (a), confirming that athermal α' is dependent on the presence of prior ε-martensite for this steel. Based on these observations and in light of refs. (TAKAKI; NAKATSU; TOKUNAGA, 1993; JIANG et al., 1995; JIANG et al., 1996; JUN; CHOI, 1998), it can be concluded that the larger the grain size the higher the possibility of occurring ε-martensite intersections, favoring α'-martensite formation and shifting $M_s^{\alpha'}$ to higher values (ALLAIN et al., 2004).

6.3 Summary and conclusions

Strain-induced martensite formation, austenite reversion and athermal martensitic transformation in cold-rolled 17.6Mn-TRIP steel were investigated. The following conclusions can be drawn:

i) At a strain of ε = 0.22, α'-martensite is found interspersed within the matrix. In terms of magnetic properties, such microstructural configuration displayed the maximum H_c. For larger strains, H_c decreased as a consequence of the coalescence of α'-martensite grains. Therefore, strong magnetic shape anisotropy was observed to determine the coercivity of this steel.

ii) Austenite reversion during isothermal annealing presented an annealing time-dependence at 500 and 600°C, evidencing a long-range diffusional mechanism. Within this temperature range, austenite formation fragmented the prior cold-rolled α'-martensite structure. As a

consequence, strong magnetic shape anisotropy lead to high values of H_c. In the early stages of austenite reversion, the formation of austenite nanograins was sufficient to strongly increase the coercivity of the investigated steel. For $T_{annealing} \geq 700°C$, however, austenite reversion was complete after 5 min.

iv) After complete austenite reversion at 800°C, athermal α'-formation (with the presence of prior athermal ε-martensite) was observed for temperatures below 100°C. For 30, 45 and 60 min of annealing at 800°C, the start α'-martensite temperature ($M_s^{\alpha'}$) was observed to be nearly the same (~ 70°C). However, 120 min of annealing at 800°C shifted the $M_s^{\alpha'}$ to 95°C. Austenite grain growth with increasing annealing time was clearly observed by means of EBSD analyses. For 5, 30, and 120 min, austenite grains were found to be subdivided by ε-plates. Intersection of ε-plates were observed to be more prevalent at 120 min. Nevertheless, in all evaluated cases, athermal α'-martensite was only found within ε-martensite. Using a thermodynamics approach, the M_s^{ε} values were also calculated. Results showed that ε-martensite was always expected to be formed before α'-martensite, corroborating the observations made via EBSD and *in-situ* magnetic measurements. Therefore, it was concluded that the larger the austenite grain size, the higher the possibility of ε-martensite intersections, favoring α'-martensite formation.

Chapter 7

Revealing the anomalous increase in magnetization of α'-martensite at low temperatures

7.1 Introduction

In the previous Chapter, it was observed that isothermal annealing at 350°C promoted the increase in the magnetization of the 80% cold-rolled high-Mn steel. Similar behavior was already reported for different variants of austenitic stainless steels containing austenite and α'-martensite in conditions of age-annealing at ~ 400°C (GUY; BUTTLER; WEST, 1983; MONTANARI, 1990; GAUZZI et al., 1999; PADILHA; PLAUT; RIOS, 2003; GAUZZI et al., 2006). Over decades, this scenario has been addressed as consequence of an 'anomalous increase of the α'-content'. Some authors suggest that such increase in magnetization is due to static recovery in remaining austenite and stress relief, allowing the adjacent α'-phase to experience further growth (CHUKHLEB; MARTYNOV, 1960; MANGONON JR.; THOMAS, 1970). Another possible explanation is given by the formation of carbides on austenite grain boundaries which leads to the formation of C-depleted regions with higher martensitic starting temperature ($M_s^{\alpha'}$). Thus, under cooling these regions are prone to transform into α'-martensite (CHUKHLEB; MARTYNOV, 1960; HARRIS, 1982). In case of refs. (GUY; BUTTLER; WEST, 1983; MONTANARI, 1990; GAUZZI et al., 1999; GAUZZI et al., 2006) the content of α'-martensite was assessed by means of *ex-situ* measurements including magnetic probing. *In-situ* conventional XRD at 400°C was performed by Gauzzi and co-authors (2006) to investigate the anomalous increase of α'-martensite in an AISI 304 steel. However, for that steel both aging and austenite reversion was reported to be concurrent at 400°C.

Differently from the refs. (CHUKHLEB; MARTYNOV, 1960; MANGONON JR.; THOMAS, 1970; HARRIS, 1982; GUY; BUTTLER; WEST, 1983; MONTANARI, 1990; GAUZZI et al., 1999; PADILHA; PLAUT; RIOS, 2003; GAUZZI et al., 2006), an anomalous magnetization was detected for a high-Mn steel with 17.6 wt.% Mn, mainly composed of α'-martensite and also containing a neglectable fraction of the ε-phase (i.e., cold-rolled to 80%, Fig. 6.2). Therefore, the 'anomalous increase in α'-content' driven by stress relaxation in surrounding austenite seems not to be adequate in the present study. Besides, the possible precipitation of $M_{23}C_6$ was inferred to occur in α' rather than in the γ-

phase in this steel (Fig. 5.9). In light of this observations, the aim of this Chapter is to throw lights onto the raise in magnetization at 350°C and understand the corresponding underlying mechanisms, based on the influence of internal stresses, short-range ordering, and chemical fluctuations on the magnetic properties of high-Mn steels. For this purpose, a systematic investigation was carried out for the steel deformed to 20 and 80% of cold rolling. Detailed data were obtained by means of several probes including *in-situ* and *ex-situ* magnetic measurements. High-resolution X-ray diffraction (XRD) allowed the use of the modified Williamson-Hall method to evaluate the lattice-strain ($\varepsilon_{\text{lattice}}$), as well as the evolution of the coherent domain sizes. Additionally, phase evolution was also assessed by means of XRD. Electron backscatter diffraction (EBSD) and scanning transmission electron microscopy (STEM) were used to investigate detailed microstructural aspects. Localized chemical composition fluctuations were observed via atom probe tomography (APT). All the results were complemented with thermodynamic simulations to obtain information regarding the magnetic contribution of phases (e.g. Bohr magneton and Curie temperature), using the software Thermo-Calc. This study also brings new insights regarding the use of magnetic probing as a tool for phase quantification in magnetic systems and how nano- and sub-micron scaled microstructural changes modify the macro-magnetic properties of a variety of steels.

7.2 Results

7.2.1 In-situ magnetic measurements

The changes in magnetization during continuous annealing were reported in Chapter 5 for the 80% cold rolled steel, as displayed in Fig. 5.2. In this Section, Fig. 5.2 is partially reproduced in terms of the corresponding magnetic moment (m) for the temperature range between 310 and 400°C as shown in Fig. 7.1. In this figure, the magnetic moment of the 80% deformed steel is observed to decrease up to 339°C as a likely consequence of the relaxation of the magnetic elastic constants. Preceding the austenite reversion (A_s = 375°C), however, a slight increase in the magnetic moment is detected for the temperature interval of 339-375°C. At this point, it is important to mention that the detection limit of the VSM used in this experiment is 10^{-4} emu. Therefore, the raise in m observed is far above the imprecision limit and can indeed be attributed to microstructural modifications of the steel, referred to as ‘anomalous increase in magnetization’.

Figure 7.1 - Changes of the magnetic moment of the 80% cold rolled high-Mn steel tracked during *in-situ* magnetic measurement. The complete M *x* T curve is displayed in Fig. 5.2.

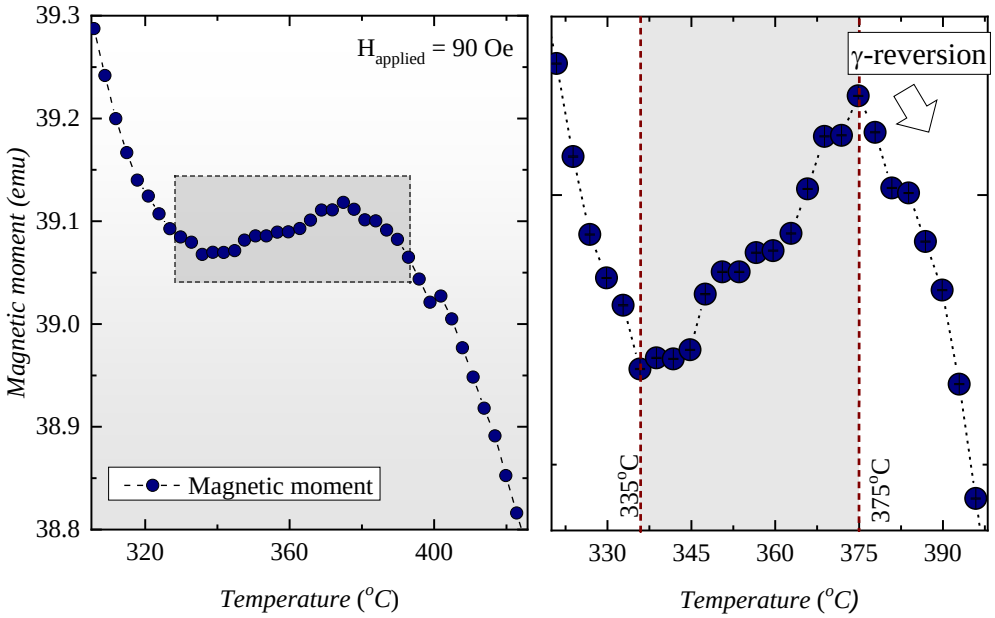

Source: elaborated by the author.

7.2.2 Ex-situ magnetic measurements

In light of the short temperature interval where the anomalous increase in magnetization was observed in Fig. 7.1, isothermal annealings at 350°C (5-120 min) were conducted for the steel deformed to 20 and 80% of thickness reduction. The phase fraction of austenite, ε-, and α'-martensite at 20% is 0.40, 0.20, and 0.40, respectively (Fig. 4.1). Contrastingly, at 80% the microstructure is mainly composed of α'-martensite and only a negligible amount of ε-martensite was observed in EBSD analysis (Fig. 4.8). The purpose of reproducing the same conditions of annealing for two distinct levels of strain is to understand the effects of different internal stresses and phase fractions on the magnetic properties of the steel.

After annealing, hysteresis loops were acquired at room temperature for each sample (not shown) and provided the corresponding behavior of M_s in function of annealing time, as displayed in Fig. 7.2. From this figure, it is evident that the deformation level exerts a minor influence on the shape of both curves, allowing to distinguish four stages as also indicated in Fig. 7.2. In the first stage, M_s increases with 5 min annealing and remains nearly unchanged after 15 min. The plateaus observed between 5 and 15 min are 6.2 and 4.9 emu/g higher than the corresponding starting M_s values at 20 and 80% (referred to as $|\Delta M_s|$ in Fig. 7.2), respectively. Upon the second stage, M_s drops similarly in ~ 4 emu/g in both conditions

Figure 7.2 - Kinetics of the changes in M_s values during isothermal conditions of annealing at 350°C for the high-Mn steel deformed to 20 % (blue squares) and 80% (red squares).

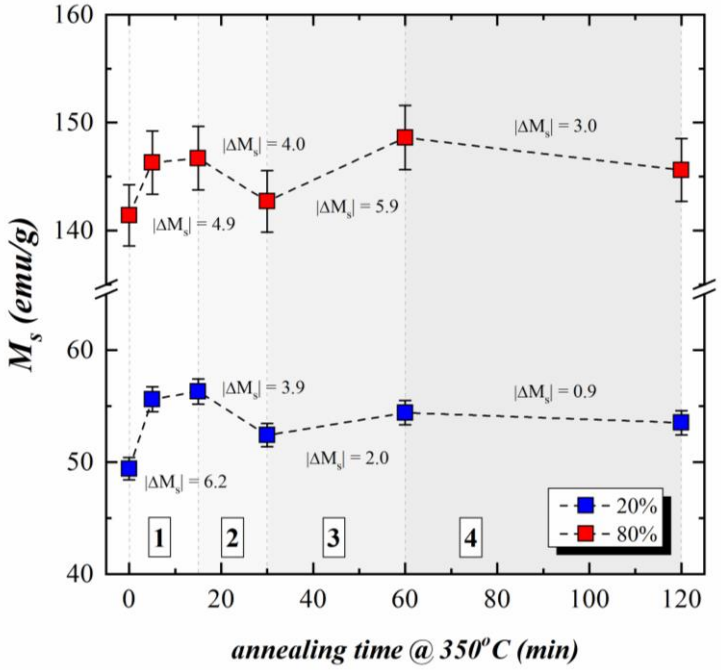

Source: elaborated by the author.

but raises again after 60 min, characterizing the third stage. The magnitude of such increase is about three times higher for the steel deformed to 80%. Finally, the fourth stage is represented by a further decrease in magnetization whose drop is also observed to be three times higher for the 80%-deformed steel. By tracking the evolution of α'-martensite in an AISI 304 steel during isothermal annealings at 400°C, Montanari (1990) reported that the fraction of the α'-phase evolves with fluctuation-shaped curves similar to the M_s curves displayed in Fig. 7.2. However, in the present work the values of M_s is not totally related to the fraction of α'-martensite but directly linked to stress-relief, short-range ordering, chemical fluctuations, and elemental segregation, as it will be demonstrated in the following sections.

7.2.3 Metallographic inspection

Figure 7.3 shows the microstructural evolution of the 20%-deformed steel upon annealing at 350°C, assessed by means of EBSD phase maps. In this figure, austenite, ε-, and α'-martensite are represented by green, yellow, and red, respectively. Previously, Fig. 7.2 revealed that the magnetic behavior of the α'-phase possesses nearly the same kinetics independently on the strain level (i.e. independently on the α'-phase fraction). For this reason and aiming at obtaining detailed data regarding all phases, EBSD analysis was only

Figure 7.3 - Microstructural evolution of the **(a)** 20%-deformed steel annealed at 350°C for **(b)** 15 min; **(c)** 30 min; **(d)** 60 min and **(e)** 120 min. Microstructures observed with the aid of EBSD phase maps where austenite, ε-, and α'-martensite are represented by green, yellow, and red, respectively.

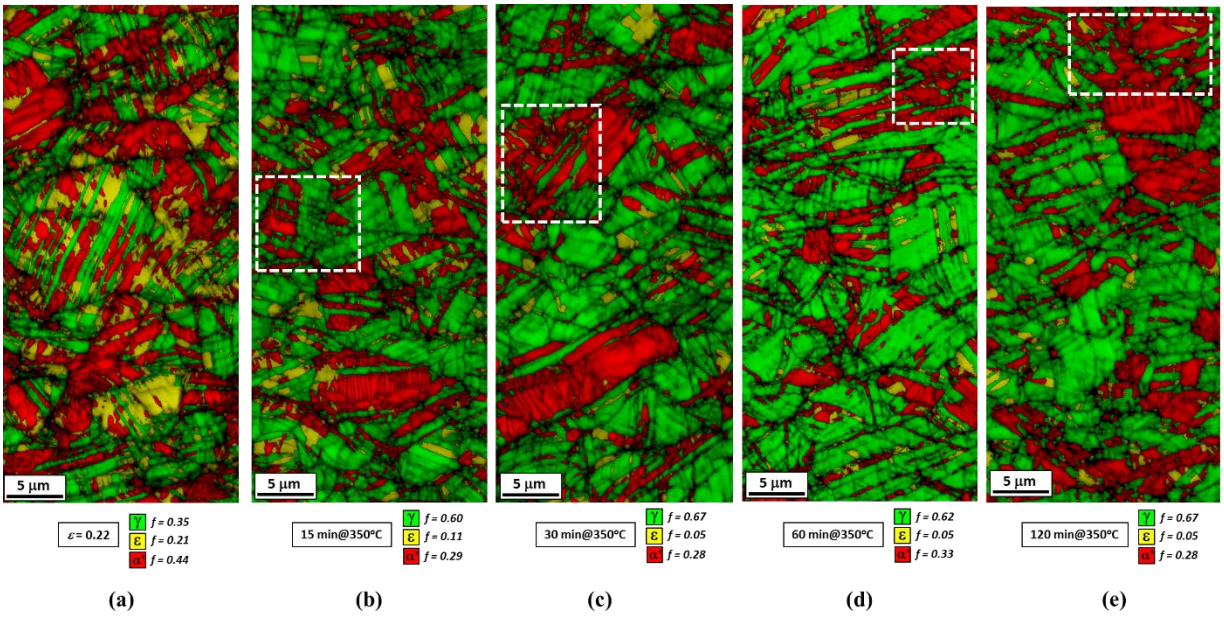

Source: elaborated by the author.

conducted for the steel deformed to 20% of rolling. Fig. 7.3 (a) partially reproduces the microstructure of the 20%-deformed steel, as already discussed in Chapter 4. From Fig. 7.3 (b), 15 min of annealing is sufficient to reduce the fraction of the ε-martensite to 0.11, suggesting that the $\varepsilon \rightarrow \gamma$ reaction is mainly controlled by a shear mechanism. Longer times of exposure at 350°C (Fig. 7.3 c) drop the ε-content to ~0.05 and no further transformation is observed up to 120 min (Fig. 7.3e). In Fig. 7.3, no significant changes in morphology are observed in α'-grains, however, ultra-fine austenite regions can be distinguished immersed within α'-martensite, as clearly evidenced by the dashed frames. Since such configuration is seldomly observed in the deformed state, due to the fact that ε-martensite intermediates the α'-formation, it is plausible to assume that these ultra-fine γ-regions replace the prior ε-plates, i.e. constituting of fresh reversed γ.

7.2.4 X-ray diffraction analysis

7.2.4.1 Phase quantification

Based on the coexistence of approximately identical fractions of γ- and α'-phases at 20% (Fig. 4.1) and on the similar evolution of magnetization for 20% and 80% (Fig. 7.2), high-resolution X-ray diffraction measurements (XRD) were only conducted for the steel deformed to 20% and isothermally annealed at 350°C. For such analysis, the ε-martensite

Figure 7.4 - Phase fraction evolution in the 20%-deformed steel during isothermal annealing at 350°C, calculated from the XRD data.

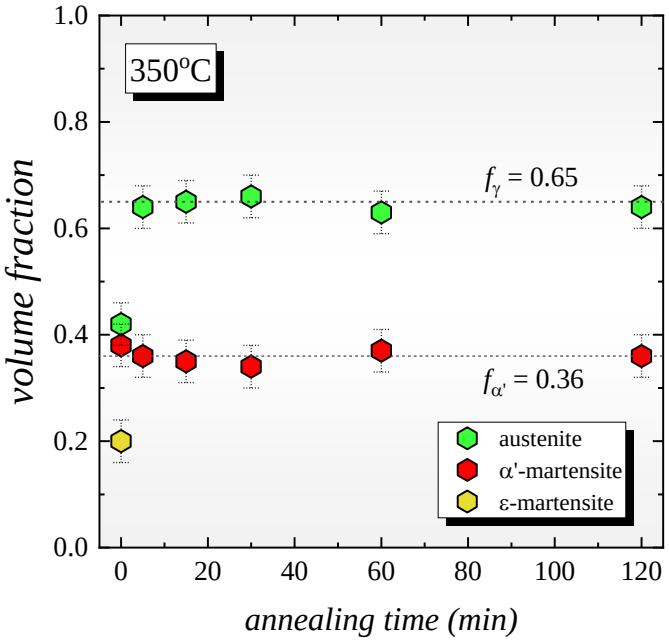

Source: elaborated by the author.

peaks presented low diffraction intensity and therefore were excluded from the calculations. Nevertheless, the very small peaks of ε-martensite confirm its presence in the evaluated samples as previously observed via EBSD. Fig. 7.4 shows the evolution of the γ- and α'-fractions as function of the annealing time and does not reveal substantial modifications in terms of the α'-martensite fraction. In fact, these values remain nearly constant in ~ 0.36 up to 120 min of annealing. Only the massive transformation of ε-martensite into austenite ($\varepsilon \rightarrow \gamma$) in the early 5 min of annealing is noticed in Fig. 7.4. These results evidence that the changes in the M_s values observed in Fig. 7.2 is not completely related to an anomalous increase of α'-martensite caused by stress relief in austenite.

7.2.4.2 Modified Williamson Hall

In this Chapter, the modified Williamson Hall method was employed to evaluate the evolution of lattice strain ($\varepsilon_{\text{lattice}}$) and coherent domains for the 20%-deformed steel. Based on Eq. (2.10), Fig. 7.5 shows the modified Williamson-Hall plots of austenite and α'-martensite for representative conditions of annealing at 350°C. From these plots it was obtained the $\varepsilon_{\text{lattice}}$ parameter and the coherent domain sizes (D), as displayed in Fig. 7.6 (a) and (b) respectively. Fig. 7.6 (a) reveals that the values of $\varepsilon_{\text{lattice}}$ in the α'-phase sharply drops in the early 30 min of annealing and tends to saturate for longer times. This result is a

Figure 7.5 - Modified Williamson-Hall plots for **(a)** austenite and **(b)** α'-martensite from the 20%-deformed steel isothermally annealed at 350°C.

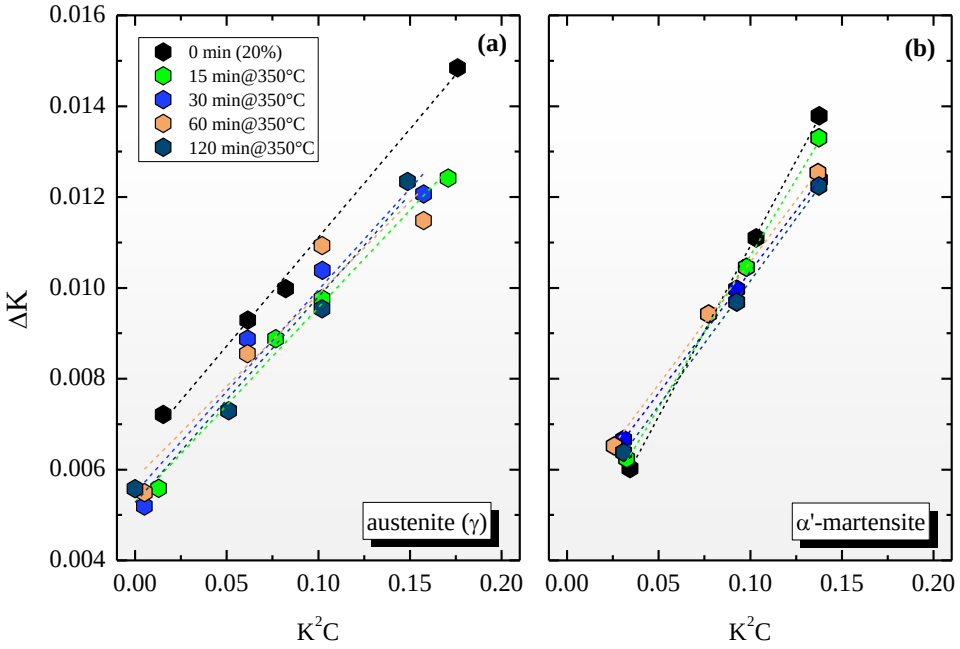

Source: elaborated by the author.

Figure 7.6 - Evolution of the **(a)** lattice strain and **(b)** coherent domain size of the austenite and α'-martensite deformed to 20% and isothermally annealed at 350°C.

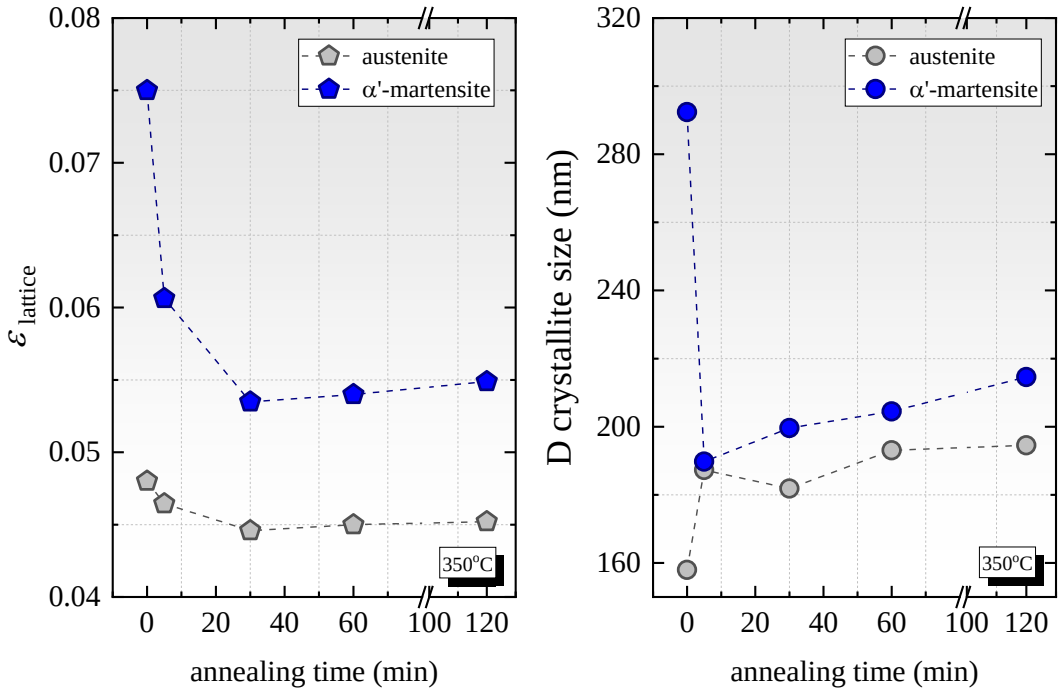

Source: elaborated by the author.

strong evidence that recovery takes place in α'-martensite leading to stress relief. Regarding austenite in Fig. 7.6 (a), its lattice strain slightly decreases with 30 min of annealing (i.e. stress relief) and no significant changes are observed for prolongated annealing times.

The coherent domain sizes in α'- martensite (Fig 7.6b) considerably decreases up to 5 min of annealing, clearly displaying an anomalous behavior since the coalescence of the existing domains is expected to occur driven by diffusional processes upon annealing (e.g. recovery). In light of this observation and due to the relative short annealing time of 5 min, it is plausible to assume that such further fragmentation of α'-martensite is a likely consequence of short-range diffusional processes (viz. short-range ordering). For longer times, D slightly increases up to 120 min, under the expected behavior. The coherent domain size in austenite, in turn, increases with 5 min of annealing and remains nearly constant for longer times.

7.2.4.3 Lattice parameters

Figure 7.7 shows the evolution of the lattice parameter of both austenite and α'-martensite during isothermal annealing at 350°C. Fig. 7.7 (a) reveals that the lattice parameter of austenite remarkably increases after 5 min of annealing, indicating lattice relaxation due to stress relief. For longer times, however, no significant changes are notice. With regard to α'-martensite (Fig. 7.7b), its lattice parameter evolves during annealing with the same trend displayed by the M_s values (Fig. 7.2). From Fig. 7.7 (b), the lattice parameter of the α'-martensite expands as a likely consequence of stress relief in the early 15 min of annealing (stage 1). Contrastingly, a contraction event is observed after 30 min, which

Figure 7.7 - Evolution of the lattice parameter of **(a)** austenite and **(b)** α'-martensite with the progress of the isothermal annealing at 350°C.

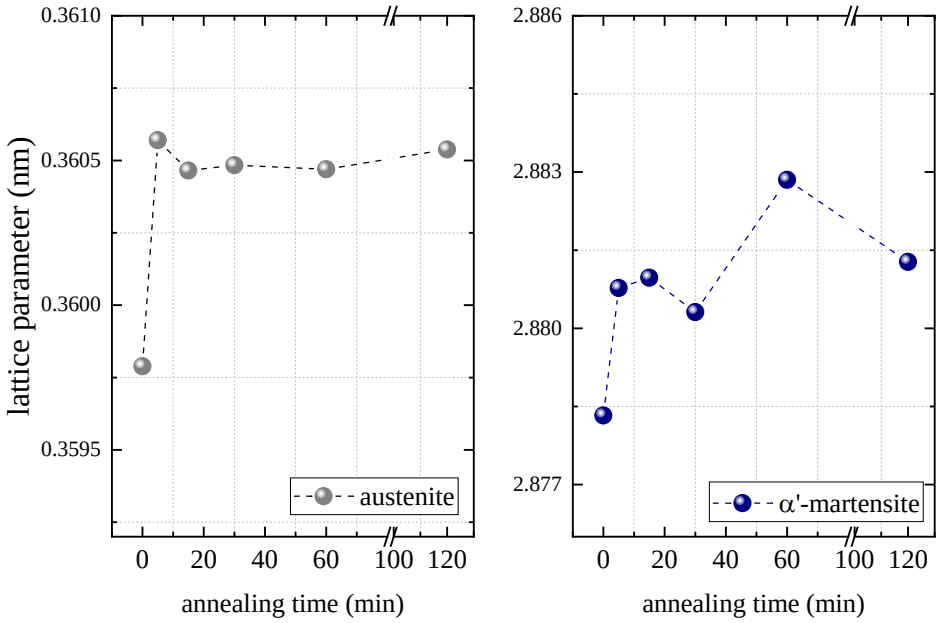

Source: elaborated by the author.

coincides with a decrease in M_s (stage 2). A pronounced peak in the lattice parameter is observed after 60 min (stage 3) and it is followed by a subsequent drop with 120 min of annealing (stage 4).

7.2.5 Thermodynamic simulations

In order to better understand the linkage between the magnetization of α'-martensite and its chemical composition, thermodynamic simulations were conducted using the software Thermo-Calc coupled with the database TCFE9. The magnetization of a specimen is closely related to its fraction of ferromagnetic phases and their corresponding chemical composition. Since no clear transformation of α'-martensite (i.e. modifications in its volume fraction) was previously detected by means of XRD analysis and metallographic inspection, it is plausible to assume that the fluctuations in magnetization observed in Fig. 7.2 are mainly driven by local changes in its composition. Therefore, the possible decomposition of the α'-bcc phase into other bcc regions with different chemical compositions was assessed for a low temperature range preceding the austenite reversion, i.e. between 100 and 360°C. For such purpose, the martensite of the present steel was treated as a disordered α-bcc phase and set in the calculations with the global chemical composition of the steel (Table 2.1). The equilibrium conditions between different bcc regions were then obtained as depicted in Fig. 7.8. For the investigated temperature interval, it is noticed the coexistence of three regions, namely, an intermetallic with stoichiometry of $Ni_5Al_3Mn_2$ and two α-bcc regions, one comprising of a Fe-enriched bcc (bcc^{Fe}) while the other is a Mn-enriched bcc type (bcc^{Mn}). For the long terms of the equilibrium at 350°C, the predicted volume fractions of these phases are 0.015, 0.17, and 0.80, respectively. The magnetic contribution of the distinct bcc regions was assessed in terms of the number of Bohr magneton (μ) and Curie temperature (T_{Curie}), calculated according to the following equations (CHUANG et al., 1986; HUANG, 1989; LACAZE; SUNDMAN, 1990; XINGJUN; SHIMING, 1993):

$$\mu^{bcc} = 2.216x_{Fe} - 5.562x_{Ni} + [10.26 + 0.881(\cdot\, x_{Ni} - \cdot\, x_{Fe})]x_{Ni}x_{Fe} \qquad (7.1)$$

$$T_{Curie}^{bcc} = 1043x_{Fe} - 1747x_{Al} - 580x_{Mn} - 2235x_{Ni} + 123x_{Mn}x_{Fe} + 2820x_{Al}x_{Fe} + 504x_{Fe}x_{Si}(x_{Fe} - x_{Si}) + [3630 + 1096(\cdot\, x_{Ni} - \cdot\, x_{Fe})]x_{Ni}x_{Fe} \qquad (7.2)$$

where, x_i represents the molar fraction of the element *"i"*.

Figure 7.8 - Decomposition of the α-bcc phase into three different bcc regions: $Ni_5Al_3Mn_2$ intermetallic, Fe-enriched bcc (bcc^{Fe}), and Mn-enriched bcc (bcc^{Mn}), predicted with the aid of the software Thermo-Calc for low temperatures.

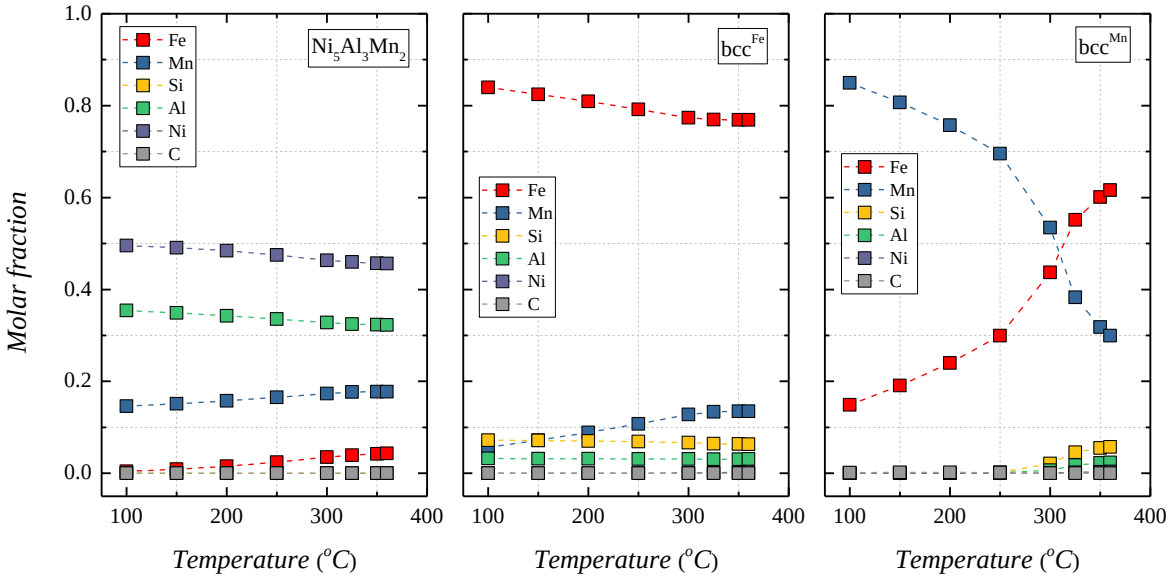

Source: elaborated by the author.

For the given temperature of 350°C, the calculated values of μ for the regions $Ni_5Al_3Mn_2$, bcc^{Fe}, and bcc^{Mn} are respectively 0.37, 1.67, and 1.23. By comparing these values with the one obtained for the disordered bcc ($\mu^{disordered}$ =1.57), it is clearly seen that the decomposition of the bcc phase is prone to create, to some extent, regions with higher magnetic contributions when compared to the starting disordered state. With regard to the T_{Curie}, the corresponding values for $Ni_5Al_3Mn_2$, bcc^{Fe}, and bcc^{Mn} are -79, 565, and 270°C, respectively. Therefore, during the *in-situ* magnetic measurements (Fig. 7.1) the increase in magnetization can be attributed to the formation of Fe-enriched zones, which is ferromagnetic at 350°C and at the same present higher contribution to the overall magnetization when compared to the starting disordered bcc. Although these results are predicted for equilibrium conditions, they bring new insights on the role of local chemical compositions changes to the magnetization of Mn-based steels.

7.2.6 Atom probe tomography (APT)

Representative samples from the steel deformed to 80% and isothermally annealed at 350°C were subjected to APT measurements in order to evaluate local changes in chemical composition and their interplay with the fluctuations of M_s values reported in Fig. 7.2. Since the overall shape of the curves "M_s *vs* annealing time" is practically the same for both, the 20 and 80% conditions, and for ensuring a homogenous extraction of regions containing

only α'-martensite, APT measurement was performed for specimens obtained from the 80% steel.

7.2.6.1 Specimen isothermally annealed at 350°C for 60 min

Figure 7.9 (a) shows the three-dimensional reconstruction of the specimen deformed to 80% and annealed at 350°C for 60 min. In this figure, iso-composition surfaces for Mn (yellow) are constructed with a threshold value of 19 at. % and reveal the existence of Mn-segregation to crystallographic defects. The heterogenous precipitation of Ni-enriched nanoparticles is revealed by means of iso-compositions surfaces (green) with a 5 at. % threshold, as evidenced by the red frame in the enlarged view given in Fig. 7.9 (b). By using the proxygram procedure, the stoichiometry of these nanoparticles is sufficiently estimated as $NiAlMn_2$, as demonstrated in Fig. 7.9 (c). The average composition of the matrix, excluding those regions with Mn-segregation, in terms of Mn, Al, Si, and Ni is 15.9, 1.4, 3.6, and 0.7 at. %, respectively. However, a better evaluation of the elemental partitioning between matrix and segregated regions is enabled by the analysis of two-dimensional composition maps as shown in Fig. 7.10.

From the reconstruction specimen shown in Fig. 7.9 (a), a smaller volume was selected and illustrated in Fig. 7.10 (a), where the Mn-segregation is also evidenced by the iso-composition surfaces (yellow) with the threshold value of 19 at.%. Two-dimensional compositions maps were acquired from the representative region highlighted by the green square with dimensions of 25 x 25 nm^2 in Fig.7.10 (a). In such area, the Mn-segregated surface indicated by the white arrow was used as a reference for this analysis. The composition distributions in terms of Mn, Si, Ni, and Al are displayed in Fig. 7.10 (b-e), respectively. The projection of the Mn-enriched surface pointed out by the white arrow in Fig. 7.10 (a) is also evidenced by arrows in Figs. 7.10 (b-e). From these figures, it is very evident the existence of chemical fluctuations along the microstructure so that elemental segregation to defects (see area pointed out by the arrow) seems to be driven by a spinodal-like decomposition as already demonstrated by binary Fe-Mn alloys annealed at low temperatures (KWIATKOWSKI DA SILVA et al., 2018b). In fact, the chemical fluctuations regarding such decomposition reaches values as high as 30 at. % of Mn and ~ 6.3 at.% of Si on the defects, as indicated by the arrows in Fig. 7.10 (b) and (c). Consequently, adjacent regions depleted in solute are formed displaying compositions of ~ 9 at.% of Mn and ~ 1.5 at. % of Si. Besides, Fig. 7.10 (b) and (c) also reveals that both Mn and Si co-segregate simultaneously to defects. The composition fluctuations in terms of Ni and Al are found

Figure 7.9 - Atom probe tomography measurements for the steel deformed to 80% and isothermally annealed at 350°C for 60 min. **(a)** Three-dimensional reconstruction of the specimen. Iso-compositions surfaces for Mn (yellow) are revealed with the threshold value of 19 at.% of Mn. Iso-compositions for Ni (green) are constructed using 5 at.% as a threshold value. **(b)** Enlarged view of the volume confined by the cylinder in (a). The red frame highlights the presence of Ni-enriched nano-precipitates. **(c)** Proxygram construction for the iso-composition surfaces of 5 at.% of Ni enables to estimate the stoichiometry of the nano-precipitates.

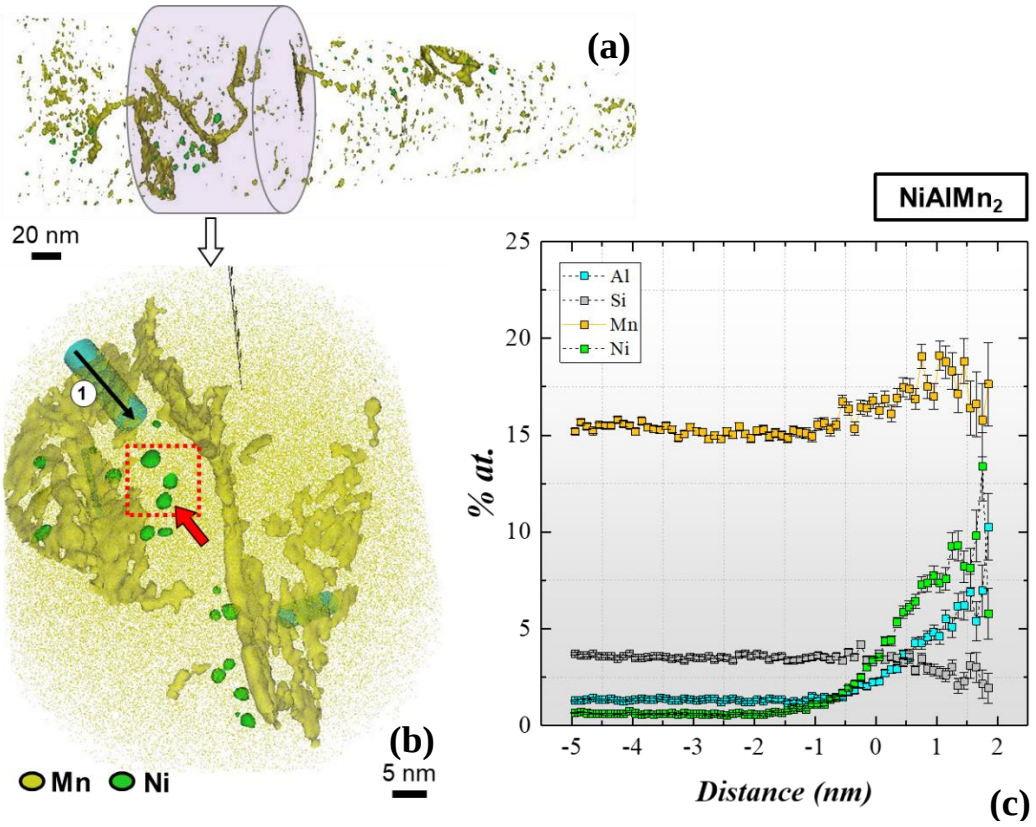

Source: elaborated by the author.

homogenously distributed within the microstructure independently on the presence of crystallographic defects, i.e. no co-segregation of Ni and Al is observed as the one observed for the pair Mn/Si. The presence of very confined clusters enriched in Ni and Al with ~ 2.5 at.% of both elements suggests the heterogenous nano-precipitation of the intermetallic $NiAlMn_2$, as previously observed in Fig. 7.9. At this point, one must also bear in mind the minor instrumental contribution arising from the non-preferential evaporation of Al (MILLER, 1981), which may cause an underestimation of this element in these nano-precipitates, as discussed in Chapter 5.

Figure 7.10 - Atom probe tomography for the specimen deformed to 80% and isothermally annealed at 350°C for 60 min. **(a)** Partial reproduction of the three-dimensional reconstruction displayed in Fig. 7.7 (a). Two-dimensional composition maps were acquired from area delimitated by green square of 25 x 25 nm^2. Two-dimensional composition maps in terms of **(b)** Mn, **(c)** Si, **(d)** Ni, and **(e)** Al. The white arrows indicate the coordinates of the segregated region shown in (a) adopted as reference for this analysis.

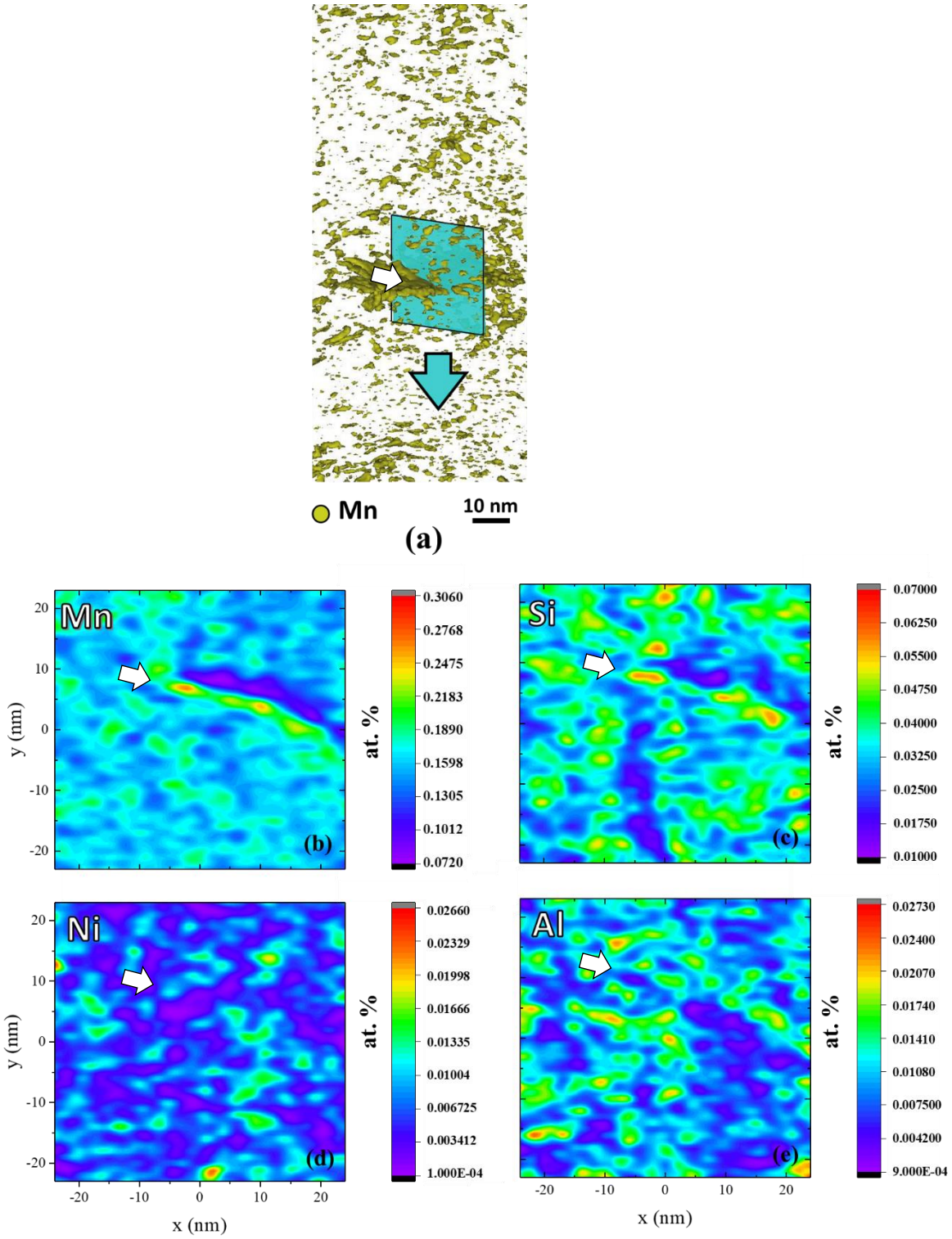

Source: elaborated by the author.

7.2.6.1.1 Magnetic contribution

The chemical compositions obtained from APT measurements and displayed in Fig. 7.10 were also useful to evaluate the magnetic contribution arising from different regions of the α'-martensite annealed at 350°C during 60 min. With the aid of Eqs. (7.1) and (7.2) the chemical distributions shown in Fig. 7.10 were converted into two-dimensional maps for both μ^{bcc} and T_{Curie}, as depicted in Fig. 7.11 (a) and (b), respectively. Fig. 7.11 (a) shows the distribution of the μ^{bcc} parameter within the microstructure and as expected it varies according to the chemical fluctuations driven by the spinodal decomposition. In this figure, the areas limited by the dashed lines present $\mu^{bcc} \leq 1.57$, which is the corresponding value for the disordered starting bcc phase. Fig. 7.11 (a) also reveals that the values of μ^{bcc} are majorly higher than 1.57 and the regions with low magnetic contribution are few and found only within the segregated regions. At the same time, the solute-depleted-zones lying adjacently to the segregated ones are responsible for promoting very high magnetic contributions to the overall response of the specimen, with μ^{bcc} as high as 2.00. The corresponding distribution for T_{Curie} is shown in Fig. 7.11 (b). From this figure, it is possible to see that the segregated zones possess the lowest T_{Curie} values. Some of them are paramagnetic at 350°C and thus during the *in-situ* magnetic measurements do not contribute to the increase in magnetization of the specimen. Therefore, the increase in magnetization

Figure 7.11 - (a) Two-dimensional maps showing the distribution of the number of Bohr magneton (μ^{bcc}) within the steel deformed to 80% and isothermally annealed at 350°C for 60 min. **(b)** Corresponding map for the distribution of the values for the Curie temperature (T_{Curie}).

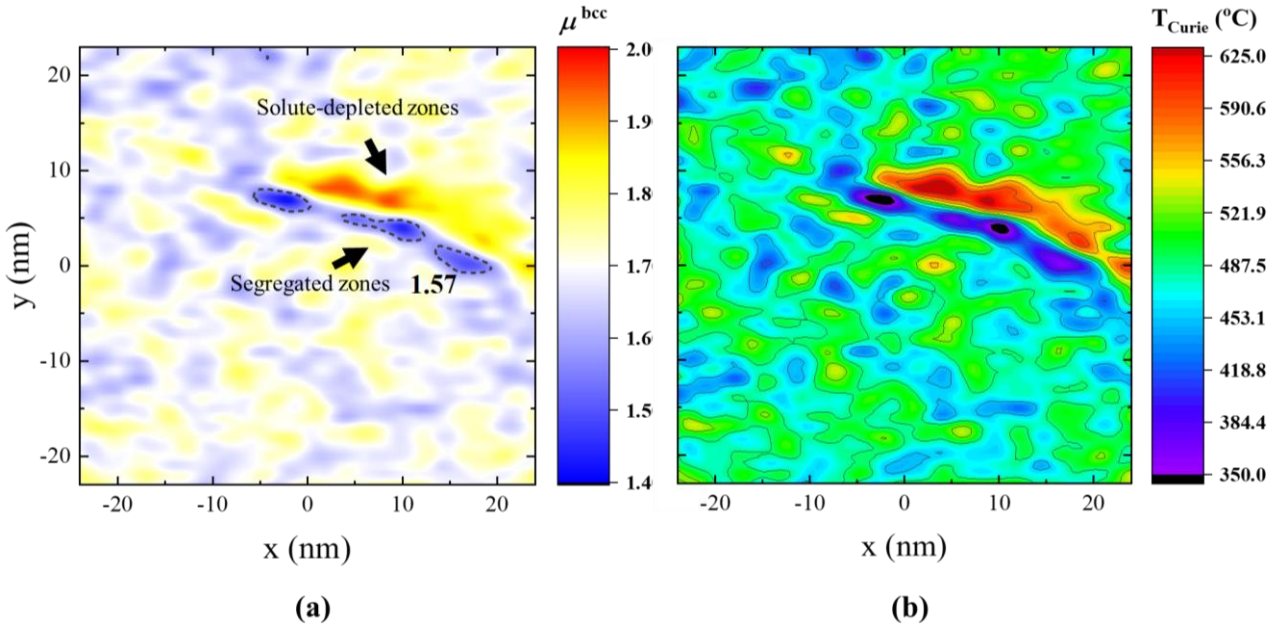

Source: elaborated by the author.

observed not only after 60 min of annealing at 350°C, but also during continuous annealing can be associated to the creation of new solute-depleted zones with high magnetic contribution (i.e., enriched in Fe) driven by chemical fluctuations.

7.2.6.2 Specimen isothermally annealed at 350°C for 120 min

APT measurements were also conducted for the steel deformed to 80% and isothermally annealed at 350°C for 120 min and the results are displayed in Fig. 7.12 (a) for the three-dimensional reconstruction of the APT specimen. In this figure, Mn-segregation is revealed by the iso-composition surfaces (yellow) with the threshold value of 19 at.% of Mn. For the sake of comparison, the size of the specimen displayed in Fig. 7.12 (a) was kept approximately the same as the one reported in Fig. 7.11 (a), for the material annealed during 60 min. By comparing both Fig. 7.11 (a) and Fig. 7.12 (a), it is clear that the volume occupied by Mn-segregation is more pronounced in the specimen annealed for the longer time. Yet, an enlarged view of the likely presence of dislocation loops decorated by Mn is also evidenced in Fig. 7.12 (a) by the blue box. In order to better understand the elemental segregation in this annealing condition, this region was used as a reference for obtaining two-dimensional composition maps, using the same procedure adopted in Section 7.2.6.1.

The two-dimensional composition maps acquired in the cross-section of the tube displayed in Fig. 7.12 (a) are shown in Figs. 7.12 (b-e) in terms of Mn, Si, Ni, and Al, respectively. In Figs 7.12 (b) and (c), Mn and Si fluctuations are also observed to occur driven by spinodal decomposition and compositions as high as ~ 33 at.% of Mn and ~ 7.5 at. % of Si are observed decorating the structure of defects. These values are slightly higher than the ones observed for the material annealed for 60 min. Likewise, Mn and Si also co-segregate to defects leading to the formation of solute-depleted zones adjacently to the segregated ones. The composition of Ni is homogenously distributed within the microstructure and only few confined regions reaches up to ~ 3.7 at. %, indicating the nanoprecipitation. Regarding Al in Fig. 7.12 (e), chemical fluctuations are also observed for this element, as well as few clusters whose composition reaches up to 2.2 at. % of Al.

Figure 7.12 - Atom probe tomography for the specimen deformed to 80% and isothermally annealed at 350°C for 120 min. **(a)** Three-dimensional reconstruction of the APT specimen. Iso-composition surfaces for Mn (yellow) are revealed using a threshold of 19 at.%. The box highlights the presence of dislocation loops decorated by Mn-segregation. Two-dimensional composition maps were acquired from the cross-section of the tube displayed in (a). Two-dimensional composition maps in terms of **(b)** Mn, **(c)** Si, **(d)** Ni, and **(e)** Al.

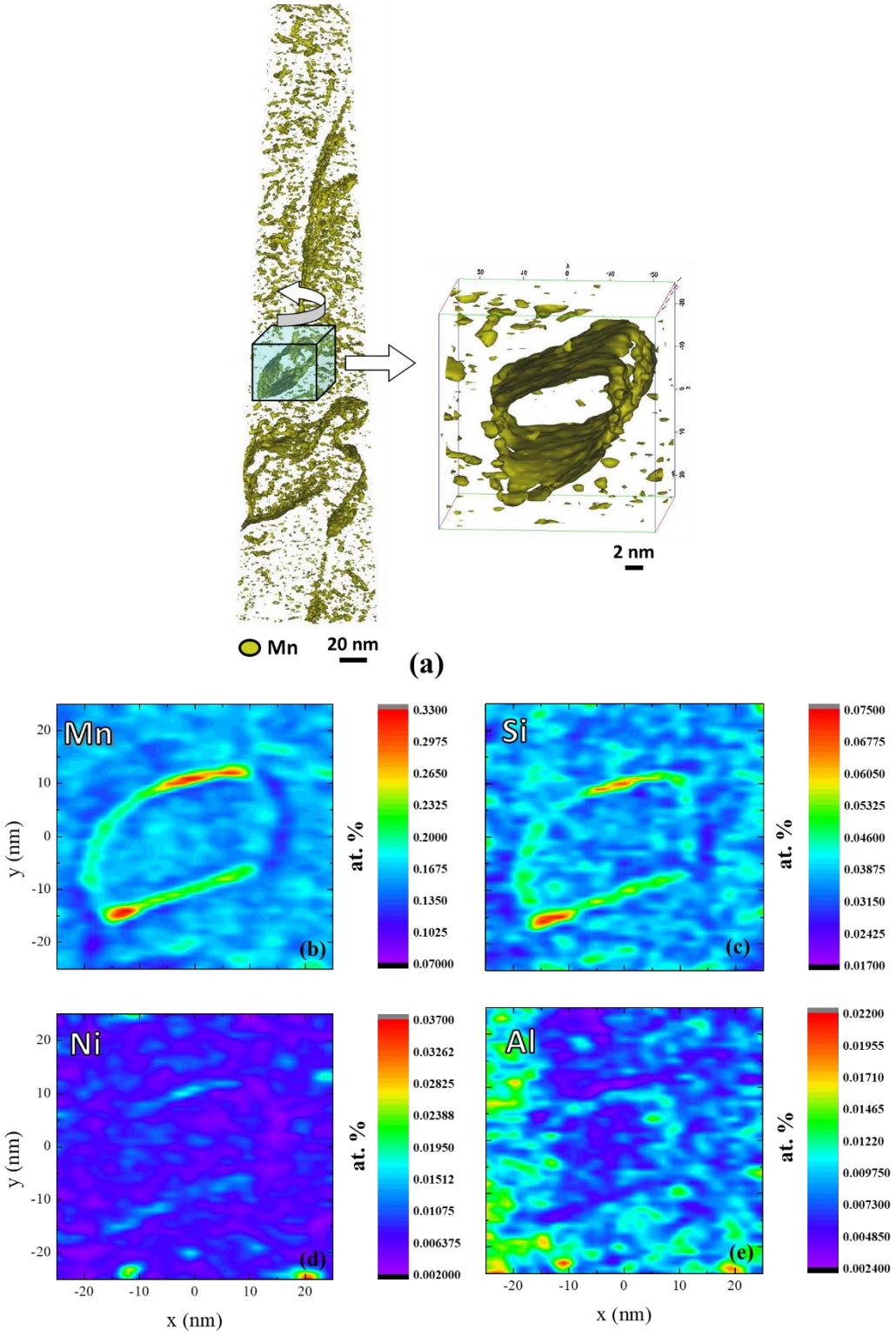

Source: elaborated by the author.

7.2.6.2.2 Magnetic contribution

The chemical compositions displayed in Fig. 7.12 were also converted into μ^{bcc} and T_{Curie} maps as shown in Fig. 7.13. Fig. 7.13 (a) shows the distribution of μ^{bcc} values and reveals fluctuations ranging from 1.57 to 1.85 in the matrix. In this figure, the threshold value of 1.57 observed for the disordered bcc was highlighted by the dashed lines and the corresponding regions possessing $\mu^{bcc} \leq 1.57$ are only found within the segregated zones. With regard to the solute-depleted zones, their maximum value of μ^{bcc} is 1.85. In terms of T_{Curie} (Fig. 7.13b) and as observed for the specimen annealed for 60 min, the segregated regions are paramagnetic at 350°C. However, for 120 min of annealing the paramagnetic volumes seem to extend over a broader volume within the segregated zones, when compared to Fig. 7.11 (b).

Figure 7.13 - (a) Two-dimensional maps showing the distribution of the number of Bohr magneton (μ^{bcc}) within the steel deformed to 80% and isothermally annealed at 350°C for 120 min. **(b)** Corresponding map for the distribution of the values for the Curie temperature (T_{Curie}).

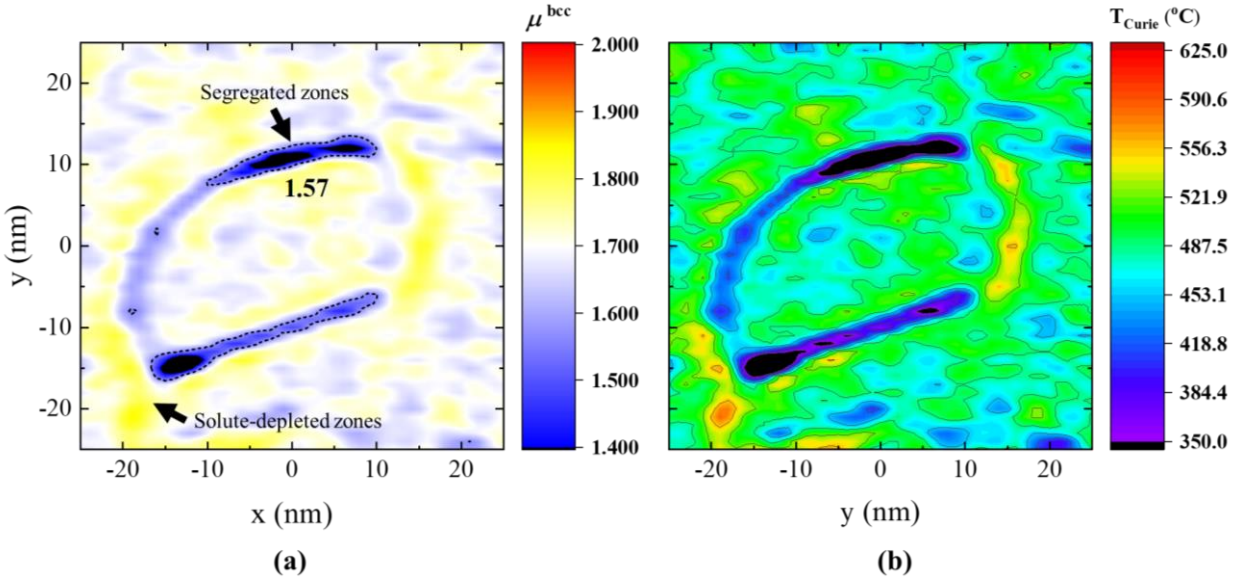

Source: elaborated by the author.

7.3 Discussion

In this study, a systematic microstructural characterization was conducted to reveal the underlying mechanisms responsible for the fluctuations of M_S values displayed in Fig. 7.2. Three premises were used as basis since the classical 'anomalous increase in α'-content' seems not to be entirely adequate in the present investigation. In the following sections, the fluctuations of M_S identified in Fig. 7.2 are discussed separately according to their corresponding stage.

7.3.1 Stage 1

Considering the stage 1 in Fig.7.2, both, the low temperature and the short annealing time would not be sufficient to promote significant long-range diffusional reactions in the specimens. Additionally, phase quantification performed via XRD measurements and metallographic inspections conducted using EBSD revealed the absence of pronounced phase transformation for the ferromagnetic α'-martensite. In other words, the formation of newly fresh α'-martensite was not observed during annealing at 350°C for all investigated annealing times. Thus, this observation impairs the use of the premise "anomalous increase in α'-content allowed by stress relief in neighbor austenite" as the explanation of the increase in magnetization.

Martensitic transformation in metastable austenite is accompanied by lattice distortion and creation of strong internal stress fields. Therefore, the influence of magneto-elastic effects on the magnetic properties cannot be neglected in studies of Mn-based alloys containing the ferromagnetic α'-phase. The magnetic behavior of polycrystalline iron under stress has been reported to be complex. However, it was already demonstrated in ref. (CULLITY; GRAHAM, 2009) that stress raises the M *x* H curve of iron at low applied magnetic fields. Contrastingly, for high magnetic fields, the effects of stress are the

Figure 7.14 - Hysteresis loops (M *x* H curves) for the high-Mn steel deformed to 80% (yellow curve) and subsequently annealed at 350°C for 5 min (blue curve). The crossover of these curves is given at H = 0.95 kOe evidencing the Villari reversal.

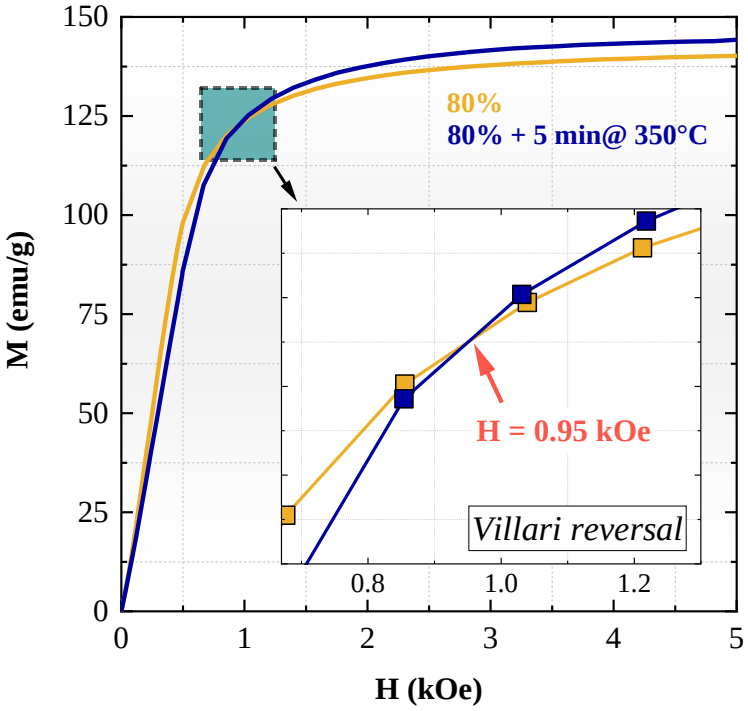

Source: elaborated by the author.

opposite, lowering the M *x* H curves. Therefore, when considering the hysteresis loops for two specimens of the same Fe-based alloy, one deformed (stressed) and the other absent of stress (i.e., annealed), it would be observed at some point the crossover of the curves for a specific field. Such effect is known as Villari reversal and it is reproduced in the present study as reported in Fig. 7.14. In this figure, the early stages of magnetization in the M *x* H hysteresis loops are plotted for the steel deformed to 80% and for the one shortly annealed at 350°C (5 min). Here, it is important to mention that the dimensions of the samples were kept approximately the same (Section 2.3.3) in order to minimize the demagnetizing effects. Results from Fig. 7.14 clearly show the influence of internal stress on the magnetic properties of the cold-rolled α'-martensite and for this case the Villari reversal effect is observed at H = 0.95 kOe. Modified Williamson Hall plots also confirmed the occurrence of recovery in α'-martensite after 5 min of annealing (Fig. 7.6). Therefore, in light of this discussion the most plausible effect ruling the increase of M_s after short annealing times at 350°C (up to 15 min), i.e. stage 1 in Fig. 7.2, is the relaxation of the magneto-elastic constants promoted by stress relief in α'-martensite.

7.3.2 Stage 2

In Fig. 7.2, the M_s values were observed to decrease after 30 min of annealing at 350°C (stage 2). At a first moment, one can attribute to this behavior the precipitation of secondary phases with paramagnetic character. To check this, further metallographic inspection was carried out for the steel deformed to 80% and isothermally annealed at 350°C for 30 min. For this purpose, high-angular annular dark-field imaging (HAADF) was conducted using a scanning transmission electron microscope (STEM). The obtained results are shown in Fig. 7.15 for two distinct regions of the specimen, labeled as #1 and #2. Both regions were observed under the mode HAADF in Figs. 7.15 (a) and (d), annular dark field (ADF) in Figs. 7.15 (b) and (e), and annular bright field (ABF) in Figs. 7.15 (c) and (f). In these images, the substructural morphology of the α'-martensite is lath-type with dense dislocation arrangements and no evidences of precipitations were observed, as confirmed by the high-resolution images and corresponding diffraction pattern displayed in Fig. 7.15 (g), obtained from region #2.

From the modified Williamson-Hall analysis, the coherent domain sizes of the α'-martensite decreases up to 5 min of annealing at 350°C, displaying an anomalous behavior since the coalescence of crystallites are expected upon annealing due to diffusional

Figure 7.15 - High-angular annular dark-field imaging (HAADF) of the steel deformed to 80% and isothermally annealed at 350°C for 30 min. The numbers #1 and #2 correspond to two distinct analyzed regions in the sample imaged under the modes HAADF in **(a)** and **(d)**, ADF in **(b)** and **(e)** and ABF in **(c)** and **(f)**. **(g)** high-resolution HAADF images and corresponding diffracted pattern, obtained from region #2.

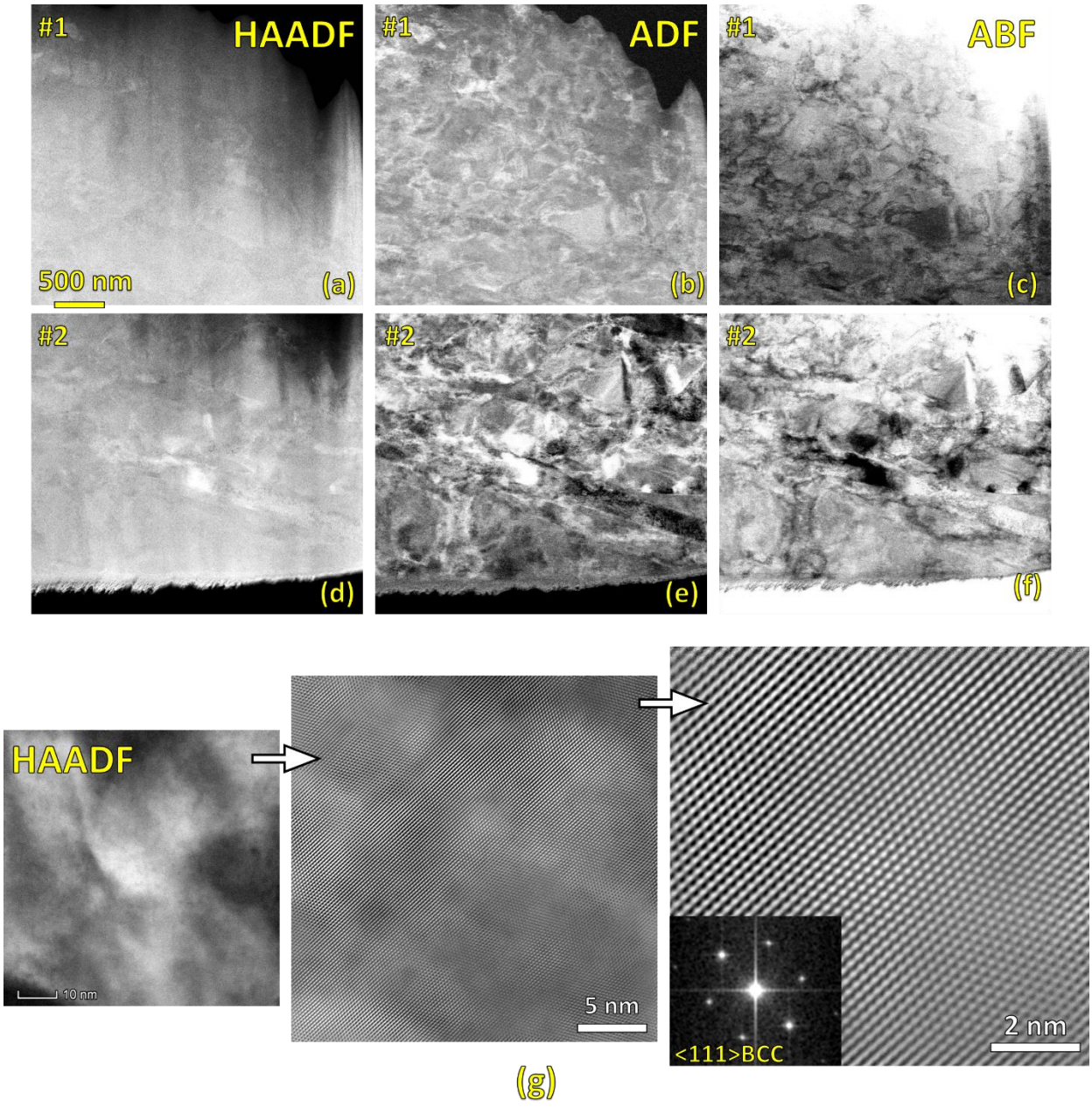

Source: elaborated by the author.

processes. Thus, the further fragmentation of the coherent domains in α'-martensite can be ascribed to reactions of short-range ordering, leading to the creation of new smaller crystallites where certain atoms tend to rearrange mutually in specific configurations, as schematically exemplified in Fig. 7.16. For the binary systems Fe-Al, Fe-Si, and Ni-Mn short-range ordering is well understood and the configurations such as B2-bcc and $D0_3$ emerges as examples of ordering (HUFFMAN; FISHER, 1967; INDEN, 1981; INDEN,

Figure 7.16 - (a) Schematic representation of the starting disordered bcc phase (steel deformed to 80%) with random distribution of atoms within the coherent domain sizes (crystallites). The straight dot lines represent the atomic planes. **(b)** Schematic representation of the same specimen after the formation of ordered crystallites, which leads to the fragmentation of the initial coherent domain sizes.

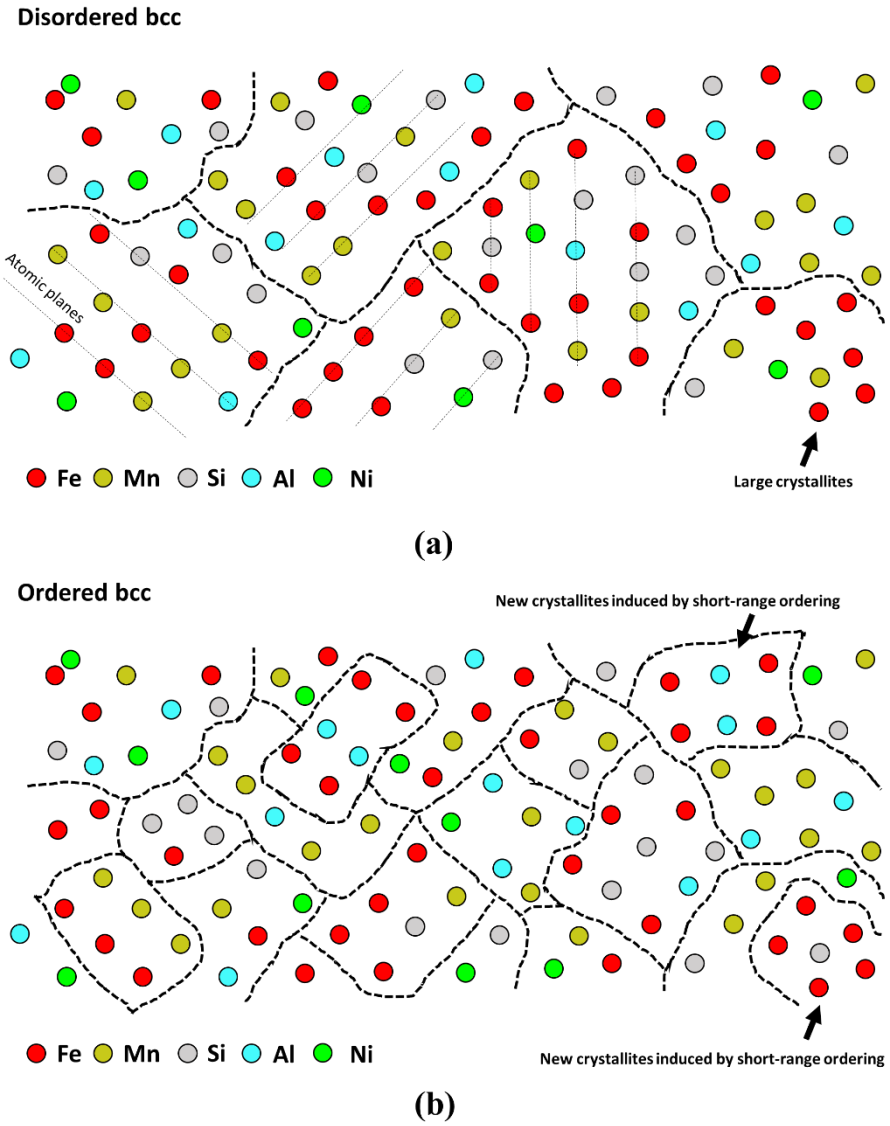

Source: elaborated by the author.

1982; ZENG; BAKER, 2006; ERSHOV et al., 2009; GORBATOV et al., 2011). Such types of configurational structures are reported to decrease the magnetization as reported in ref. (ZENG; BAKER, 2006). When considering the B2-bcc belonging to the Fe-Al system, Al atoms reduce the individual magnetic moments of Fe sites by decreasing the ferromagnetic interaction between Fe-Fe pairs. Additionally, the pair Mn-Mn, for example, is reported to present negligible contributions to magnetization (SMOLUCHOWSKI, 1951).

The transition between the disordered bcc to the ordered B2-bcc is accompanied by a reduction in the lattice parameter of ~ 0.8% (ZENG; BAKER, 2006). In fact, Fig. 7.7

revealed that the lattice parameter of the α'-martensite in the present steel fluctuates with the same trend displayed by the M_s values during the isothermal annealing. Most important, the decrease in M_s observed after 30 min of annealing (Fig. 7.2) occurs concomitantly with a contraction in the α'-martensite lattice parameter (Fig. 7.7), which is in agreement with the statement of ref. (ZENG; BACKER, 2016). Although the character of the short-range ordering reactions occurring in this steel is not clear yet, the above results provide strong evidences that such effect is the main mechanism responsible for dropping M_s to values similar to those ones observed after cold rolling, (stage 2 in Fig. 7.2). Here, it is important to notice that short-range ordering seems not to be predominant in the early stages of annealing (i.e., up to 15 min), where the increase of the M_s values is caused by stress relief in α'-martensite.

7.3.2 Stages 3 and 4

APT measurements revealed the existence of chemical fluctuations driven by spinodal decomposition in the specimens exposed to 350°C during 60 and 120 min. Due to pronounced chemical fluctuations, areas with high values of μ^{bcc} (high magnetic contribution) are created within the α'-phase, especially in the solute-depleted zones found adjacently to the segregated ones. In other words, the early stages of elemental segregation to crystallographic defects act as a cleaning process of the matrix expelling solutes of non-magnetic atoms (e.g. Mn) to defects and leading behind a matrix enriched in Fe. Therefore, these internal chemical changes promote the increase in M_s after 60 min of annealing. For the steel annealed up to 120 min, the APT three-dimensional reconstructed specimens revealed that the number of segregated regions is much higher after 120 min of annealing. Consequently, the number of the zones decorated with non-magnetic atoms increases, as well as its influence on the overall magnetization of the specimen. Thus, M_s tends to decrease with longer times of exposure at 350°C, especially for the 80% deformed steel.

7.4 Summary and conclusions

A systematic investigation was carried out to reveal the underlying mechanisms responsible for increasing the values of M_s in a high-Mn steel deformed to 20 and 80% of rolling. XRD analysis and high-resolution microstructural characterization revealed the absence of further growth of α'-martensite and therefore, the increase in M_s can only be understand in terms of chemical changes within α'-martensite. For isothermal conditions of

annealing at 350°C, short annealings up to 15 min promoted the increase of M_s due to stress relief in α'-martensite. Further annealing to 30 min promotes the decrease in M_s and a contraction in the α'-lattice. These observations were inferred to be driven by short-range ordering reactions, as also suggested by the further subdivision of the α'-martensite into smaller crystallites. Finally, chemical fluctuations are observed after longer times of exposure at 350°C. As a consequence, the segregation of solutes to crystallographic defects enriches the matrix in Fe-content promoting the increase in M_s after 60 min. Further segregation occurs during 120 min so that the raise in number of the zones with low magnetic contributions makes M_s decrease as well. The obtained results clearly show the importance of chemical compositions fluctuations to the magnetic properties of Mn-based alloys. Therefore, the values of M_s must be taken cautiously for phase quantification since it is prone to undergo strong influences from internal stresses and chemical changes.

8. Final Remarks

Since the high-quality performance of Mn-based steels is closely related to microstructural aspects and in order to design high-strength variants of such materials, it is imperative to deeply understand their complex superposition of several strain hardening mechanisms, diffusion-controlled reactions, as well as their influence on mechanical properties. In this work, a systematic characterization of a high-Mn steel containing 17.6 wt. % of Mn and belonging to the Fe-Mn-Al-Si-C-Ni system was conducted for a variety of deformed and annealed conditions. Starting with a fully recrystallized microstructure, the combinatorial use of XRD, ECCI-SEM, and EBSD allowed revealing the occurrence of several displacive and important reactions in γ, ε - and α'-martensite, including the formation of sub-micron structural defects and the martensitic transformation induced by deformation. With regard to the austenite reversion, near-atomic resolution APT combined with thermodynamic and thermo-kinetic simulations, and dilatometry measurements brought new information about the challenging observation of the γ-nucleation in high-Mn steels. This work also contributes to add new evidences to the literature that the successful γ-nucleation events are preceded by strong long-range elemental partitioning, especially in terms of Mn. Besides, the growth of reversed austenite is also controlled by pronounced elemental partitioning and solute redistribution, as revealed by thermo-kinetic simulations and confirmed via APT. Magnetic measurements are considered as one of the most powerful tools for investigating phase transformations in steels. By using *ex-situ* and *in-situ* magnetic measurements, the stability of austenite faced the martensitic transformation upon cooling was studied and the findings of this work confirmed that the ε-martensite is an intermediate phase for α'-formation. Regarding isothermal annealings, the formation of nano reversed γ-grains in the early stages of the austenite reversion is sufficient to induce strong magnetic shape anisotropy. Finally, the strong influence of short and long-range chemical fluctuations on the magnetic properties was studied using APT, high-resolution microscopy, thermodynamic simulations, and magnetic measurements. It was clearly demonstrated that the Mn-based steels variants containing the ferromagnetic α'-martensite are very sensitive to local changes in chemical composition. The results reported in this thesis throw new insights regarding the use of the magnetization saturation as a probe for quantifying ferromagnetic phases in steels.

References

AARONSON, H. I.; ENOMOTO, M.; LEE, J. K. **Mechanisms of Diffusional Phase Transformations in Metals and Alloys**. Boca Raton, FL: CRC Press, 2010.

ADLER, P. H.; OLSON, G. B.; COHEN, M. Strain Hardening of Hadfield Manganese Steel. **Metallurgical Transactions A**, v.17, p.1725-1737, 1986.

ALLAIN, S.; CHATEAU, J.-P.; BOUAZIZ, O.; MIGOT, S.; GUELTON, N. Correlations between the calculated stacking fault energy and the plasticity mechanisms in Fe-Mn-C alloys. **Materials Science and Engineering A**, v.387-389, p.158-162, 2004.

ANAND, K. K.; MAHATO, B.; HAASE, C.; KUMAR, A.; CHOWDHURY, S. G. Correlation of defects density with texture evolution during cold rolling of a Twinning-Induced Plasticity (TWIP) steel. **Materials Science and Engineering A**, v.711, p.69-77, 2018.

BALDO, S.; MÉSZÁROS, I. Effect of cold rolling on microstructure and magnetic properties in a metastable lean duplex stainless steel. **Journal of Materials Science**, v.45, p.5339-5346, 2010.

BERRENBERG, F.; HAASE, C.; BARRALES-MORA, L. A.; MOLODOV, D. A. Enhancement of the strength-ductility combination of twinning-induced/transformation-induced plasticity steels by reversion annealing. **Materials Science and Engineering A**, v.681, p.56–64, 2017.

BORGENSTAM, A.; HÖGLUND, L.; ÅGREN, J.; ENGSTRÖM, A. DICTRA, a tool for simulation of diffusional transformations in alloys. **Journal of Phase Equilibria**, v.21, p.269-280, 2000.

BRACKE, L.; KESTENS, L.; PENNING, J. Transformation mechanism of α'-martensite in an austenitic Fe–Mn–C–N alloy. **Scripta Materialia**, v.57, p.385–388, 2007.

BUNGE, H. **Texture Analysis in Materials Science**, Butterworth, London, 1982.

CALCAGNOTTO, M.; PONGE, D.; DEMIR, E.; RAABE, D. Orientation gradients and geometrically necessary dislocations in ultrafine grained dual-phase steels studied by 2D and 3D EBSD. **Materials Science and Engineering A**, v.527, p.2738-2746, 2010.

CHUANG, Y.-Y.; CHANG, Y. A.; SCHIMD, R.; LIN, J.-C. Magnetic Contributions to the Thermodynamic Functions of Alloys and the Phase Equilibria of Fe-Ni System below 1200 K. **Metallurgical Transactions A**, v.17A, p.1361-1372, 1986.

CHUKLEB, A. N.; MARTYNOV, V. P. Phase Transformations YZ a During the Aging of 1808 Type Steels Previously Deformed at a Negative Temperature. **Physic of Metals and Metallography**, v.10, 1960.

CULLITY, B.D. **Elements of X-ray diffraction**. 2nd.ed. Massachusetts: Addison – Wesley Publishing Company, 1978.

CULLITY, B. D.; GRAHAM, C. D. **Introduction to Magnetic Materials**. 2nd ed. John Wiley and Sons, New Jersey, 2009.

DAFÉ, S. S. F.; SICUPIRA, F. L.; MATOS, F. C. S.; CRUZ, N. S.; MOREIRA, D. R.; SANTOS, D. B. Effect of cooling rate on (ε, α') martensite formation in twinning/transformation-induced plasticity Fe–17Mn–0.06C steel. **Materials Research**, v.16, p.1229-1236, 2013.

DASTUR, P.; ZAREI-HANZAKI, A.; PISHBIN, M. H.; MOALLEMI, M.; ABEDI, H. R. Transformation and twinning induced plasticity in an advanced high Mn austenitic steel processed by martensite reversion treatment. **Materials Science and Engineering A**, v.696, p.511-519, 2017.

DASTUR, P.; ZAREI-HANZAKI, A.; RAHIMI, R.; KLEMM, V.; DE COOMAN, B. C.; MOLA, J. Nanoscale partitioning of Mn between austenite and martensite revealed by Curie temperature variations. **Philosophical Magazine Letters**, 2018.
DOI: 10.1080/09500839.2018.1465238

DE COOMAN, B. C.; CHIN, K. G.; KIM, J. (2011). High Mn TWIP Steels for Automotive Applications, New Trends and Developments in Automotive System Engineering, Prof. Marcello Chiaberge (Ed.), ISBN: 978-953-307-517-4.
Disponível em: http://www.intechopen.com/books/new-trends-anddevelopments-in-automotive-system-engineering/high-mn-twip-steels-for-automotive-applications.
Acesso em: 16 jun. 2019.

DE, A. K.; MURDOCK, D. C.; MATAYA, M. C.; SPEER, J. G.; MATLOCK, D. K. Quantitative measurement of deformation-induced martensite in 304 stainless steel by X-ray diffraction. **Scripta Materialia**, v.50, p. 1445–1449, 2004.

DING, H.; DING, H.; SONG, D.; TANG, Z.; YANG, P. Strain hardening behavior of a TRIP/TWIP steel with 18.8% Mn. **Materials Science and Engineering A**, v.528, p.868–873, 2011.

DINSDALE, A. T. SGTE data for pure elements. **Calphad (Computer Coupling of Phase Diagrams and Thermochemistry)**, v.15, p.317-425, 1991.

DJUROVIC, D.; HALLSTEDT, B.; VON APPEN, J.; DRONSKOWSKI, R. Thermodynamic assessment of the Mn-C system. **Calphad (Computer Coupling of Phase Diagrams and Thermochemistry)**, v.34, p.279-285, 2010.

DJUROVIC, D.; HALLSTEDT, B.; VON APPEN, J.; DRONSKOWSKI, R. Thermodynamic assessment of the Fe-Mn-C system. **Calphad (Computer Coupling of Phase Diagrams and Thermochemistry)**, v.35, p.479-491, 2011.

DMITIREVA, O.; PONGE, D.; INDEN, G.; MÍLLAN, J.; CHOI, P.; SIETSMA, J.; RAABE D. Chemical gradients across phase boundaries between martensite and austenite in steel studied by atom probe tomography and simulation. **Acta Materialia**, v.59, p.364-374, 2011.

DONADILLE, V; VALLE, R.; DERVIN, P.; PENELLE, R. Development of texture and microstructure during cold-rolling and annealing of fcc alloys: example of an austenitic stainless steel. **Acta Metallurgica**, v.37, p.1547-1571, 1989.

ELMASSALAMI, M.; PALATNIK-DE-SOUSA, I.; AREIZA, M. C. L.; REBELLO, J. M. A.; ELZUBAIR, A. On the magnetic anisotropy of superduplex stainless steel. **Journal of Magnetism and Magnetic Materials**, v.323, p.2403-2407, 2011.

ERSHOV, N. V.; KLEINERMAN, N. M.; LUKSHINA, V. A.; PILYUGIN, V. P.; SERIKOV, V. V. Specific Features of the Local Atomic Structure of a Fe–Si Alloy in the α Area of the Phase Diagram. **Physics of the Solid State**, v. 51, pp. 1236-1242, 2009.

ESCOBAR, D. P.; DAFÉ, S. S. F.; VERBEKEN, K.; SANTOS, D. B. Effect of the cold rolling reduction on the microstructural characteristics and mechanical behavior of a 0.06%C–17%Mn TRIP/TWIP steel. **Steel Research International**, v. 86, n. 9999, p. 1-12, 2015.

ESCOBAR, D. P.; DAFÉ, S. S. F.; SANTOS, D. B. Martensite reversion and texture formation in 17Mn-0.06C TRIP/TWIP steel after hot cold rolling and annealing. **Journal of Materials Research and Technology**, v. 4, p. 162-170, 2015.

FIELD, D. M.; BAKER, D. S.; VAN AKEN, D. C. On the prediction of a-martensite temperatures in medium manganese steels. **Metallurgical and Materials Transactions A**, v.48A, p.2150-2163, 2017.

FROMMEYER, G.; BRÜX, U. Microstructures and mechanical properties of high-strength Fe-Mn-Al-C light-weight TRIPLEX steels. **Steel Research International**, v.77, p.627-633, 2006.

FUSTER, V.; DRUKER, A. V.; BARUJ, A.; MALARRÍA, J.; BOLMARO, R. Characterization of phases in an Fe–Mn–Si–Cr–Ni shape memory alloy processed by different thermomechanical methods. **Materials Characterization**, v.109, p.128-137, 2015.

GALINDO-NAVA, E. I.; RIVERA-DÍAZ-DEL-CASTILLO, P. E. J. Understanding martensite and twin formation in austenitic steels: A model describing TRIP and TWIP effects. **Acta Materialia**, v.128, p.120-134, 2017.

GARCÍA DE ANDRÉS, C.; CABALLERO, F. G.; CAPDEVILA, C.; ÁLVAREZ, L. F. Application of dilatometric analysis to the study of solid-solid phase transformations in steels. **Materials Characterization**, v.48, p.101-111, 2002.

GARSHELIS, J.; FIEGEL, W. S. Magnetic observations of austenite-martensite transformations induced by torsional strain. **Journal of Applied Physics**, v.53, p.2407-2409, 1982.

GAUZZI, F.; MONTANARI, R.; PRINCIPI, G.; PERIN, A.; TATA, M. E. Martensite formation during heat treatment of AISI 304 steel with biphasic structure. **Materials Science and Engineering A**, v.273-275, p.443-447, 1999.

GAUZZI, F.; MONTANARI, R.; PRINCIPI, G.; TATA, M. E. AISI 304 steel: anomalous evolution of martensitic phase following heat treatments at 400°C. **Materials Science and Engineering A**, v.438-440, p.202-206, 2006.

GAZDER, A. A.; SALEH, A. A.; NANCARROW, M. J. B.; MITCHELL, D. R. G.; PERELOMA, E. V. A transmission Kikuchi diffraction study of a cold-rolled and annealed Fe–17Mn–2Si–3Al–1Ni–0.06C wt% steel. **Steel Research International**, v.86, p.1204-1214, 2015.

GEISER, B. P.; LARSON, D. J.; OLTMAN, E.; GERSTL, S.; REINHARD, D.; KELLY, T. F.; PROSA, T. J. Wide-field-of-view atom probe reconstruction. **Microscopy and Microanalysis**, v.15, p.292-293, 2009.

GORBATOV, O. I.; KUZNETSOV, A. R.; GORNOSTYREV, YU. N.; RUBAN, A. V.; ERSHOV, N. V.; LUKSHINA, V. A.; CHERNENKOV, YU. P.; FEDOROV, V. I. Role of Magnetism in the Formation of a Short-Range Order in Iron–Silicon Alloys. **Journal of Experimental and Theoretical Physics**, v.112, p. 848-859, 2011.

GRÄSSEL, O.; KRÜGER, L.; FROMMEYER, G.; MEYER, L. W. High strength Fe-Mn-(Al,Si) TRIP/TWIP steels development–properties–application. **International Journal of Plasticity**, v.16, p.1391-1409, 2000.

GUPTA, R. K.; ANANTHARAMAN, T. R. An X-ray diffraction study of deformation in h.c.p. rare-earth metals. **Journal of Less-Common Metals**, v.25, p.353-360, 1971.

GUTIERREZ-URRUTIA, I.; ZAEFFERER, S.; RAABE, D. Electron channeling contrast imaging of twins and dislocations in twinning-induced plasticity steels under controlled diffraction conditions in a scanning electron microscope. **Scripta Materialia**, v.61, p.737-740, 2009.

GUTIERREZ-URRUTIA, I.; ZAEFFERER, S.; RAABE, D. The effect of grain size and grain orientation on deformation twinning in a Fe–22wt.% Mn–0.6 wt.% C TWIP steel. **Materials Science and Engineering A**, v.527, p.3552-3560, 2010.

GUTIERREZ-URRUTIA, I.; RAABE, D. Dislocation and twin substructure evolution during strain hardening of an Fe–22wt.% Mn–0.6 wt.% C TWIP steel observed by electron channeling contrast imaging. **Acta Materialia**, v.59, p.6449-6462, 2011.

GUTIERREZ-URRUTIA, I.; ZAEFFERER, S.; RAABE, D. Coupling of electron channeling with EBSD: toward the quantitative characterization of deformation structures in the SEM. **Journal of the Minerals, Metals and Materials Society**, v.65, p.1229-1236, 2013.

GUY, K. B.; BUTTLER, E. P.; WEST, D. R. F. Reversion of bcc α' marteniste in Fe-Cr-Ni austenitic stainless steel. **Metals Science**, **v.**17, p.167-176, 1983.

HAMADA, A. S. **Manufacturing, Mechanical Properties and Corrosion Behaviour of High-Mn TWIP Steels.** 2007. Doctoral Thesis. Department of Mechanical Engineering, Faculty of Technology, University of Oulu, Linnanmaa, Finland, 2007.

HARRIS. COMMISSION OF THE EUROPEAN COMMUNITIES. JOINT RESEARCH CENTRE. ISPRA ESTABLISHMENT et al. **Mechanical behaviour and nuclear applications of stainless steel at elevated temperatures**. Varese, Italy: Maney Pub, 1982.

HERRERA, C.; PONGE, D.; RAABE, D. Design of a novel Mn-based 1GPa duplex stainless TRIP steel with 60% ductility by a reduction of austenite stability. **Acta Materialia**, v.59, p.4653-4664, 2011.

HILLERT, M. In: AARONSON, H. I. ed. Lectures on the Theory of Phase Transformations, 2nd ed. Warrendale, PA: TMS-AIME, 1999. p. 1.

HÖLSCHER, M.; RAABE, D.; LÜCKE, K. Rolling and Recrystallization Textures of BCC Steels. **Steel Research International**, v.62, p.567-575, 1991.

HÖLSCHER, M.; RAABE, D.; LÜCKE, K. Relationship between rolling textures and shear textures in fcc and bcc metals. **Acta Metallurgica et Materialia**, v.42, p.879-886, 1994.

HUANG, W. M. An assessment of the Fe-Mn system. **Calphad (Computer Coupling of Phase Diagrams and Thermochemistry)**, v.13, p.243-252, 1989.

HUFFMAN, G. P.; FISHER, R. M. Mössbauer studies of ordered and cold-worked Fe-Al alloys containing 30 to 50 at.% aluminum. **Journal of Applied Physics**, v.38, p.735-742, 1967.

IDRISSI, H.; RYELANDT, L.; VERON, M.; SCHRYVERS, D.; JACQUES, P.J. Is there a relationship between the stacking fault character and the activated mode of plasticity of Fe–Mn-based austenitic steels? **Scripta Materialia**, v.60, p.941-944, 2009.

INDEN, G. The role of magnetism in the calculation of phase diagrams, **Physica**, v.103B, p.82-100, 1981.

INDEN, G. The effect of continuous transformations on phase diagrams. **Bulletin of Alloy Phase Diagrams**, v.2, p.412-422, 1982.

INDEN, G.; NEUMANN, P. Simulation of diffusion-controlled phase transformations in steels. **Steel Research**, v.67, p.401-407, 1996.

JIANG, B. H.; SUN, L.; LI, R.; HSU, T.Y. Influence of austenite grain size on $\gamma-\varepsilon$ martensitic transformation temperature in Fe-Mn-Si-Cr alloys. **Science of Metallurgical Materials**, v. 33, p.63-68, 1995.

JIANG, B. H.; QI, X.; ZHOU, W.; HSU, T.Y. Comment on “Influence of austenite grain size on $\gamma \rightarrow \varepsilon$ martensitic transformation temperature in Fe-Mn-Si-Cr alloys”. **Scripta Materialia**, v.34, p.771-773, 1996.

JUN, J. H.; CHOI, C. S. Variation of stacking fault energy with austenite grain size and its effect on the M_s temperature of $\gamma \rightarrow \varepsilon$ martensitic transformation in Fe-Mn alloy. **Materials Science and Engineering A**, v.258, p.535-556, 1998.

KAPOOR, R.; KUMAR, L.; BATRA, I. S. A dilatometric study of the continuous heating transformation in 18wt.%Ni maraging steel of grade 350. **Materials Science and Engineering A**, v.352, p.318-324, 2003.

KAPOOR, R.; BATRA, I. S. On the α’ to γ transformation in maraging (grade 350), PH 13-8 Mo and 17-4 PH steels. **Materials Science and Engineering A**, v.371, p.324-334, 2004.

KEIJSER, T. H.; MITTEMEIJER, E. J.; ROZENDAAL, H. C. F. The determination of crystallite-size and lattice-strain parameters in conjuction with profile-refinement method for the determination of crystal structures. **Journal of Applied Crystallography**, v. 16, p. 309-316, 1983.

KELLY, P. M. The martensite transformation in steels with low stacking fault energy. **Acta Metallurgica**, v.13, p.635-646, 1965.

KIM, H.; SUH, D.-W.; KIM, N. J. Fe-Al-Mn-C lightweight structural alloy: a review on the microstructures and mechanical properties. **Science and Technology of Advanced Materials**, v.14, p.014205(1)-014216(11), 2013.

KIM, J. J.; DE COOMAN, B. C. Observation of dislocations with Burgers vector containing a <c> component in martensitic ε Fe-17%Mn. **Scripta Materialia**, v.128, p.78-82, 2017.

KISKO, A.; MISRA, R. D. K.; TALONEN, J.; KARJALAINEN, L. P. The influence of grain size on the strain-induced martensitic formation in tensile straining of an austenitic 15Cr-9Mn-Ni-Cu stainless steel. **Materials Science and Engineering A**, v.578, p.408-416, 2013.

KOYAMA, M.; ZHANG, Z.; WANG, M.; PONGE, D.; RAABE, D.; TSUZAKI, K.; NOGUCHI, H.; TASAN, C. C. Bone-like crack resistance in hierarchical metastable nanolaminate steels. **Science**, v.355, p.1055-1057, 2017.

KUMAR, B. R.; SINGH, A. K.; DAS, S.; BHATTACHARYA, D. K. Cold rolling texture in AISI 304 stainless steel. **Materials Science and Engineering A**, v.364, p.132-139, 2004.

KUNDU, S.; BHADESHIA, H. K. D. H. Crystallographic texture and intervening transformations. **Scripta Materialia**, v.57, p.869-872, 2007.

KUZMINA, M.; HERBIG, M.; PONGE, D.; SANDLÖBES, S.; RAABE, D. Linear complexions: Confined chemical and structural states at dislocations. **Science**, v.349, p.1080-1083, 2015.

KUZMINA, M.; PONGE, D.; RAABE, D. Grain boundary segregation engineering and austenite reversion turn embrittlement into toughness: Example of a 9 wt.% medium steel. **Acta Materialia**, v.86, p.182-192, 2015.

KWIATKOWSKI DA SILVA, A.; LEYSIN, G.; KUZMINA, M.; PONGE, D.; HERBIG, M.; SANDLÖBES, S.; GAULT, B.; NEUGEBAUER, J.; RAABE, D. Confined chemical and structural states at dislocations in Fe-9wt%Mn steels: a correlative TEM-atom probe study combined with multiscale modelling. **Acta Materialia**, v.124, p.305-315, 2017.

KWIATKOWSKI DA SILVA, A.; INDEN, G.; KUMAR, A.; PONGE, D.; GAULT, B.; RAABE, D. Competition between formation of carbides and reversed austenite during tempering of a medium-manganese steel studied by thermodynamic-kinetic simulations and atom probe tomography. **Acta Materialia**, v.147, p.165-175, 2018a.

KWIATKOWSKI DA SILVA, A.; PONGE, D.; PENG, Z.; INDEN, G.; LU, Y.; BREEN, A.; GAULT, B.; RAABE, D. Phase nucleation through confined spinodal fluctuations at crystal defects evidenced in Fe-Mn alloys. **Nature Communications**, v.9, p.1-11, 2018b. DOI: 10.1038/s41467-018-03591-4

LACAZE, J.; SUNDMAN, B. An Assessment of the Fe-C-Si System. **Metallurgical Transactions A**, v.22A, p.2211-2223, 1991.

LEE, Y. K.; CHOI, C. S. Driving force for $\gamma \rightarrow \varepsilon$ martensitic transformation and stacking fault energy of γ in Fe-Mn binary system. **Metallurgical and Materials Transactions A**, v.31, p.355-360, 2000.

LEE, Y. Relationship between austenite dislocation density introduced during thermal cycling and M_s temperature in an Fe-17 wt pct Mn alloy. **Metallurgical and Materials Transactions A**, v.33, p.1913-1917, 2002.

LI, X.; CHEN, L.; ZHAO, Y.; MISRA, R. D. K. Influence of manganese content on ε-/α'-martensitic transformation and tensile properties of low-C high-Mn TRIP steels. **Materials and Design**, v.142, p.190-202, 2018.

LIU, Y. C.; SOMMER, F.; MITTEMEIJER, E. J. Abnormal austenite-ferrite transformation behaviour in substitutional Fe-based alloys. **Acta Materialia**, v.51, p.507-519, 2003.

LU, F.; YANG, P.; MENG, L.; CUI, F.; DING, H. Influences of thermal martensites and grain orientations on strain-induced martensites in high manganese TRIP/TWIP steels. **Journal of Materials Science and Technology**, v.27, p.257-265, 2011.

LÜ, Y.; HUTCHINSON, B.; MOLODOV, D. A.; GOTTSTEIN, G. Effect of deformation and annealing on the formation and reversion of ε-martensite in an Fe–Mn–C alloy. **Acta Materialia**, v.58, p.3079-3090, 2010.

LUTTEROTTI, L.; SCARDI, P.; MAITRELLI, P. Simultaneous structure and size-strain refinement by the Rietveld method. **Journal of Applied Crystallography**, v.23, p.246-52, 1990.

LUTTEROTTI, L.: MAUD, version 2.038, 2006
Disponível em: http://www.ing.unitn.it/~luttero/maud. Acesso em: 16 jun. 2019.

MA, B.; LI, C.; HAN, Y.; WANG, J. $\gamma \rightarrow \alpha'$ Martensitic transformation and magnetic property of cold rolled Fe–20Mn–4Al–0.3C steel. **Journal of Magnetism and Magnetic Materials**, v.419, p.249-254, 2016.

MANGONON, P. L.; THOMAS, G. The martensite phases in 304 stainless steel. **Metallurgical transactions**, v.1, p.1577-1586, 1970.

MÉSZÁROS, I.; PROHÁSZKA, J. Magnetic investigation of the effect of α′-martensite on the properties of austenitic stainless steel**. Journal of Materials Processing and Technology**, v.161, p.162-168, 2005.

MILLER, M. K.; SMITH, D. W. An atom probe study of the anomalous field evaporation of alloys containing silicon. **Journal of Vacuum Science and Technology**, v.19, p.57-62, 1981.

MITRA, A.; SRIVASTAVA, P. K.; DE, P. K.; BHATTACHARYA, D. K.; JILES, D. C. Ferromagnetic properties of deformation-induced martensite transformation in AISI 304 stainless steel. **Metallurgical and Materials Transactions A**, v.35A, p.599-605, 2004.

MONTANARI, R. Increase of martensite content in cold rolled AISI 304 steel produced by annealing at 400°C. **Materials Letters**, v.10, p.57-61, 1990.

MOSZNER, F.; POVODEN-KARADENIZ, E.; POGATSCHER, S.; UGGOWITZER, P. J.; ESTRIN, Y.; GERSTL, S. S. A.; KOZESCHNIK, E.; LÖFFLER, J. F. Reverse $\alpha' \rightarrow \gamma$ transformation mechanisms of martensitic Fe-Mn and age-hardenable Fe-Mn-Pd alloy upon fast and slow continuous heating. **Acta Materialia**, v.72, p.99-109, 2014.

MUMTAZ, K.; TAKAHASHI, S.; ECHIGOYA, J.; KAMADA, Y.; ZHANG, L.F.; KIKUCHI, H.; ARA, K.; SATO, M. Magnetic measurements of martensitic transformation in austenitic stainless steel after room temperature rolling. **Journal of Materials Science**, v.39, p.85-97, 2004a.

MUMTAZ, K.; TAKAHASHI, S.; ECHIGOYA, J.; KAMADA, Y.; ZHANG, L. F.; KIKUCHI, H.; ARA, K.; SATO, M. Magnetic measurements of the reverse martensite to austenite transformation in a rolled austenitic stainless steel. **Journal of Materials Science**, v.396, p.1997-2010, 2004b.

NAKADA, N.; ARAKAWA, Y.; PARK, K. S.; TSUCHIYAMA, T.; TAKAKI, S. Dual phase structure formed by partial reversion of cold-deformed martensite. **Materials Science and Engineering A**, v.553, p.128-133, 2012.

NAKADA, N.; TSUCHIYAMA, T.; TAKAKI, S.; PONGE, D.; RAABE, D. Transition from diffusive to displacive austenite reversion in low-alloy steel. **ISIJ International**, v.53, p.2275-2277, 2013.

NAKADA, N.; MIZUTANI, K.; TSUCHIYAMA, T.; TAKAKI, S. Difference in transformation behavior between ferrite and austenite formations in medium manganese steel. **Acta Materialia**, v.65, p.251-258, 2014.

OLSON, G. B.; COHEN, M. A general mechanism of martensitic nucleation: part I. General concepts and the FCC $\rightarrow$ HCP transformation. **Metallurgical Transactions A**, v.7 p.1897-1904, 1976.

PADILHA, A. F.; PLAUT, R. L.; RIOS, P. R. Annealing of cold-worked austenitic stainless steels. **ISIJ International**, v.43, p.135-143, 2003.

PIERCE, D. T.; NOWAG, K.; MONTAGNE, A.; JIMÉNEZ, J. A.; WITTIG, J. E.; GHISLENI, R. Single crystal elastic constants of high-manganese transformation- and twinning-induced plasticity steels determined by a new method utilizing nanoindentation, **Materials Science and Engineering A**, v.578, p.134-139, 2013.

PIERCE, D. T.; JIMÉNEZ, J. A.; BENTLEY, J.; RAABE, D.; OSKAY, C.; WITTIG, J. E. The influence of manganese content on the stacking fault and austenite/ε-martensite interfacial energies in Fe–Mn–(Al–Si) steels investigated by experiment and theory. **Acta Materialia**, v.68, p.238-253, 2014.

PISARIK, S.T.; VAN AKEN, D.C. Crystallographic orientation of the ε → α martensitic (athermal) transformation in a FeMnAlSi steel. **Metallurgical and Materials Transactions A**, v. 45A, p. 3173-3178, 2014.

PISARIK, S. T.; VAN AKEN, D. C. Thermodynamic driving force of the γ → ε transformation and resulting Ms temperature in high-Mn steels. **Metallurgical Materials Transactions A**, v.47, p.1009-1018, 2016.

POPA, N. C. The (hkl) dependence of diffraction-line broadening caused by strain and size for all Laue groups in Rietveld refinement. **Journal of Applied Crystallography**, v.31, p.176-80, 1998.

PORTER, D. A.; EASTERLING, K. E.; SHERIF, M. Y. **Phase transformations in metals and alloys.** Boca Raton, FL: CRC Press, 2009.

PRAMANIK, S.; SALEH, A. A.; PERELOM, E. V.; GAZDER, A. A. Effect of isochronal annealing on the microstructure, texture and mechanical properties of a cold-rolled high manganese steel. **Materials Characterization**, v.144, p.66-76, 2018a.

PRAMANIK, S.; GAZDER, A. A.; SALEH, A. A.; PERELOMA, E. V. Nucleation, coarsening and deformation accommodation mechanisms of ε-martensite in a high manganese steel. **Materials Science and Engineering A**, v.731, p.506-519, 2018b.

PRINCE, E. **The Rietveld Method**. Oxford: Ed. R. A. Young, Oxford University Press, Oxford, UK, 1993.

RAABE, D.; LÜCKE, K. Textures of ferritic stainless steels. **Materials Science and Technology**, v.9, p.302-312, 1993.

RAABE, D. Texture and microstructure evolution during cold rolling of a strip cast and of a hot rolled austenitic stainless steel. **Acta Materialia**, v.45, p.1137-1151, 1997.

RAABE, D.; SANDLÖBES, S.; MILLÁN, J.; PONGE, D.; ASSADI, H.; HERBIG, M.; CHOI, P.-P. Segregation engineering enables nanoscale martensite to austenite phase transformation at grain boundaries: a pathway to ductile martensite. **Acta Materialia**, v.61, p.6132-6152, 2013.

RAABE, D.; SPRINGER, H.; GUTIERREZ-URRUTIA, I.; ROTERS, F.; BAUSCH, M.; SEOL, J. B.; KOYAMA, M.; CHOI, P. P.; TSUZAKI, K. Alloy design, combinatorial synthesis, and microstructure-property relations for low-density Fe-Mn-Al-C austenitic steels. **Journal of the Minerals, Metals and Materials Society**, v.66, p.1845-1856, 2014.

REMY, L.; PINEAU, A. Twinning and strain-induced F.C.C. → H.C.P. transformation in the Fe-Mn-Cr-C system. **Materials Science and Engineering A**, v.28, p.99-107, 1977.

SAEED-AKBARI, A.; IMLAU, J.; PRAHL, U.; BLECK, W. Derivation and variation in composition-dependent stacking fault energy maps based on subregular solution model in high-manganese steels. **Metallurgical and Materials Transactions A**, v.40, p.3076-3090, 2009.

SAHU, P.; DE, M.; KAJIWARA, S. Microstrucutral characterization of stress-induced martenistes evolved at low temperatures in deformed powders of Fe-Mn-C alloys by the Rietveld method. **Journal of Alloys Compounds**, v.346, p.158-169, 2002.

SAHU, P.; HAMADA, A. S.; GHOSH, R. N.; KARJALAINEN, L. P. X-ray diffraction study on cooling-rate-induced γ fcc → ε hcp martensitic transformation in cast-homogenized Fe-26Mn-0.14C austenitic steel. **Metallurgical and Materials Transactions A**, v. 38, p. 1991-2000, 2007.

SAHU, P.; HAMADA, A. S.; SAHU, T.; PUUSTINEN, J.; OITTINEN, T.; KRJALAINEN, L. P. Martensitic transformation during cold rolling deformation of an austenitic Fe-26Mn-0.14C alloy. **Metallurgical Materials Transactions A**, v.43A, p.47-55, 2012.

SATO, A.; SOMA, K.; MORI, T. Hardening due to pre-existing ε-Martensite in an Fe-30Mn-1Si alloy single crystal. **Acta Metallurgica**, v.30, p.1901-1907, 1982.

SCHNEIDER, A.; INDEN, G. Simulation of the kinetics of precipitation reactions in ferritic steels. **Acta Materialia**, v.53, p.519-531, 2005.

SEOL, J. B.; RAABE, D.; CHOI, P. P.; IM, Y. R.; PARK, C. G. Atomic scale effects of alloying, partitioning, solute drag and austempering on the mechanical properties of high-carbon bainitic–austenitic TRIP steels. **Acta Materialia**, v.60, p.6183-6199, 2012.

SHINTANI, T.; MURATA, Y. Evaluation of the dislocation density and dislocation character in cold rolled type 304 steel determined by profile analysis of X-ray diffraction. **Acta Materialia**, v.59, p.4314-4322, 2011.

SMOLUCHOWSKI, R. Influence of order on magnetic properties. **Le Journal de Physique et le Radium**, v.12, p.389-398, 1951.

SOUZA FILHO, I. R.; SANDIM, M. J. R.; COHEN, R.; NAGAMINE, L. C. C. M.; HOFFMANN, J.; BOLMARO, R. E.; SANDIM, H. R. Z. Effects of strain-induced martensite and its reversion on the magnetic properties of AISI 201 austenitic stainless steel. **Journal of Magnetization and Magnetic Materials**, v.419, p.156-165, 2016.

SOUZA FILHO, I. R.; ZILNYK, K. D.; SANDIM, M. J. R.; BOLMARO, R. E.; SANDIM, H. R. Z. Strain partitioning and texture evolution during cold rolling of AISI 201 austenitic stainless steel. **Materials Science and Engineering A**, v.702, p.161-172, 2017.

SOUZA FILHO, I. R.; SANDIM, M. J. R.; COHEN, R.; NAGAMINE, L. C. C. M.; SANDIM, H. R. Z.; RAABE, D. Magnetic properties of a 17.6 Mn-TRIP steel: Study of strain-induced martensite formation, austenite reversion, and athermal α′-formation. **Journal of Magnetism and Magnetic Materials**, v.473, p.109-118, 2019a.

SOUZA FILHO, I. R.; SANDIM, M. J. R.; PONGE, D.; SANDIM, H. R. Z.; RAABE, D. Strain hardening mechanisms during cold rolling of a high-Mn steel: Interplay between submicron defects and microtexture. **Materials Science and Engineering A**, v.754, p.636-649, 2019b.

SOUZA FILHO, I. R.; KWIATKOWSKI DA SILVA, A.; SANDIM, M. J. R.; PONGE, D.; GAULT, B.; SANDIM, H. R. Z.; RAABE, D. Martensite to austenite reversion in a high-Mn steel: Partitioning dependent two-stage kinetics revealed by atom probe tomography, *in-situ* magnetic measurements and simulation. **Acta Materialia**, v.166, p.178-191, 2019c.

STEINMETZ, D. R.; JÄPEL, T.; WIETBROCK, B.; EISENLOHR, P.; GUTIERREZ-URRUTIA, I.; SAEED–AKBARI, A.; HICKEL, T.; ROTERS, F.; RAABE D. Revealing the strain-hardening behavior of twinning-induced plasticity steels: Theory, simulations, experiments. **Acta Materialia**, v.61, p.494-510, 2013.

TAKAKI, S.; NAKATSU, H.; TOKUNAGA, Y. Effects of austenite grain size on ε martensitic transformation in Fe-15mass%Mn alloy. **Materials Transactions**, v.34, p.489-495, 1993.

TAKAKI, S.; TOMIMURA, K.; UEDA, S. Effect of pre-cold-working on diffusional reversion of deformation induced martensite in metastable austenitic stainless steel. **ISIJ International**, v.34, p.522-527, 1994.

TASAN, C. C.; DIEHL, M.; YAN, D.; ZAMBALDI, C.; SHANTHRAJ, P.; ROTERS, F.; RAABE, D. Integrated experimental–simulation analysis of stress and strain partitioning in multiphase alloys. **Acta Materialia**, v.81, p.386-400, 2014a.

TASAN, C. C.; HOEFNAGELS, J. P. M.; DIEHL, M.; YAN, D.; ROTERS, F.; RAABE, D. Strain localization and damage in dual phase steels investigated by coupled in-situ deformation experiments and crystal plasticity simulations. **International Journal of Plasticity**, v.63, p.198-210, 2014b.

TAVARES, S. S. M.; DA SILVA, M. R.; NETO, J. M.; MIRAGLIA, S.; FRUCHART, D. Ferromagnetic properties of cold-rolled AISI 304L steel. **Journal of Magnetism and Magnetic Materials**, v.242-245, part 2, p.1391-1394, 2002.

THOMPSON, K.; LAWRENCE, D.; LARSON, D. J.; OLSON, J. D.; KELLY, T. F.; GORMAN, B. In situ site-specific specimen preparation for atom probe tomography. **Ultramicroscopy**, v.107, p.131-139, 2007.

TOMIMURA, K.; TAKAKI, S.; TOKUNAGA, Y. Reversion mechanism from deformation induced martensite to austenite in metastable austenitic stainless steel. **ISIJ International**, v.31, p.1431-1437, 1991.

ÚNGAR, T.; DRAGOMIR, I.; RÉVÉSZ, Á.; BORBÉLY, A. The contrast factors of dislocations in cubic crystals: the dislocation model of strain anisotropy in particle. **Journal of Applied Crystallography**, v.32, p.992-1002, 1999.

ÚNGAR, T. Microstructural parameters from X-ray diffraction peak broadening. **Scripta Materialia**, v.51, p.777-781, 2004.

VAN HOUTE, P. Simulation of the rolling and shear texture of brass by the Taylor theory adapted for mechanical twinning. **Acta Metallurgica**, v.26, p.591-604, 1978.

WANG, M. M.; TASAN, C. C.; PONGE, D.; KOSTKA, A.; RAABE, D. Smaller is less stable: Size effects on twinning vs. transformation of reverted austenite in TRIP-maraging steels. **Acta Materialia**, v.79, p.268-281, 2014.

WANG, M. M.; TASAN, C. C.; PONGE, D.; DIPPEL, A. C.; RAABE, D. Nanolaminate transformation-induced plasticity–twinning-induced plasticity steel with dynamic strain partitioning and enhanced damage resistance. **Acta Materialia**, v.85, p.216-228, 2015.

WARREN, B. E. **X-Ray Diffraction**. Reading, UK: Addison-Wesley, 1969.

WILLIAMSON, G. K.; SMALLMAN III, R. E. Dislocation densities in some annealed and cold-worked metals from measurements on the X-ray Debye-Scherrer spectrum. **Philosophical Magazine**, v.1, p.34-46, 1956.

WONG, S. L.; MADIVALA, M.; PRAHL, U.; ROTERS, F.; RAABE, D. A crystal plasticity model for twinning- and transformation-induced plasticity. **Acta Materialia**, v.118, p.40-151, 2016.

WRIGHT, S. I.; NOWELL, M. M.; FIELD, D. P. A review of strain analysis using electron backscatter diffraction. **Microscopy and Microanalysis**, v.17, p.316-329, 2011.

WU, X. L.; YANG, M. X.; YUAN, F. P.; CHEN, L.; ZHU, Y. T. Combining gradient structure and TRIP effect to produce austenite stainless steel with high strength and ductility. **Acta Materialia**, v.112, p.337-346, 2016.

WUANG, Y. N.; HUANG, J. C. Texture analysis in hexagonal materials. **Materials Chemistry and Physics**, v.81, p.11-26, 2003.

XINGJUN, L.; SHIMING, H. A thermodynamic calculation of the Fe-Mn-Al ternary system. **Calphad (Computer Coupling of Phase Diagrams and Thermochemistry)**, v.17, p.79-91, 1993.

YANG, W. S.; WAN, C. M. The influence of aluminium content to the stacking fault energy in Fe-Mn-Al-C alloy system. **Journal of Materials Science**, v.25, p.1821-1823, 1990.

YANUSHKEVICH, Z.; BELYAKOV, A.; HAASE, C.; MOLODOV, D. A.; KAIBYSHEV, R. Sctructural/textural changes and strengthening of an advanced high-Mn steel subjected to cold rolling. **Materials Science and Engineering A**, v.651, p.763-773, 2018.

ZAEFFERER, S.; ELHAMI, N. Theory and application of electron channelling contrast imaging under controlled diffraction conditions. **Acta Materialia**, v.75, p.20-50, 2014.

ZENG, Q.; BAKER, I. Magnetic properties and thermal ordering of mechanically alloyed Fe–40 at% Al. **Intermetallics**, v.14 p.396-405, 2006.

ZHANG, J.; RAABE, D.; TASAN, C. C. Designing duplex, ultrafine-grained Fe-Mn-Al-C steels by tuning phase transformation and recrystallization kinetics. **Acta Materialia**, v.141 p.374-387, 2017.

ZORZI, J. C. S. **Avaliação do processamento de aço TRIP-TWIP em escala piloto**. 2014. Dissertação (Mestrado). Universidade Federal de Minas Gerais, Belo Horizonte, Brasil, 2014.